STUDY OF AN INSTRUMENT FOR SENSING ERRORS
IN A TELESCOPE WAVEFRONT

L. J. Golden
R. V. Shack
P. N. Slater

CASE FILE
COPY

ACKNOWLEDGMENTS

ABSTRACT

This report describes the first year's work on NASA Contract NAS8-27863 entitled "Study of an Instrument for Sensing Errors in a Telescope Wavefront." It contains the partial results of theoretical and experimental investigations of different focal plane sensor configurations for determining the error in a telescope wavefront.

TABLE OF CONTENTS

LIST OF FIGURES

LIST OF TABLES

CHAPTER I

INTRODUCTION

The purpose of our work at the Optical Sciences Center is to conduct experimental and analytical research on optical testing concepts suitable for application as figure sensors for the Large Space Telescope (LST) program.

An optical testing device for this application, which we will refer to for brevity as a figure sensor, should have a wide dynamic range from a few waves, so that it may serve as an absolute standard for alignment-associated problems, to about a hundredth of a wave, so that it may serve as a means of sensing for nulling out figure errors or for measuring wavefront errors for post-detection image processing. For these purposes either selected wavefront samples or the entire system wavefront should be accessible for measurement. In order to accomplish these goals the figure sensor has to be placed at the focal plane of the telescope, and a real star source has to be used.

As there is no single test that has the range required for alignment-associated wavefront errors and also the sensitivity required $(1/100\lambda)$ for image processing and figure correction, we have divided our work into a study of: (1) a coarse range geometrical sensor operating from several waves to a large fraction of a wave, and (2) a fine range

1

sensor useful from a large fraction of a wave to approximately $1/100\lambda$. We have narrowed our study to one candidate in the coarse range (a modified Hartmann test) and to three contenders in the fine range region (Zernike, shearing polarization test, and Zernike polarization test). These are discussed in detail in this report. We expect that many of the components used in the fine range sensor will also be suitable for use with the coarse range sensor and that the range of operation for coarse and fine sensing will have significant overlap.

CHAPTER II

ABERRATED TELESCOPE WAVEFRONT SIMULATOR

1. General.

In order to experimentally determine the performance capabilities
of the various types of figure sensors, we have designed and fabricated a
device to produce a simulated aberrated telescope wavefront. This simu-
lator includes a variable magnitude star, imaged by a specially designed
telescope which can introduce various alignment, focus and figure errors
such as may occur in the operational LST. The aberrated star image pro-
duced can then be evaluated by the figure sensor under study. A sketch
of the simulator appears in Fig. 1. The star source consists of a
quartz iodine tungsten filament lamp, which is run by a stabi-
lized power supply. The filament is focused onto a 25 µm pinhole,
through a narrow band interference filter if required. The star source
can be moved in the x,y direction to simulate wavefront tilt in any
direction. This light is collimated by a 1.2m (48") focal length tele-
scope objective to simulate a star at infinity. The next 5 elements (bi-
convex lens, biconcave lens, two flat plates and thick meniscus) are
collectively called the aberration generator. This group of elements
produces an f/6 beam into which various orientations and magni-
tudes of coma, astigmatism, and spherical aberration may be introduced in

3
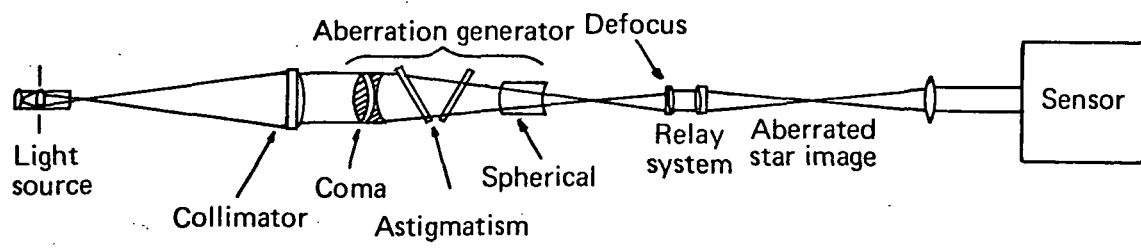
Fig. 1. Aberrated telescope wavefront simulator.

an exact manner. A relay system then reimages the f/6 image. The first element of the relay system is a 40 mm cemented doublet which collimates the aberrated star image. This element can be moved along the optical axis of the system in order to correct for focus shift produced by the aberration generator, or in order to introduce known amounts of defocus into the wavefront. The second element of the relay system is an 80 mm focal length telescope objective, which converges the light to an f/12 cone, completing the simulation of an f/12 telescope where tilt, defocus, astigmatism, coma, and spherical aberration can be introduced into the beam in differential amounts of about $1/100\lambda$ and over the range of ± 2 waves. The final collimating lens is related to the figure sensor under test and will be discussed in detail later.

2. Aberration Generator.

At the heart of the aberrated telescope wavefront simulator is the aberration generator. This instrument has been designed to introduce precisely known amounts and orientations of different primary aberration types. What follows is a discussion of the design concept, the fabricated optics, the optical evaluation and the mechanical assembly of the aberration generator.

The optical design is shown diagrammatically in Fig. 2. The instrument consists of an achromatic air-spaced doublet with a 25.4 mm clear aperture and a 152.4 mm focal length. The air-spaced doublet is designed for high coma but minimum spherical and chromatic aberration.

S5 R6 T5 R5 S4 Plano Plano T4 S3 T3 Plano Plano S2 R4 R3 R2 R1 T2 T1 S1

Rear nodal point
−12.90 mm from
rear vertex
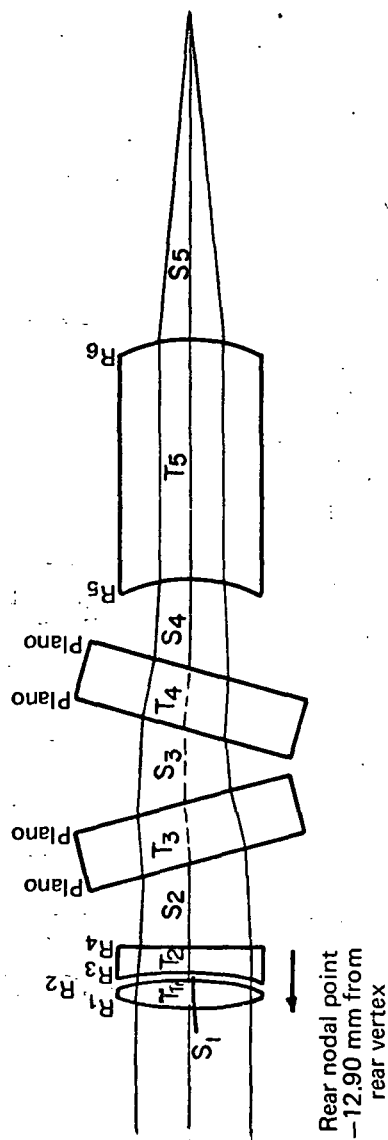
$R_1 = R_2 = 65.94$ mm
$R_3 = 59.36$ mm
$R_4 = 269.72$ mm
$R_5 = R_6 = 44.72$ mm
$T_1 = 6.36$ mm
$T_2 = 5.08$ mm
$T_3 = T_4 = 12.70$ mm
$T_5 = 51.08$ mm
$S_1 = 1.27$ mm
$S_2 + S_3 + S_4 = 51.46$ mm when tilts = 0°
$S_5 = 70.87$ mm

Element 1: diameter = 30.18 mm
Element 2: diameter = 30.18 mm
Element 3: diameter = 47.62 mm
Element 4: diameter = 47.62 mm
Element 5: diameter = 30.18 mm
Glass: element 2 = Schott F4
       all others = Schott SK4

Coatings: all MgF_2, n = 1.62
Maximum tilt of plates ≈ 15° (astigmatism)
Maximum tilt of front doublet = 1.5° (coma)
12-mm leftward movement of meniscus = 2.8 waves of −OPD
20-mm rightward movement of meniscus = 1.2 waves of +OPD
Maximum image excursion ≈ 3 mm

Fig. 2. Aberration generator, achromatic, nominal 5900 Å, nominal 152-mm EFL, f/6.

The residual astigmatism, inherent in a doublet design, is unavoidable but can be readily taken into account. This doublet is tilted about its rear nodal point (located 12.90 mm inside the last radius R_4) to generate approximately 2 waves of third-order coma at a tilt of 1.5°. About 0.4 waves of sagittal astigmatism are generated unavoidably at this angle. However, since the coma varies linearly with tilt, while the astigmatism varies quadratically, the astigmatism will be negligible for small amounts of coma (i.e., for up to about quarter-wave of coma, the residual astigmatism is less than $1/100\lambda$). Higher order aberration terms are negligible for the objective. Although the doublet is color corrected, for precise work a 40 to 50 nm bandwidth filter should be used. Following the doublet are a set of parallel plates which can be counter tipped to introduce astigmatism. No third-order coma is introduced, and higher order aberrations are negligible. These plates can be tilted up to 15° at which point 2.2 waves of sagittal astigmatism are introduced. Again, this astigmatism contribution varies quadratically. The last element, a thick meniscus lens, can be moved longitudinally for generation of +2.8 to -1.2 waves of spherical aberration. However, the effect of moving this meniscus is complicated since both fifth- and third-order spherical aberration are changed. A change in focal position and effective focal length must also be taken into account.

3. Design Evaluation.

a. Coma.

The air-spaced doublet has been ray traced at a field angle of 1.5° and the important coefficients for two wavelengths appear below in Table I.

TABLE I

DESIGN COEFFICIENTS FOR DOUBLET

λ = 546.1 nm, Field Angle 1.5°

SA3	SA5	SA7	CMA3	CMA5	AST3
-1.84587E-3	+1.70755E-3	+1.86313E-4	-2.23989E-3	-1.7334E-5	-8.95394E-4

λ = 632.8 nm

-2.57982E-3	1.66305E-3	1.87093E-4	-2.22001E-3	-2.45111E-5	-8.92584E-4

The meniscus element is positioned to minimize any spherical aberration residual, since extrinsic higher order aberration contributions are small and higher order coma and astigmatism are negligible, we can compute the Optical Path Difference (OPD) changes introduced by the doublet by using

$$OPD_{Doublet} = -\frac{1}{2} CMA3 r^3 \cos\phi U - \frac{1}{4} AST3(\cos 2\phi+1)r^2 U^2,$$

where r is the fractional pupil height, ϕ is the angle measured from a direction perpendicular to the tilt axis, and U is the fractional tilt angle. Below is the OPD calculated for these tilt effects at two wavelengths. As mentioned before, for OPD $\leq \frac{1}{4}$ wave, the astigmatism contribution is $< 1/100\lambda$ and can be ignored.

b. Astigmatism.

The two plane-parallel plates were ray traced at an angle of 15° in an f/6 convergent beam. Because of the high degree of correction in the objective, it is expected that extrinsic contributions due to objective imperfection will be negligible. Since two counter-tipped plates are used the third-order coma cancels and the third-order astigmatism dominates, with higher order aberrations inconsequential. The meniscus element is positioned to minimize the residual spherical. A summary of the third- and fifth-order coefficients for the two counter-tipped plates appears in Table II. The OPD due to astigmatism is calculated from

$$OPD_{Astigmatism} = -\frac{1}{4} AST3(\cos 2\phi + 1)r^2 U^2.$$

c. Spherical aberration.

The position of the meniscus element relative to the doublet will determine the amount of spherical aberration in the system. This aberration contribution is strictly speaking very complex consisting of third, fifth, seventh and higher order spherical coefficients to determine the OPD in the pupil. However, from comparisons of exact ray trace OPD to

TABLE II

DESIGN COEFFICIENTS FOR ASTIGMATISM

λ = 546.1 nm, Plate Tilt 15°

SA3	SA5	AST3	AST5
4.68100E-4	-1.50419E-6	4.83740E-3	-1.60639E-6

λ = 632.8 nm

4.67761E-4	-1.49766E-6	4.833908E-3	-1.599410E-6

---

that of OPD calculated by using third-, fifth- and seventh-order coefficients, the computational error is always better than 5% or 7% in the OPD, where the smaller percentage refers to meniscus position changes made to introduce small errors ($\sim 1/10\lambda$) and the larger percentage refers to meniscus position changes made to introduce larger errors ($\sim 1/2\lambda$). The OPD is calculated from

$$OPD = -\frac{1}{8} SA3r^4 - \frac{1}{12} SA5r^6 - \frac{1}{16} SA7r^8.$$

As we reposition the meniscus we also change the back focal position (BFP) and the aberration generator effective focal length (GEFL). This change in BFP is compensated for in the relay optics and the change in GEFL results in an f# change which can be compensated for by stopping down the pupil in order to maintain an f/6 cone in the generator and an

f/12 cone in the simulator. Figure 3 illustrates the BFP as a function
on meniscus position. Figure 4 shows the GEFL as a function of meniscus
position. Figures 5-18 show the variation of third-, fifth- and seventh-
order spherical aberration with meniscus position for two wavelengths.

    d. <u>Overall optical path difference.</u>

    The graphical coefficients were obtained by ray tracing at vari-
ous positions of the meniscus. In order to obtain analytical expressions
for BFP, GEFL, SA3, SA5, and SA7 each of the curves was fitted to a
polynomial expression which resulted in the following equations:

$$SA3 = (2.4683572 \times 10^{-7})x^3 - (5.4403322 \times 10^{-5})x^2$$

$$+ (3.9624001 \times 10^{-3})x - 0.092684628$$

$$SA5 = (5.4406814 \times 10^{-8})x^3 - (1.0583634 \times 10^{-5})x^2$$

$$+ (7.0274608 \times 10^{-4})x - 0.014209098$$

$$SA7 = (7.9180215 \times 10^{-9})x^3 - (1.4642964 \times 10^{-6})x^2$$

$$+ (9.3790299 \times 10^{-5})x - (1.9275608 \times 10^{-3})$$

$$BFP = -(3.9558132 \times 10^{-5})x^3 - (8.0375794 \times 10^{-4})x^2$$

$$+ (0.30452283)x + 108.12638$$

$$GEFL = (3.8922327 \times 10^{-5})x^3 + (3.9824714 \times 10^{-4})x^2$$

$$+ (0.65624124)x + 118.61591$$

where x is a term in millimeters, which referes to the spacing between
the plane-parallel plates and the meniscus element. It is found by
adding the reading on the dial indicator to a constant C. This constant
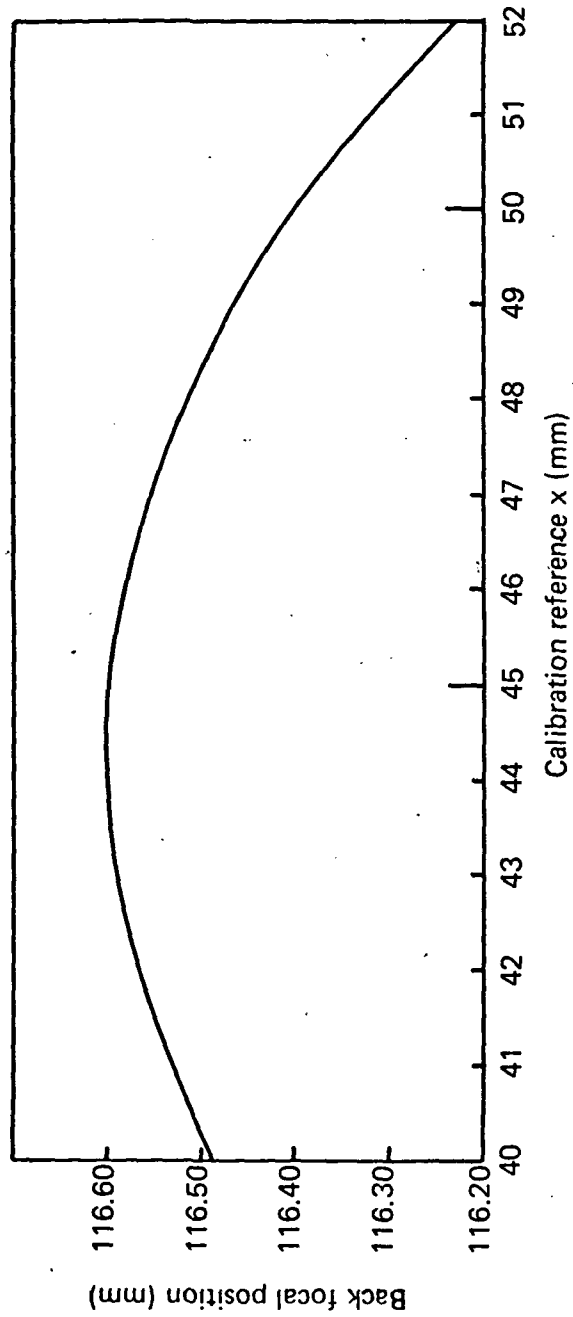
Fig. 3. Back focal position as a function of meniscus position.
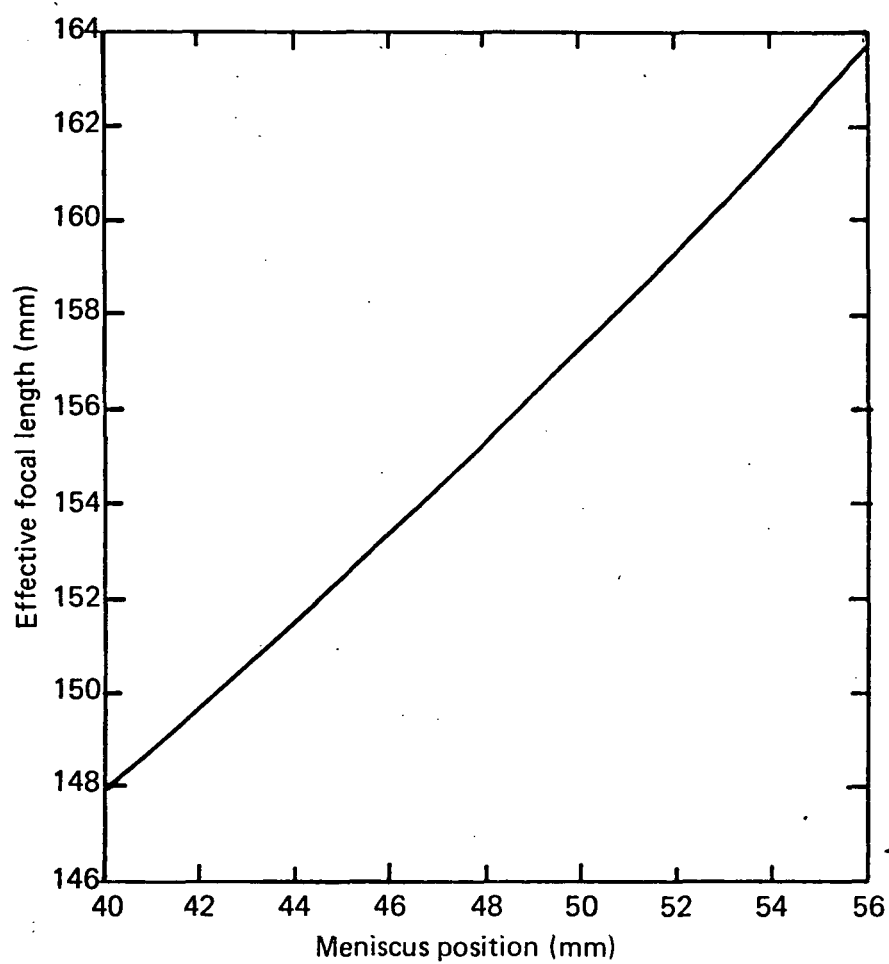
Fig. 4. Aberration generator effective focal length (GEFL) versus meniscus position.
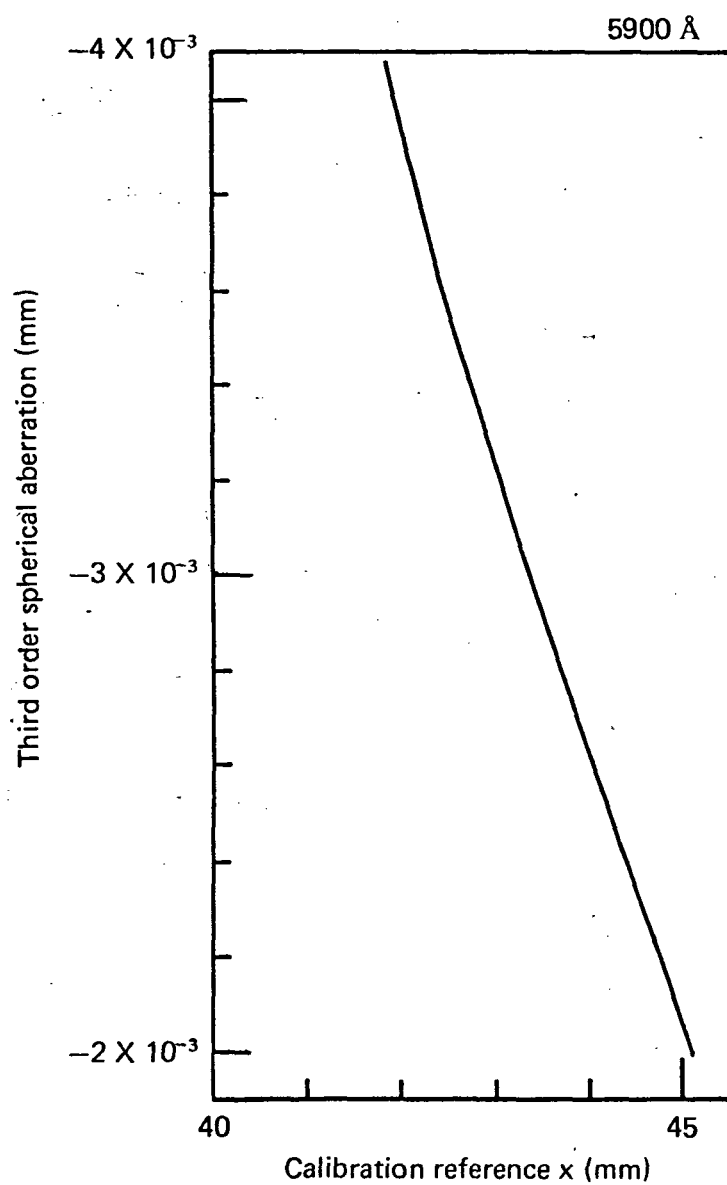
Fig. 5. Third-order spherical aberration as a
function of meniscus position for
λ = 590 nm.
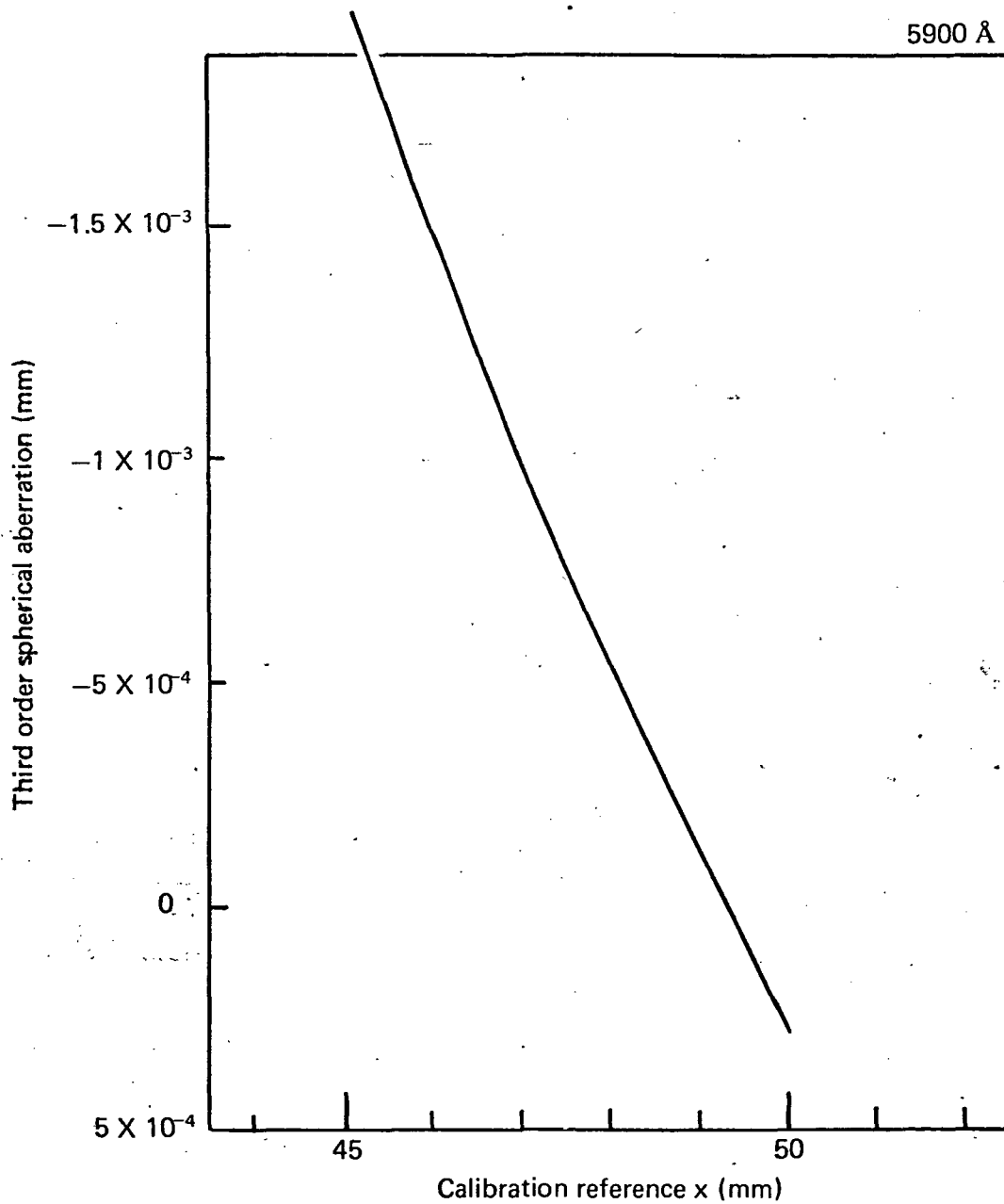
Fig. 6. Third-order spherical aberration as a function of meniscus position for λ = 590 nm.
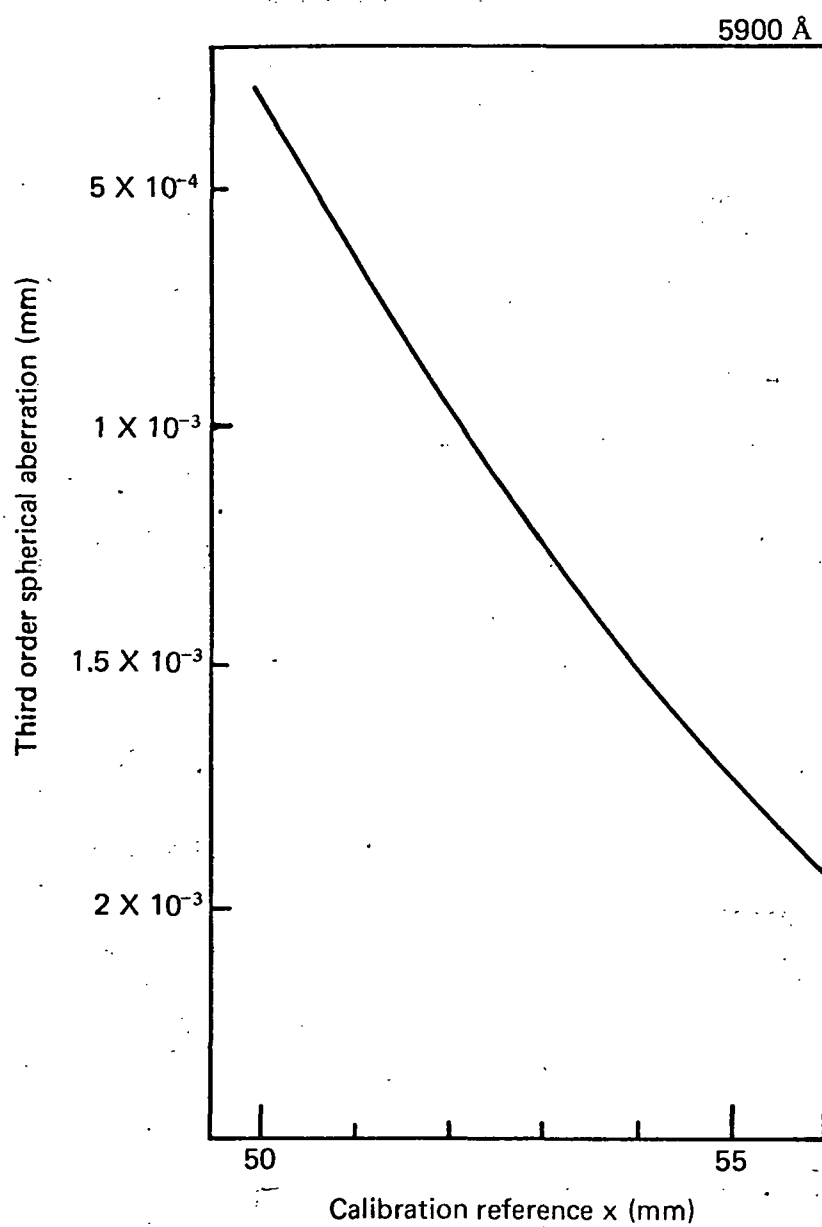
Fig. 7. Third-order spherical aberration as a function of meniscus position for $\lambda = 590$ nm.
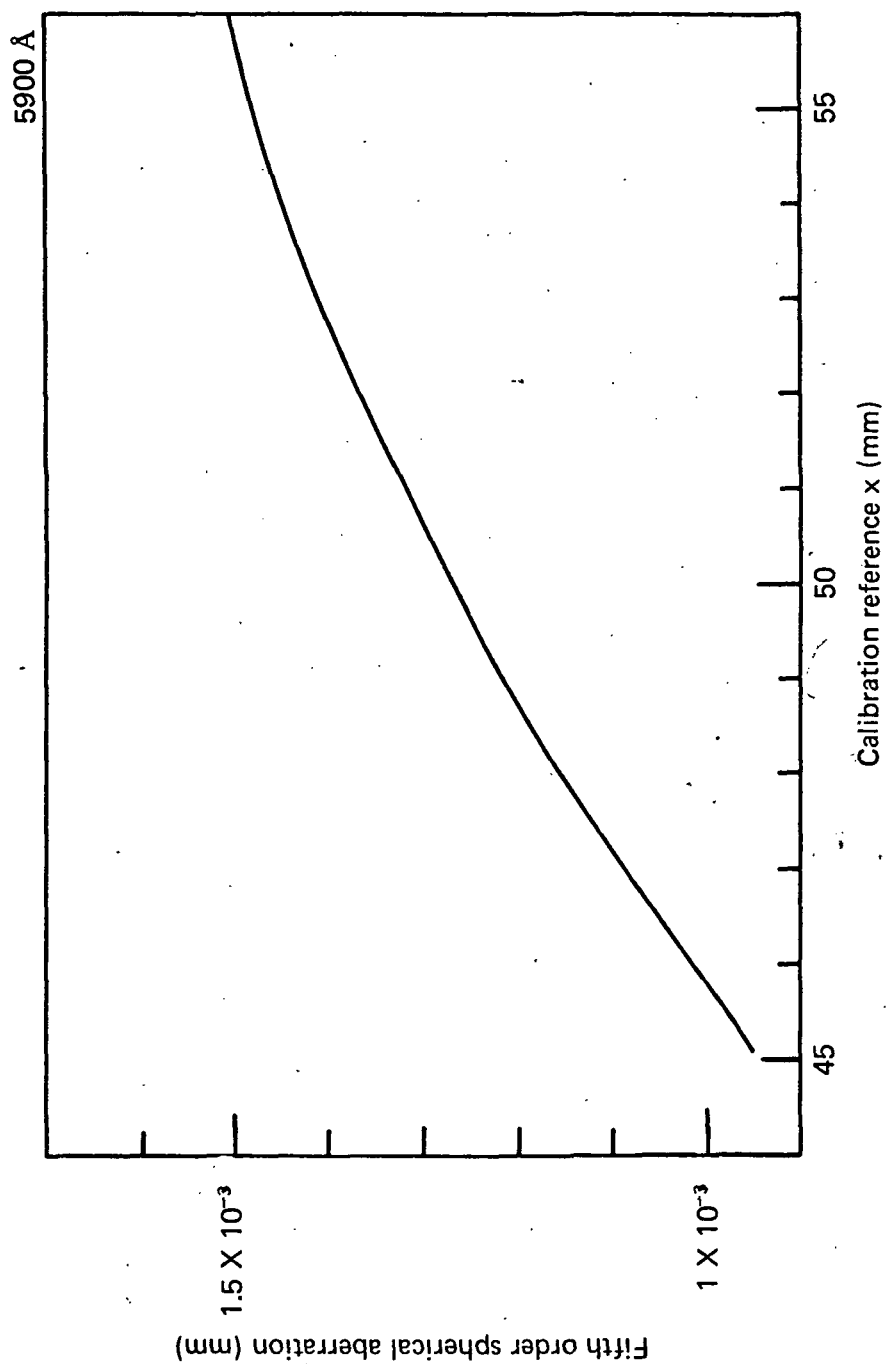
Fig. 8. Fifth-order spherical aberration as a function of meniscus position for λ = 590 nm.
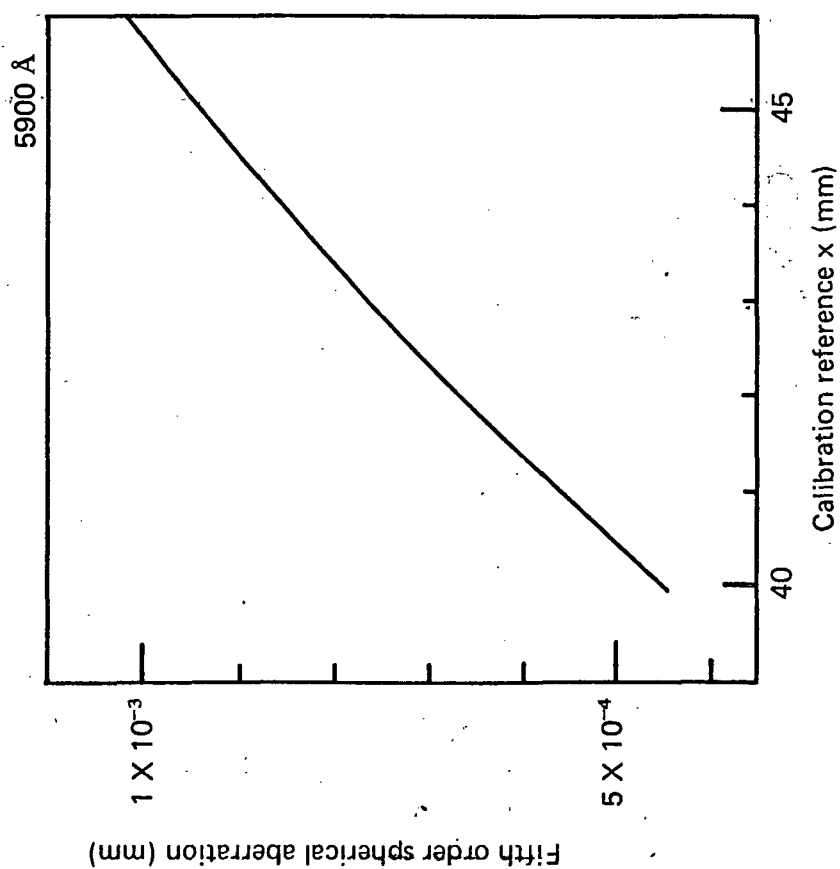
Fig. 9. Fifth-order spherical aberration as a function of meniscus position for λ = 590 nm.
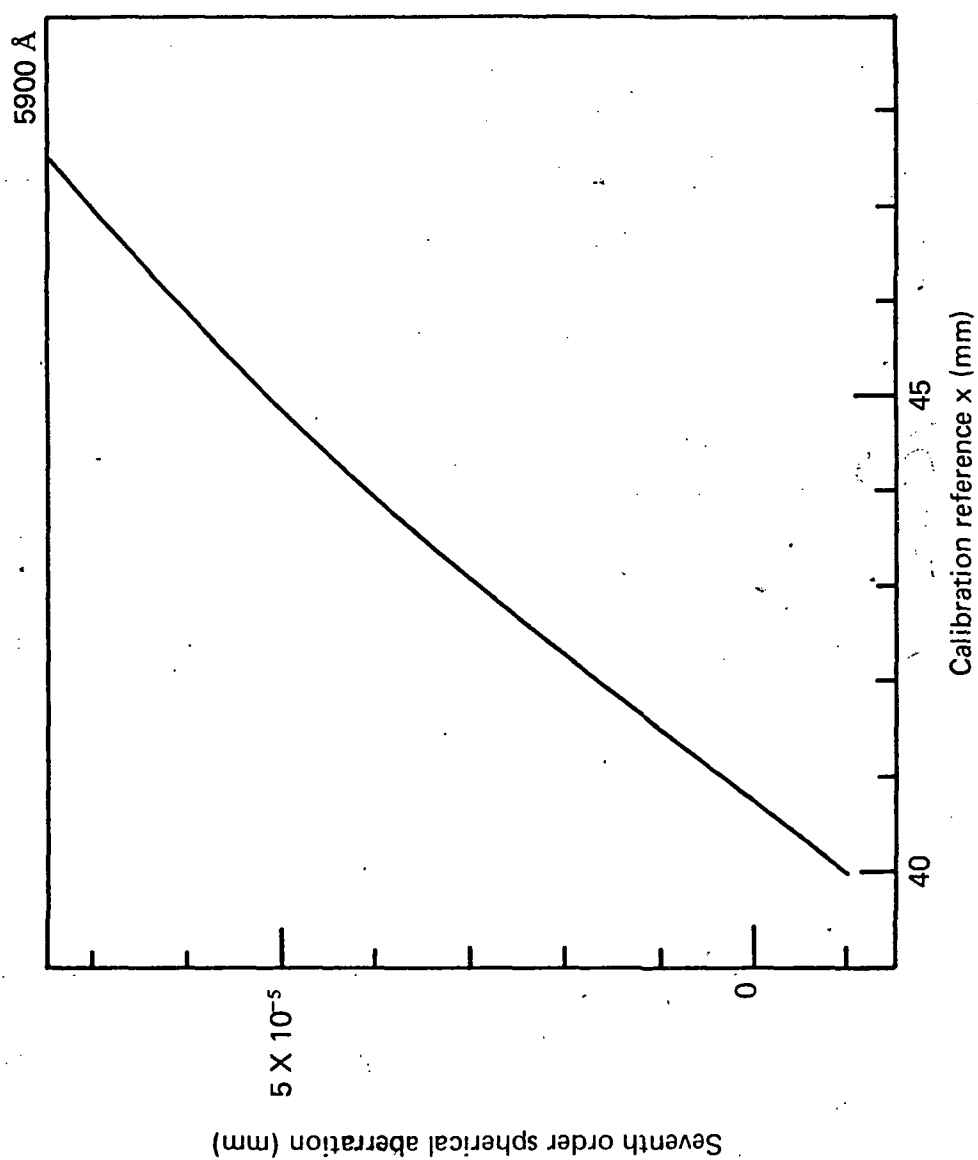
Fig. 10. Seventh-order spherical aberration as a function of meniscus position for λ = 590 nm.
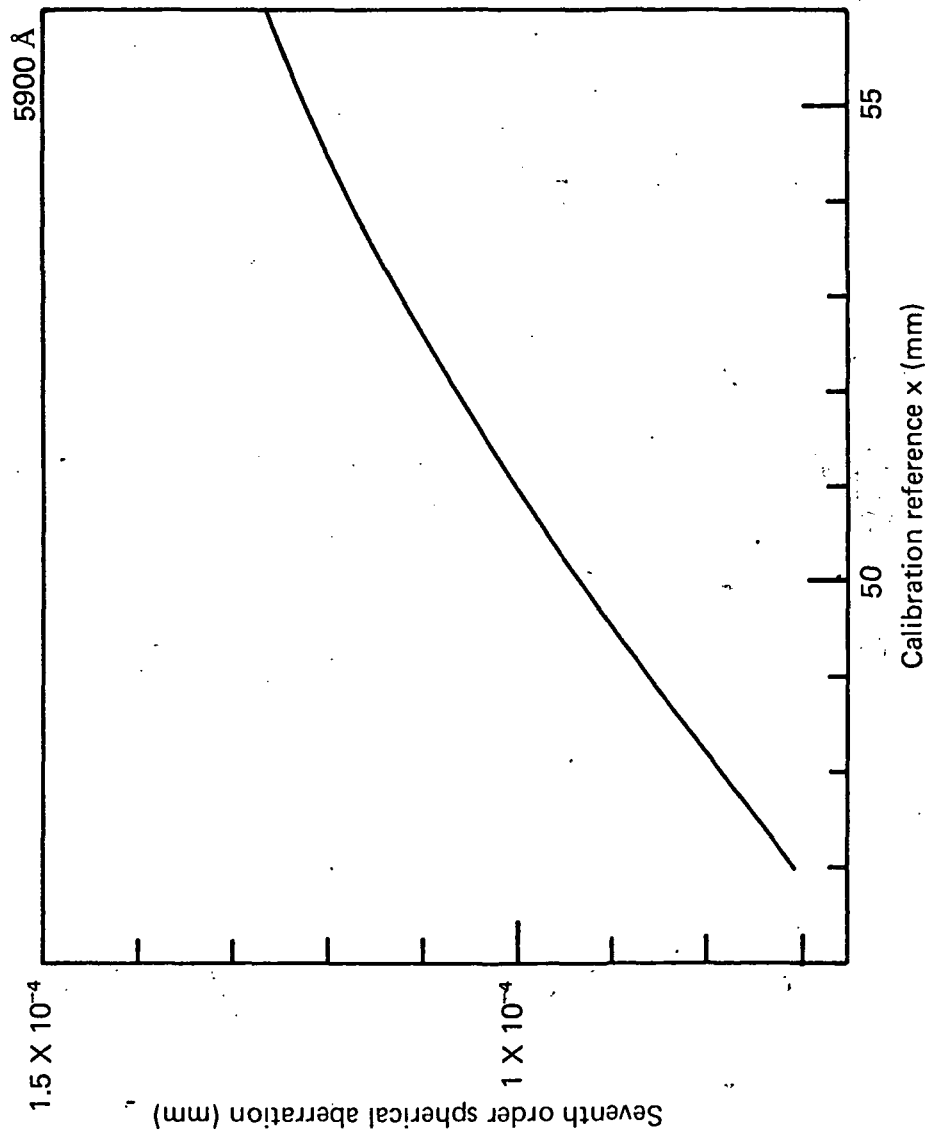
Fig. 11.   Seventh-order spherical aberration as a function of meniscus position for λ = 590 nm.
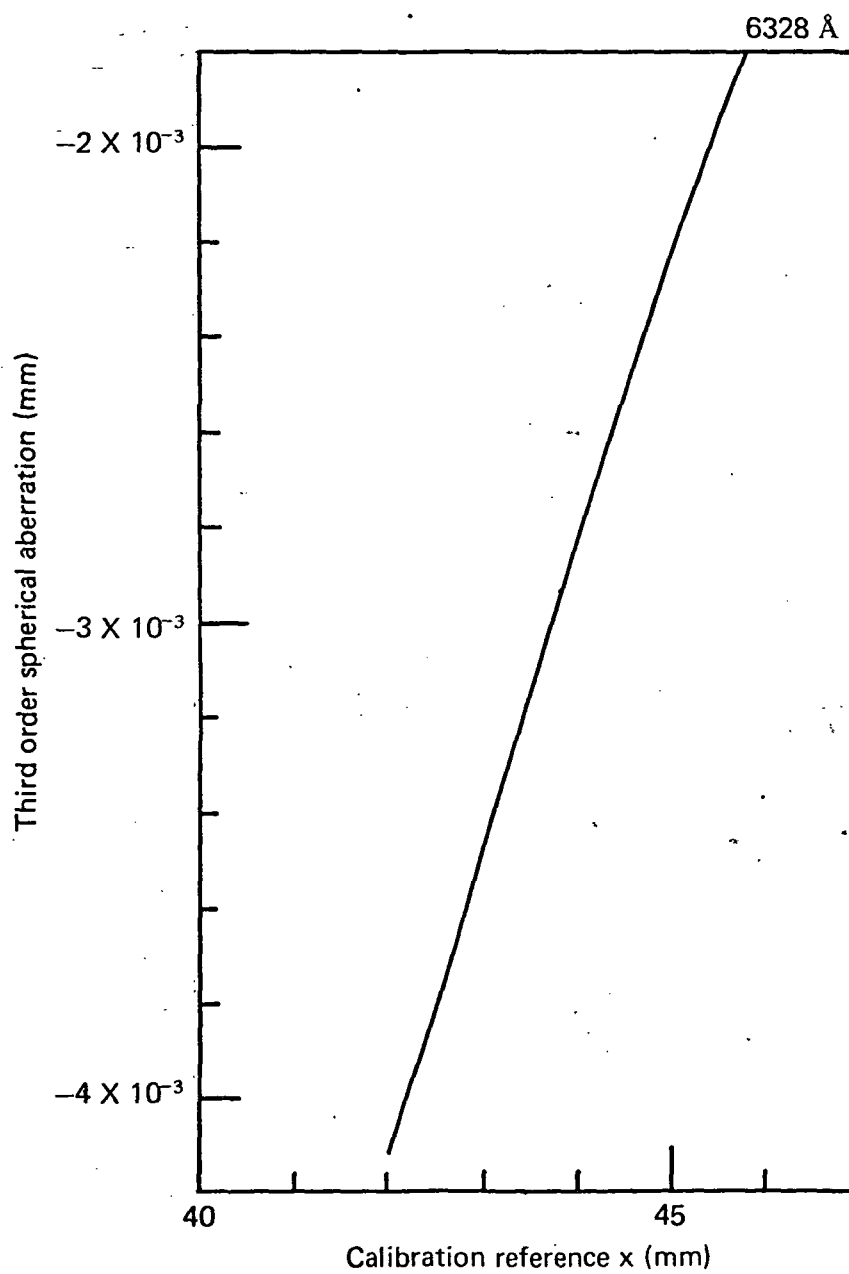
Fig. 12. Third-order spherical aberration as a function of meniscus position for $\lambda = 632.8$ nm.
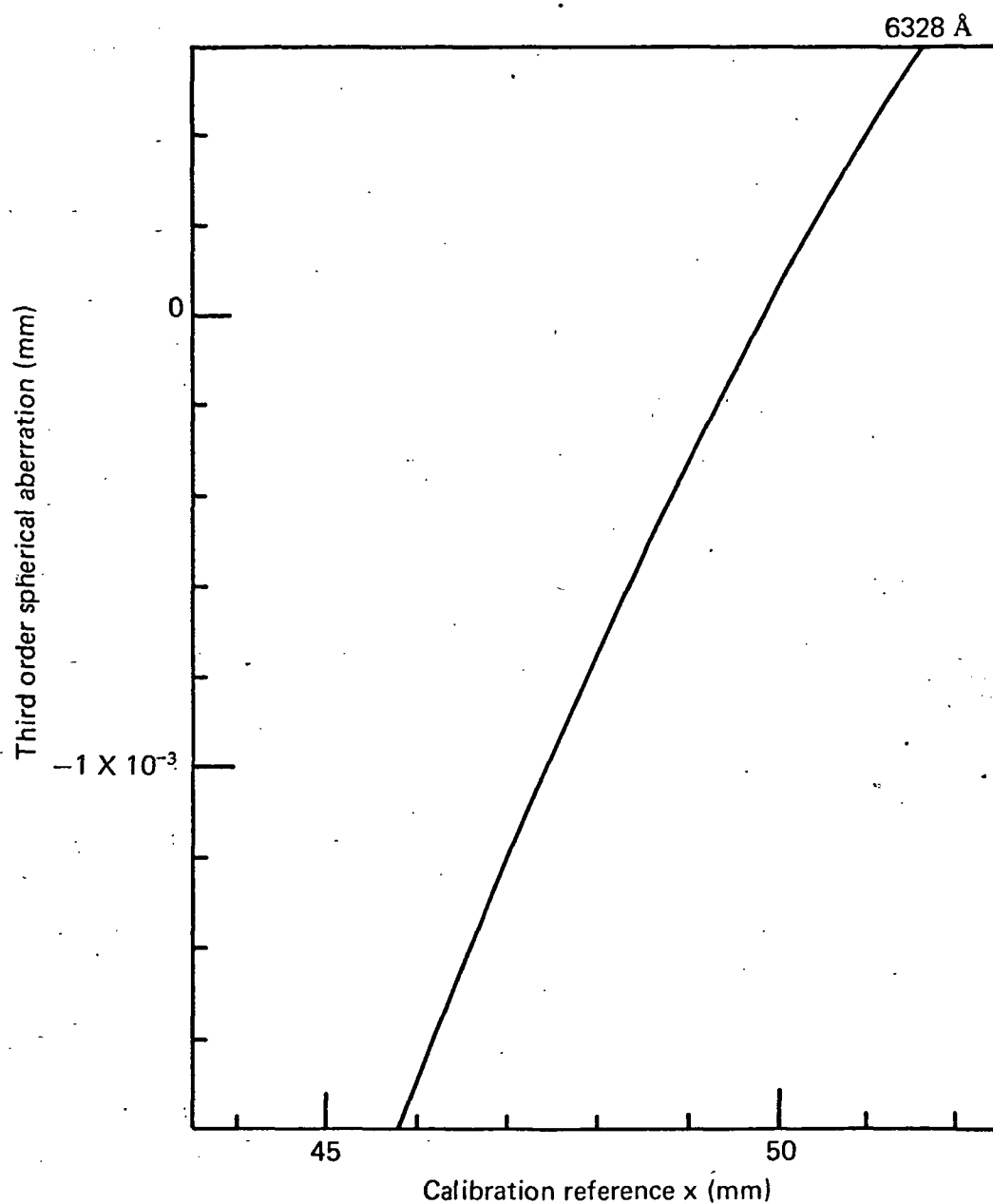
Fig. 13. Third-order spherical aberration as a function of
meniscus position for λ = 632.8 nm.
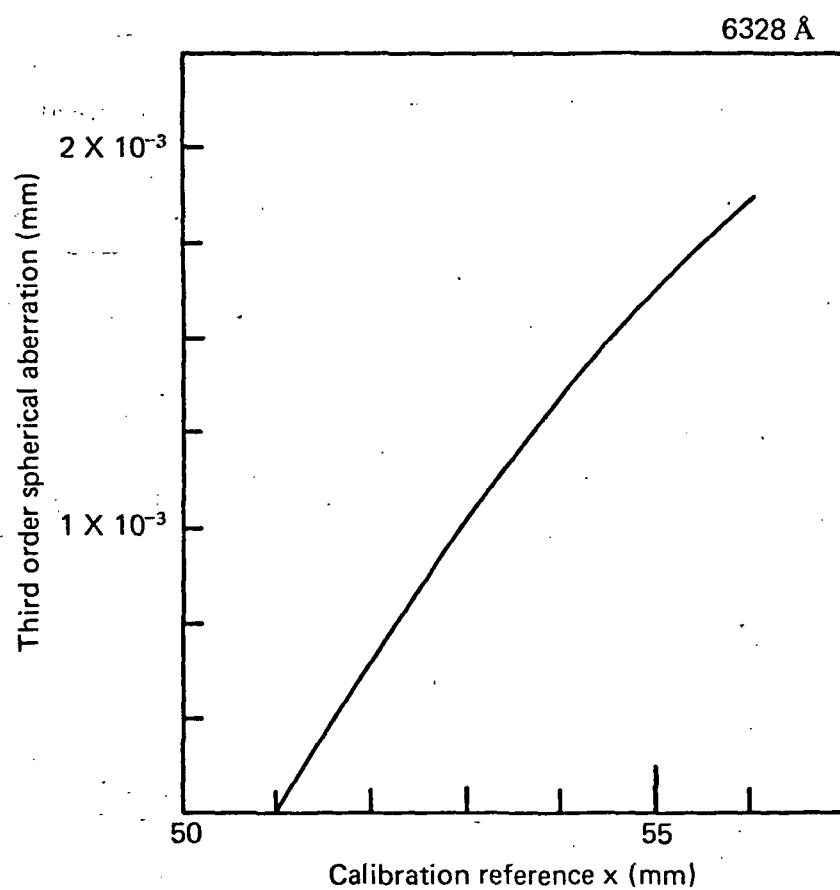
Fig. 14. Third-order spherical aberration as a
function of meniscus position for
λ = 632.8 nm.
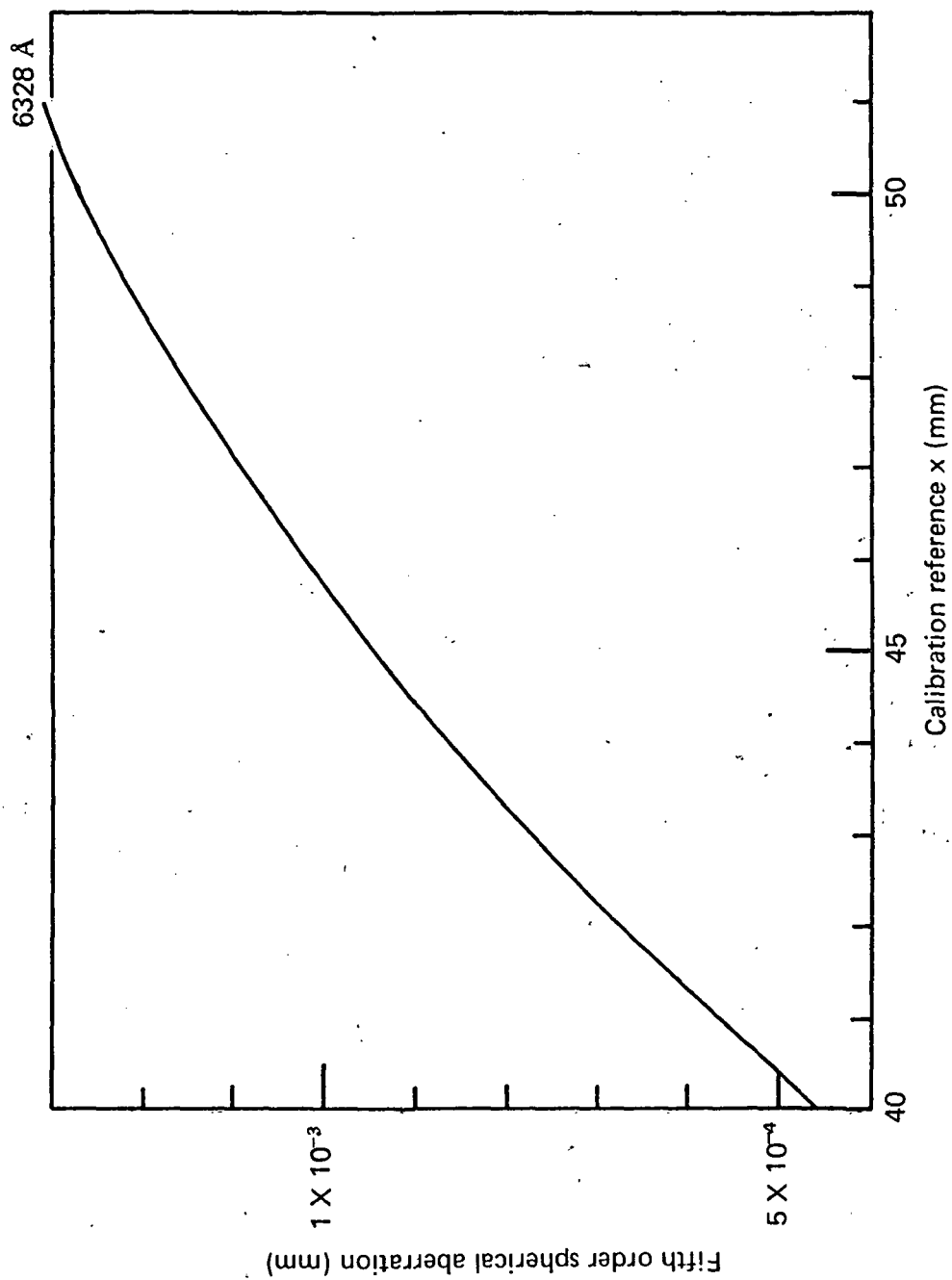
Fig. 15. Fifth-order spherical aberration as a function of meniscus position for λ = 632.8 nm.
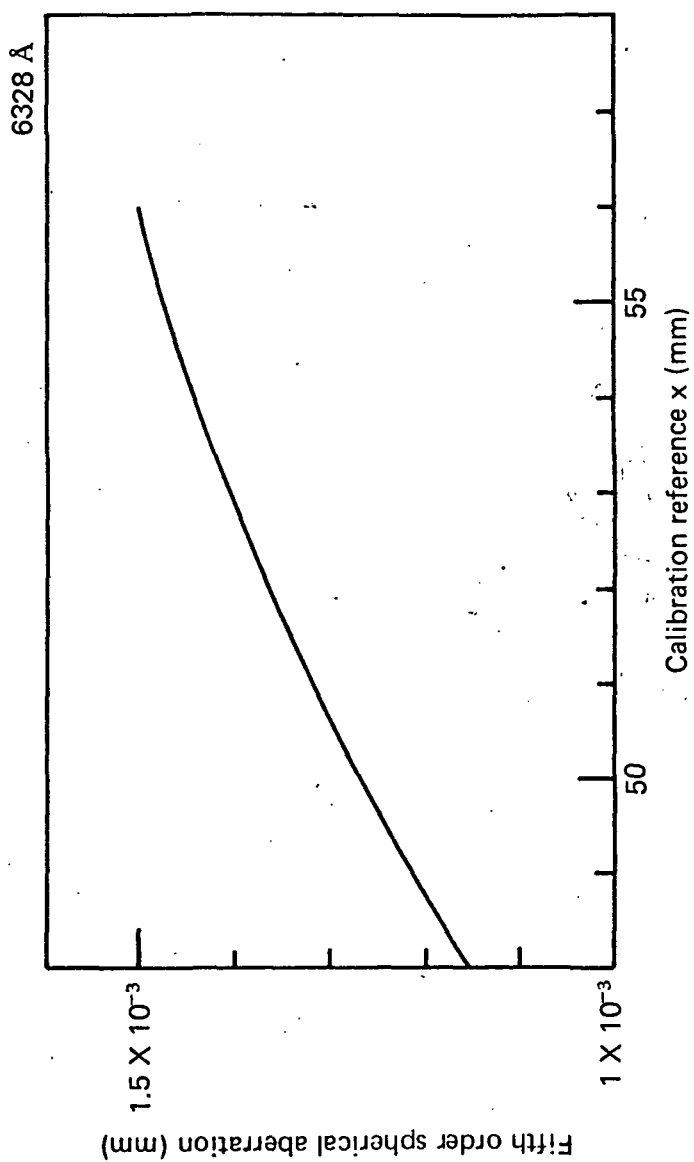
Fig. 16. Fifth-order spherical aberration as a function of meniscus
position for λ = 632.8 nm.
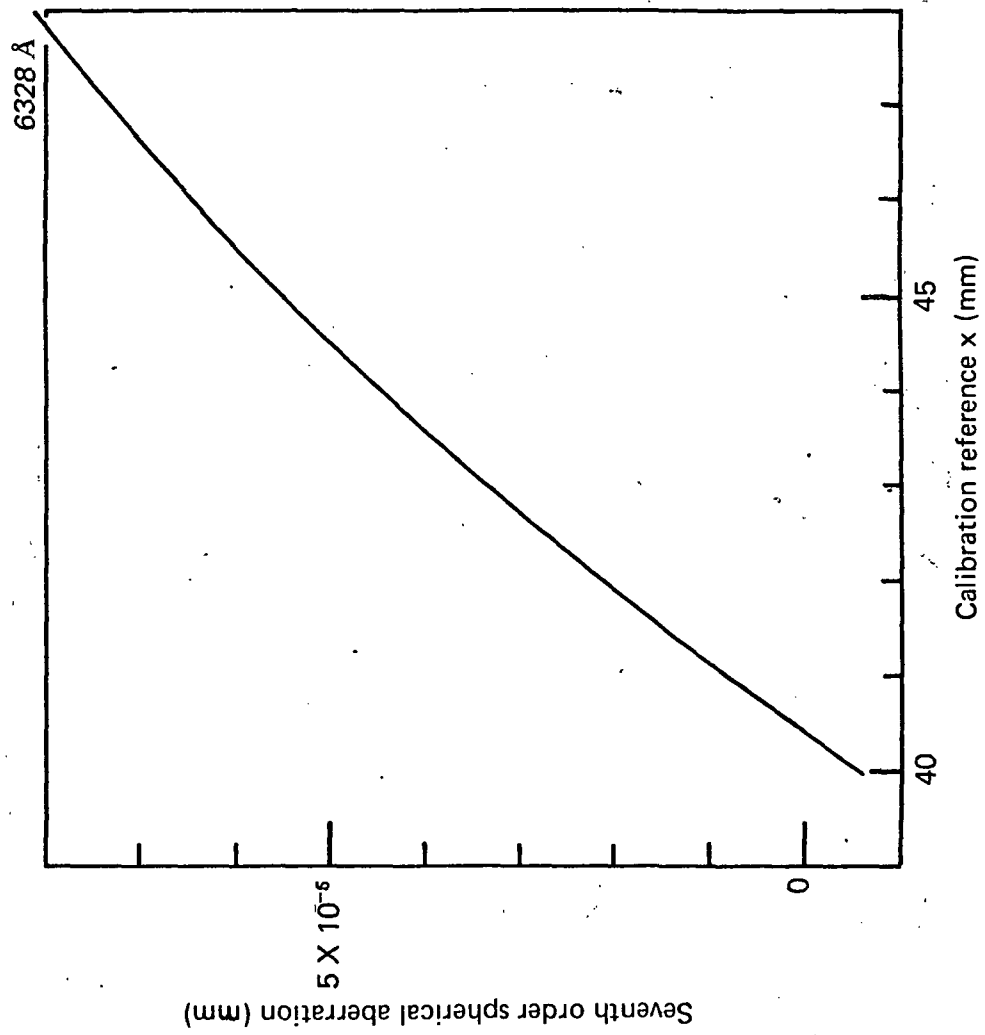
Fig. 17. Seventh-order spherical aberration as a function of meniscus position for λ = 632.8 nm.

Fig. 18. Seventh-order spherical aberration as a function of meniscus position for λ = 632.8 nm.

is to be determined experimentally in the calibration of the generator, so as to compensate for residual manufacturing errors. Using these equations and the expressions for OPD contribution of the various components of the aberration generator we can generate an overall expression for OPD introduced by the total aberration generator as follows:

$$OPD_{Total} = OPD_{Pinhole} + OPD_{Doublet} + OPD_{Plates}$$
$$+ OPD_{Meniscus} + OPD_{Relay}$$

where the optical path difference for the total aberration generator OPD_{Total} is equal to the sum of the OPD's of the individual components of the system.

The optical path difference contributed by lateral shifts in the pinhole position $OPD_{Pinhole}$ has the effect of tilting the wavefront. This is expressed as:

$$OPD_{Pinhole} = - \frac{h}{R} \beta r \cos(\phi - \alpha) = - \frac{12.7}{R} \beta r \cos(\phi - \alpha)$$

where h is the radius of the entrance pupil, R is the focal length of the aberration generator, β is the lateral distance the pinhole is located from the axial position, r is the lateral distance from the optical axis as a fraction of the pupil radius for the point on the wavefront being evaluated, ϕ is the angular position of the point on the wavefront as measured from the vertical y axis, and α is the angular position of the pinhole as measured from the vertical y axis. β and α are determined by the readings of the micrometers that position the pinhole x-y movement

stage. They are:

$$\beta = \frac{\sqrt{x^2 + y^2}}{CLEFL} = \frac{\sqrt{(AX-AXO)^2 + (AY-AYO)^2}}{CLEFL}$$

$$\alpha = \arctan \frac{X}{Y} = \arctan \frac{AX-AXO}{AY-AYO}$$

where CLEFL is the focal length of the collimating lens, and AX and AY are the readings on the micrometers for the X and Y axes respectively, and AXO and AYO are the positions of the micrometers when the pinhole is located on the optical axis. r and ϕ are determined by the readings of the micrometers on the x-y stage that positions the sampling aperture. The measurements made for r are divided by the radius h' of the pupil in the plane of the sampling aperture.

$$h' = \frac{(SEFL)(R1EFL)}{(GEFL)(R2EFL)} h$$

where SEFL is the focal length of the sampling lens*, R1EFL and R2EFL are the focal lengths of the first and second relay lenses respectively, and GEFL is the focal length of the aberration generator as determined above. Then,

$$r = \frac{1}{h'} \sqrt{x^2 + y^2} = \frac{1}{h'} \sqrt{(PX-PXO)^2 + (PY-PYO)^2}$$

$$\phi = \arctan \frac{x}{y} = \arctan \frac{PX-PXO}{PY-PYO} ,$$

where PX and PY are the readings of the micrometers that position the sampling aperture and PXO and PYO are the readings when the sampling aperture is centered about the optical axis.

*This lens recollimates the light from the second relay lens as in Fig. 1.

The optical path difference contributed by the tilt of the doublet $OPD_{Doublet}$ is expressed by

$$OPD_{Doublet} = -\tfrac{1}{2}(CMA3)r^3 U \cos\theta$$

$$= -\tfrac{1}{2}(CMA3)r^3(U_x\cos\phi + U_y\sin\phi)$$

$$= -\tfrac{1}{2}(CMA3)r^3(\tfrac{1}{0.040})\{(GXO-GX)\cos\phi + (GY-GYO)\sin\phi\}$$

where CMA3 is the amount of coma introduced by tilting the doublet 1.5^o, U is the angle of tilt from the optical axis as a fraction of the maximum angle of 1.5^o, and θ is the angular position of the point being sampled on the wavefront as it relates to the direction in which the coma is being introduced. U_x and U_y are the x and y-axis components of the angle of the doublet and are measured by GX and GY as the readings on the micrometers of the orientation device. GXO and GYO are the micrometer readings when there is no tilt in the doublet. The 0.040 factor is the micrometer movement for a tilt of 1.5^o and so gives the angle as a fraction of the angle for which CMA3 was determined.

The optical path difference contributed by the tilting and rotating of the plane-parallel plates OPD_{Plates} is expressed by

$$OPD_{Plates} = -\tfrac{1}{2}(AST3)\omega^2 r^2 \cos^2\theta'$$

$$= -\tfrac{1}{2}(AST3)\left\{\frac{2(BZ-BZO)}{15}\right\}^2 r^2\cos^2[\phi - (RZ-RZO)],$$

where AST3 is the amount of astigmatism introduced when the plates are tilted at an angle of 15° from their position of normal to the optical axis, ω is the fraction of the 15° that they are actually tilted, and θ' is the angular position of the point being sampled on the wavefront as it relates to the direction in which the astigmatism is being introduced and is equal to the difference between φ and the angle from the vertical y axis the plates are rotated. BZ is the reading on the tilt dial indicator showing the tilt and BZO is the reading when the plates are both perpendicular to the optical axis. The difference is multiplied by two because each unit division on the dial indicator is equal to 2° then divided by 15 to show the angle as a fraction of the angle for which AST3 was determined. RZ is the reading on the rotation indicator, and RZO is the reading when the plates tilt so as to introduce sagittal astigmatism in the direction of the y axis.

The optical path difference contributed by the longitudinal movement of the meniscus lens $OPD_{Meniscus}$ is represented by

$$OPD_{Meniscus} = -\frac{h^2}{2Q^2}\delta_z r^2 - \frac{1}{8}(SA3)r^4 - \frac{1}{12}(SA5)r^6 - \frac{1}{16}(SA7)r^8$$

$$= -\frac{(12.7)^2}{2(GEFL)^2}(BFP-BFPO)r^2 - \frac{1}{8}(SA3)r^4$$

$$- \frac{1}{12}(SA5)r^6 - \frac{1}{16}(SA7)r^8,$$

where δ_z is the change in focal position from the paraxial spherical aberration condition position with change of the meniscus lens position

and Q is the focal length of the aberration generator. BFP is the back focal position of the star image and BFPO is the back focal position for minimum spherical aberration. SA3, SA5, SA7, GEFL, and BFP are defined in detail above.

The optical path difference contributed by the movement of the first relay lens OPD_{Relay} is expressed by

$$OPD_{Relay} = - \frac{h^2}{2Q^2} \delta_R r^2$$

$$= - \frac{(12.7)^2}{2(GEFL)^2} (DZO-DZ)r^2,$$

where δ_R is the movement of the first relay lens. DZ is the reading of the dial gauge for the position the relay lens is at and DZO is the lens position when its focal point coincides with the focal point of the aberration generator with the meniscus lens positioned to give minimum spherical aberration.

4. Mechanical Components.

The air-spaced doublet in the aberration generator is mounted in a cell that threads into a Lansing Research Model 10.203 angular orientation device with linear micrometer adjustments. Each 0.0001" division of linear motion of the micrometers corresponds to a 13.5 arc second rotation of the lens. The cell is threaded into the orientation device until the rear nodal point of the lens coincides with the intersection of the x- and y-gimbal tilt axes. The direction and amount of coma introduced is calculated from the angle at which the doublet is tilted from the system optical axis.

The two plane-parallel plates are mounted into metal plates on individual axes parallel to one another. A toothed gear on each plate meshes with the gear on the other plate. Since both gears are of equal size, a tilt of one plate will cause an equal and opposite tilt of the other plate. One of these plates is geared to a dial indicator. Each 0.02 division on the dial is equivalent to a 2.4 minute tilt of each plate. This whole assembly is bearing-mounted so that it will rotate about the system optical axis. The bearing rotation is gear controlled. These gears also operate a digit counter where a one digit change corresponds to 1 degree of rotation about the optical axis. The amount of astigmatism is computed from the angle difference between the two plates, and the direction by tilt orientation.

The thick meniscus lens is mounted into a cell that is attached to a micrometer slide. Initially the lens is positioned so as to give minimum spherical aberration for the system. The lens can then be moved toward or away from the air-spaced doublet and parallel plates to put various amounts of positive or negative spherical aberration into the system. The travel of the lens is measured with a dial gauge having a 25-mm travel and reading to 0.01 mm. The amount of spherical aberration is calculated from the distance between the adjusted position of the meniscus lens and its nominal position when the system has minimum spherical aberration.

The two cemented doublets for the relay optics are mounted in individual cells. The cell for the first lens is mounted on a micrometer slide and is positioned so that its focal point coincides with the image

formed by the aberration generator. As the image point moves along the optical axis when the meniscus lens is moved, the first relay lens is moved on its micrometer slide so as to keep its focal point and the image in coincidence. This keeps the beam coming from this lens collimated. The collimated beam is then brought to a focus by the second lens, an f/12 telescope object. A photograph of the complete assembly appears in Fig. 19.
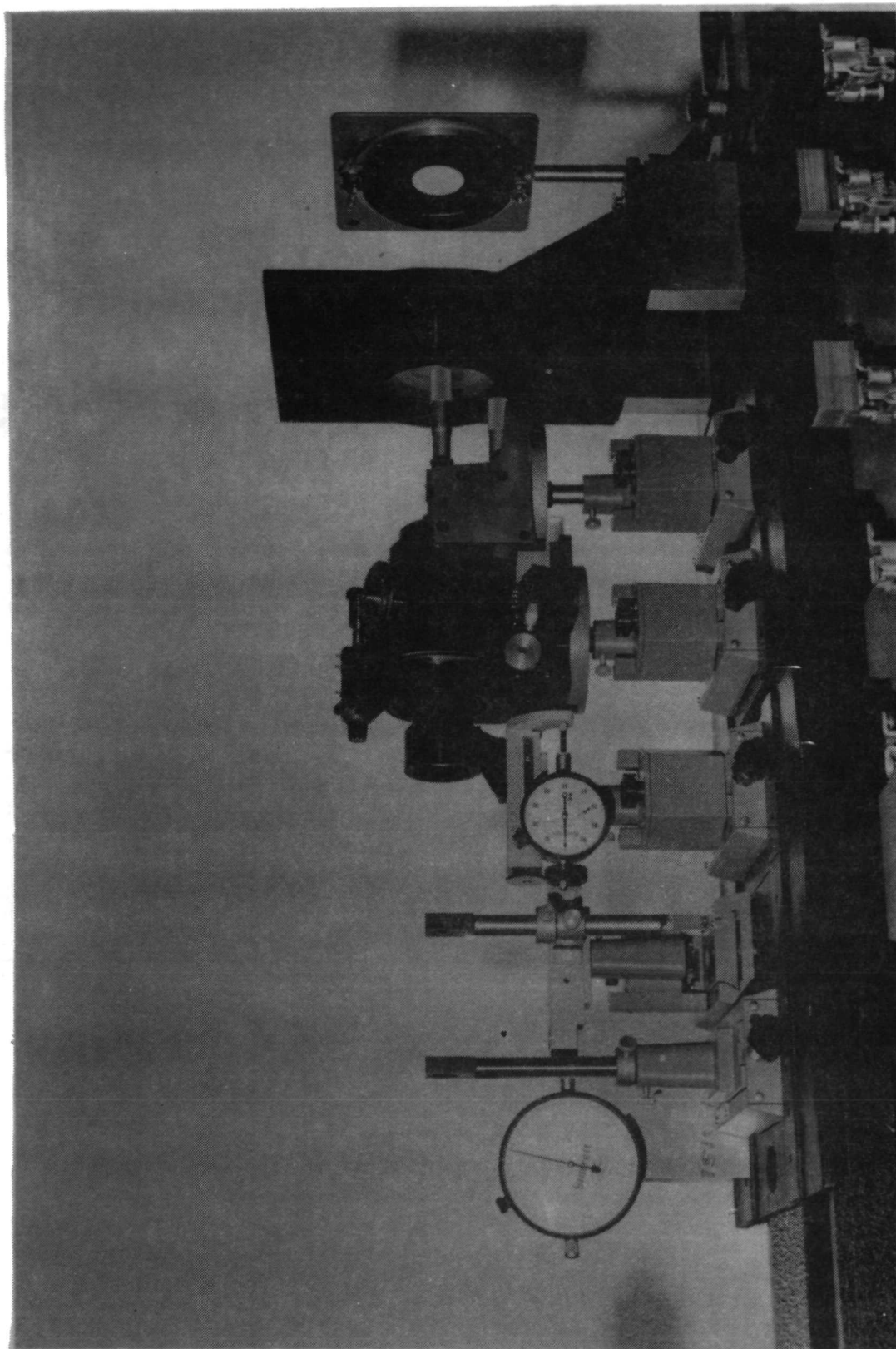
Fig. 19. Aberration generator and relay system.

CHAPTER III

THE COARSE RANGE SENSOR

1. General.

Several types of coarse range (geometrical) optical tests were considered. Three of the most common are the Foucault knife-edge test, the wire test and the Ronchi test. Effectively, in each of these types of tests, a particular type of obscuration mask (knife edge, wire, multiple wire) is placed in the vicinity of the focal plane. Knowing the mask parameters and location and by measuring shadow locations on the pupil, one can obtain ray slope information and, by integration, wavefront data. However, these tests suffer from a common flaw in that the test mask has to be rotated for nonsymmetric aberrations like astigmatism and coma. Also, to obtain meaningful error measurements we need to scan the pupil. A test that is at least as sensitive as the above and which does not require mask rotation and control, and by which we can monitor any point on the pupil we wish is the Hartmann test.

2. The Hartmann Test.

a. General arrangement.

In the classical application of the Hartmann test a mask of precisely located holes is placed in the exit pupil of the optical system. Each hole lets through a particular ray converging toward focus. Two

photographic plates are exposed, one in front of focus and the other be-
hind. By knowing the distance between the plates and by reading out on a
comparator the positions of the rays on the plates, a slope can be
determined for each ray in the pupil.

This classical form of the Hartmann test is obviously not suited
for remote testing. However, as illustrated in Fig. 20, only a simple
modification is required. Plane A indicates the optical system exit
pupil. We position lens B so that its rear focal point lies at the sys-
tem focus. At location C we have the reimaged optical system pupil in
collimated light space. In this relayed space we can sample a particular
pupil location conveniently by means of a moveable aperture. Any depar-
ture from a perfect system wavefront will show up in the sampled ray as a
small angular deviation from collimated light. The slope error in the
system exit pupil at this corresponding point can be found easily by
multiplying the measured angular departure by the ratio of the relay lens
focal length to the system focal length. This technique allows us to
sample any pupil location we so desire using the full energy spectrum
available, with an increased sensitivity equal to the focal length ratio.

i. Automatic readout.

We are now left to readout the angular deviations of these vari-
ous rays. A suggested automatic technique involves the use of an image
dissector tube of the star tracker variety. The arrangement
is indicated in Fig. 20. The second lens D focuses the particular ray
bundle we are sampling at its rear focal plane at some position off-axis
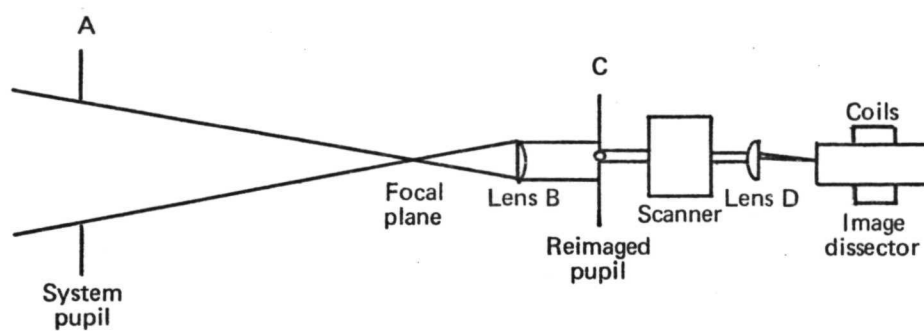
Fig. 20. Hartmann sensor configuration. In summary the advantages are: (1) a priori geometric knowledge, (2) alignment insensitivity, (3) simple and efficient data reduction, and (4) high efficiency light usage.
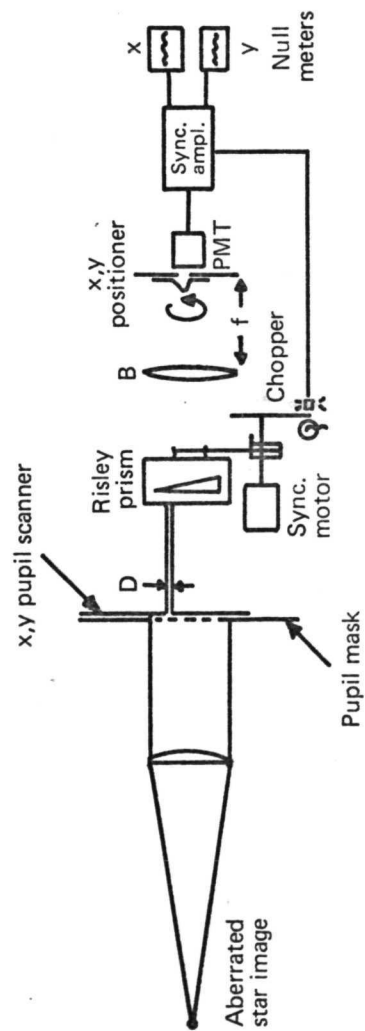
Fig. 21 Laboratory Hartmann test simulator.

which depends on the slope error and the sampled pupil position. The
image dissector measures this off-axis location. This position divided
by the lens D focal length is the magnified slope error at the pupil
position.

The dissector tube consists of a photocathode that has been
deposited within a transparent window. An electrostatic focusing system
refocuses the electron image produced by the sampled ray bundle within or
in the vicinity of a metallic plate containing a circular aperture in its
center. Those electrons getting through the aperture produce a current.
An orthogonal set of magnetic coils are phased 90° apart with equal
deflection amplitude thus producing a circular scan of the electron image
about the metallic circular aperture. Synchronous amplification of the
resulting signal is carried out about the scanning frequency. If the ray
image is perfectly centered in its scan about the circular disc, then
there is no synchronous error signal produced. However, if the ray
bundle is displaced, an A.C. error signal is produced with some particu-
lar phasing depending upon the ray position. From this we extract an
X,Y-axis error signal which can then be applied as an offset signal to
the deflection coils until the error signals are nulled. Knowing the
calibration on the offset deflection we obtain the ray position.

ii. Simulated automatic readout.

This scheme has been simulated in the laboratory using a Risley
prism scanner, a moveable pinhole and standard PMT. This is illustrated
in Fig. 21. Lens B focuses a particular ray bundle on or near the

pinhole. This diffraction image is spun about the pinhole by a Risley prism whose orientation has been adjusted to give a circular spin diameter equal to the pinhole diameter. A mechanical chopper driven by the prism motor at 30 cps gives a reference signal phased on the x axis. Behind the pinhole is an E.M.R. 9858 photomultiplier tube. As the image is moved around the pinhole any offset would produce a 30 hertz variation in the PMT output current. As illustrated in Fig. 22 this 30 hertz signal is preamplified and converted into a voltage signal. The voltage signal is then fed into a synchronous amplifier which first filters and amplifies the incoming signal and then splits the signal into two identical components 90° apart in phase. Each component is connected to the input of a phase-sensitive demodulator where the signal is mixed with the reference voltage signal to produce sum and difference currents. A filter at the output of the phase-sensitive demodulator rejects the high frequency (sum) frequencies and passes the zero or DC difference component corresponding to the component of the signal spectrum at the reference frequency. This zero-frequency current is the error signal output. We have two of these, one in-phase, indicating the x-axis displacement, and a quadrature signal, indicating the y-axis displacement. By moving the collection pinhole we can first zero out the x-error and then the y-error signals, read the micrometers and calculate our wavefront slope errors. Figure 22 is a photograph of the Hartmann test wavefront simulator being evaluated by the aberrated telescope.
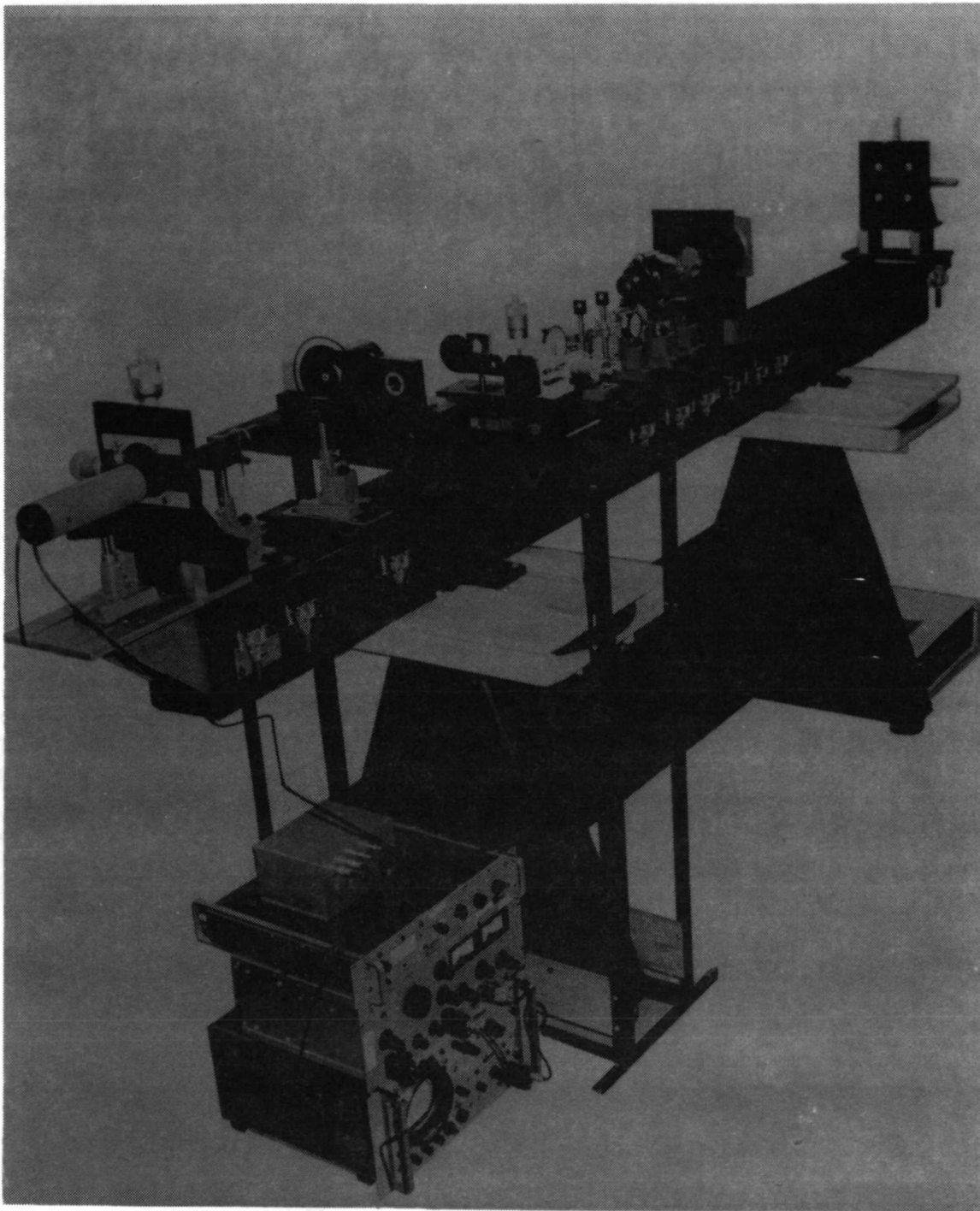
Figure 22. Hartmann Test Simulator and Aberrated Telescope Wavefront Simulator.

b. Theoretical discussion.

We have begun to investigate several theoretical problems concerning the Hartmann test. These include an examination of the effect of sampling aperture size in the exit pupil on measurement of primary aberrations and detection sensitivity. It also includes the basis for determining the optimum size scanning pinhole for subsequent S/N ratio calculations.

i. Effects of sampling aperture on third-order aberrations.

The Hartmann test is used to measure the slope of a ray in the exit pupil of an optical system. By integration one may obtain the wavefront of the optical system under test.

Ideally, we would like to make use of information from one point in the pupil, but since we are concerned about energy and diffraction we need a finite aperture for each ray. The question then arises: How does the aperture size affect our measurement of the ray slope, since we are integrating over a finite area of wavefront? In the following discussion we develop quantitatively a wavefront error measurement expression in terms of relative Hartmann aperture size and aberration type. Diffraction effects are considered in ii.

The *assumption is made that we have a measuring scheme that will locate the centroid of the image of the Hartmann aperture.* Thus we are determining the average slope of rays in a Hartmann aperture and comparing it to the slope of the ray at the center of the Hartmann aperture.
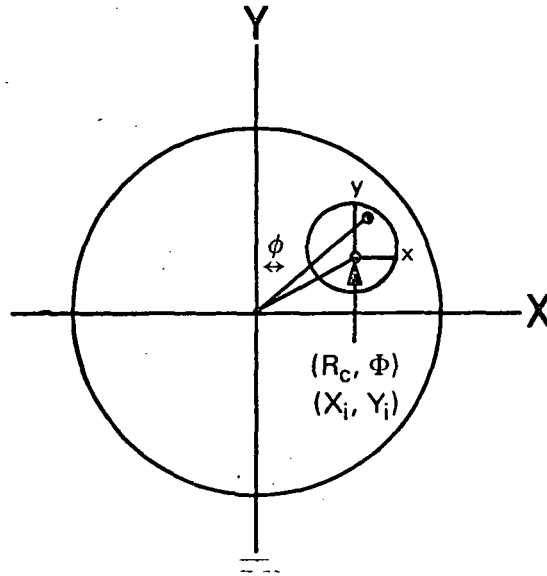
Fig. 23. Telescope system exit pupil.

The exit pupil of the system is illustrated in Fig. 23. In a normalized system $X^2 + Y^2 \leq 1$. The center of the Hartmann aperture is located at (R_c, Φ). Our analysis here restricts $R_c \leq 1 - D$, where D is the radius of the Hartmann aperture. Obviously $Y = R_c \cos\Phi + y$; $X = R_c \sin\Phi + x$.

If S_{xXY} is the x-direction slope of the wavefront at X, Y, then the average x-direction slope in the aperture centered around R_c, Φ is:

$$\overline{S}_{xX_iY_i} = \frac{\displaystyle\int_{-D}^{+D} \int_{-(D^2-x^2)^{\frac{1}{2}}}^{(D^2-x^2)^{\frac{1}{2}}} S_{xXY}\,dx\,dy}{\pi D^2} .$$

Likewise the average slope in the y-direction is:

$$\overline{S}_{yX_iY_i} = \frac{\int_{-D}^{+D} \int_{-(D^2-x^2)^{1/2}}^{(D^2-x^2)^{1/2}} S_{yXY} dxdy}{\pi D^2}$$

Now let us consider several aberration types, and their measurement errors introduced in the Hartmann test.

Defocus

$$W = W_{020}(X^2 + Y^2)$$

$$S_{xXY} = \frac{\partial W}{\partial X} = 2 W_{020} X$$

$$S_{yXY} = \frac{\partial W}{\partial Y} = 2 W_{020} Y$$

In our small displaced aperture D,

$$W = W_{020}(R_c^2 + x^2 + y^2 + 2R_c\left[x \sin\Phi + y \cos\Phi\right])$$

$$S_{xXY} = \frac{\partial W}{\partial x} = W_{020}(2x + 2R_c\sin\Phi)$$

$$\overline{S}_{xX_iY_i} = \frac{\iint S_{xXY}}{\pi D^2} = \frac{\iint (2x + 2R_c\sin\Phi)dxdy}{\pi D^2}$$

The first term integrates to zero and we are left with

$$\overline{S}_{xX_iY_i} = 2W_{020}R_c\sin\Phi = 2W_{020}X_i$$

or

$$\overline{S}_{xX_iY_i} = S_{xX_iY_i}$$

or the average x-slope in the aperture D is equal to the actual x-slope at the center coordinate of D for the defocus aberration. Likewise,

$$\overline{S}_{yX_iY_i} = S_{yX_iY_i}.$$

Thus defocus in the absence of other aberrations causes no shift in the Hartmann image centroid.

Tilt

The wavefront aberration for tilt is $W = W_{y111}Y + W_{x111}X$ where W_{y111} is a tilt of wavefront in the Y-direction.

$$S_{xX_iY_i} = \frac{\partial W}{\partial X} = W_{x111}(\text{x-slope at } X_iY_i)$$

$$W = W_{y111}(R_c\cos\Phi + y) + W_{x111}(R_c\sin\Phi + x)$$

$$S_{xXY} = \frac{\partial W}{\partial X} = W_{x111}$$

$$\overline{S}_{xXY} = \frac{\iint W_{x111}dxdy}{\pi D^2} = W_{x111}.$$

Thus,

$$\overline{S}_{x_{XY}} = S_{x_{X_iY_i}} \ .$$

We see that in the absence of other aberrations a tilt causes no shift in the Hartmann image centroid.

Astigmatism

The wavefront for astigmatism is

$$W = W_{222}\rho^2\cos\Phi^2 = W_{222}Y^2$$

$$S_{y_{X_iY_i}} = 2W_{222}Y_i$$

$$W = W_{222}(y^2 + R_c^2\cos\Phi + 2yR_c\cos\Phi)$$

$$S_{y_{X_iY}} = \frac{\partial W}{\partial y} = 2W_{222}R_c\cos\Phi = 2W_{222}Y_i + 2yW_{222}$$

$$+ 2yW_{222}$$

$$\overline{S}_{y_{XY}} = \frac{\iint (2W_{222}Y_i + 2yW_{222})dxdy}{\pi D^2} \ .$$

The second integral is zero. Thus,

$$\overline{S}_{y_{XY}} = 2W_{222}Y_i = S_{y_{X_iY_i}} \ .$$

Again astigmatism does not cause a centroid shift.

Spherical and Coma

Thus far with defocus, tilt and astigmatism we have seen that the Hartmann centroid is not shifted due to the sampling aperture size. We will see that for spherical and coma third-order aberrations, that this is not the case. That is, the finite aperture in the Hartmann test introduces a certain error of predictable form and magnitude depending on the relative Hartmann aperture size.

Spherical

$$W = W_{040}(X^2 + Y^2)^2$$

$$S_{x_{X_iY_i}} = 4W_{040}X_iR_c^2$$

$$S_{y_{X_iY_i}} = 4W_{040}Y_iR_c^2.$$

In the Hartmann aperture:

$$W = W_{040}(R_c^2 + y^2 + x^2 + 2R_c[x \sin\Phi + y \cos\Phi])^2$$

$$S_{x_{XY}} = \frac{\partial W}{\partial x} = 2W_{040}(R_c^2 + y^2 + x^2 + 2R_c$$

$$[x \sin\Phi + y \cos\Phi]) \cdot (2x + 2R_c\sin\Phi)$$

$$= 4W_{040}[xR_c^2 + xy^2 + x^3 + 2X_ix^2 + 2Y_ixy]$$

$$+ 4X_iW_{040}[R_c^2 + (x^2 + y^2) + 2X_ix + 2Y_iy].$$

All odd functions integrate to zero as indicated by the $\checkmark$. We are left with:

$$\overline{S}_{x_{X_i Y_i}} = 8W_{040}X_i \frac{\iint x^2 dx dy}{\pi D^2} + 4X_i W_{040}R_c{}^2$$

$$+ 4X_i W_{040} \frac{\int_0^{2\pi}\int_0^D \rho^2 \rho d\rho d\theta}{\pi D^2}.$$

$$\overline{S}_{x_{X_i Y_i}} = S_{x_{X_i Y_i}} + 2D^2 X_i W_{040} + W_{040}X_i D^2.$$

By symmetry:

$$\overline{S}_{y_{X_i Y_i}} = S_{y_{X_i Y_i}} + 2D^2 Y_i W_{040} + W_{040}Y_i D^2$$

$$W_{Measured} = \int_0^{X_M} \overline{S}_{x_{X_i Y_i}} dX_i + \int_0^{Y_M} \overline{S}_{y_{X_i Y_i}} dY_i$$

$$W_{Measured} = W_{040}(X_M{}^2 + Y_M{}^2)^2 + 3W_{040}\left[D^2\right] \cdot \left[X_M{}^2 + Y_M{}^2\right]$$

$$W_{Measured} = W_{040}R_M{}^4 + 3W_{040}D^2 R_M{}^2.$$

We see that when we measure spherical aberration with a Hartmann array we get an additional term in our measurement, which takes the form of a focusing error with coefficient $3W_{040}D^2$. However, since we have obtained the functional form of the associated error we can now apply this knowledge to a correction term on our defocus measurement and thus compensate for the finite Hartmann aperture size.

Coma

$$W = W_{131}\rho^3\cos\Phi = W_{131}(X^2 + Y^2)Y$$

$$S_{x_{X_iY_i}} = \frac{\partial W}{\partial X} = 2W_{131}X_iY_i$$

$$S_{y_{X_iY_i}} = \frac{\partial W}{\partial Y} = W_{131}(X_i^2 + Y_i^2) + 2W_{131}Y_i^2$$

$$S_{x_{XY}} = \frac{\partial W}{\partial x} = 2W_{131}(xy + xR_c\cos\Phi + yR_c\sin\Phi) + S_{x_{X_iY_i}}$$

Since the first three terms integrate to zero

$$\bar{S}_{x_{XY}} = S_{x_{X_iY_i}}$$

Thus there is no x-component of slope error. However,

$$S_{y_{XY}} = \frac{\partial W}{\partial y} = S_{y_{X_iY_i}} + W_{131}(\rho^2 + 2R_cx\sin\Phi + 3R_cy\cos\Phi)$$

$$+ 2W_{131}(y^2 + 2yR_c\cos\Phi).$$

Integrating we obtain:

$$\bar{S}_{y_{XY}} = S_{y_{X_i Y_i}} + W_{131}D^2.$$

Since

$$W_{Measured} = \int_0^{X_M} \bar{S}_{x_{XY}} + \int_0^{Y_M} \bar{S}_{y_{XY}} dY$$

$$W_{Measured} = W_{131}(X_M{}^2 + Y_M{}^2)Y_M + W_{131}Y_M D^2.$$

We thus see that in the case of coma, a finite size Hartmann aperture will introduce an error which takes the form of a tilt aberration. This information can be used as a correction on tilt measurement.

Conclusions

We see from the preceding discussion that if we are measuring the Hartmann centroid the only third-order aberrations that introduce errors are spherical and coma, and that the amounts of error are extremely small. We could predict the amounts of error for these aberration measurements by using the error formulas developed. We can also take advantage of our knowledge of the aberrational form of error to eliminate it. If we were monitoring an active system and were looking for changes, and we measured a change in spherical aberration we would also be able to predict the defocus type error that would be associated with it and thus not confuse it with an actual defocus change. The same argument holds for the coma and tilt error.

ii. Optimal signal recording geometry.

In order to calculate the signal generated by the slightly off-center diffraction image of a sampled bundle of rays we must know the nature of the diffraction pattern formed on the image dissector's face, the impulse response of the tube and the dimensions of the collecting aperture within the tube. The convolution of these three quantities will give us the normalized amount of energy passing into the dissector for a given diffraction image collecting aperture displacement. From this convolution curve we can determine the change in signal current for a change in position of the diffraction pattern on the tube face due to a slope error. Thus we will be able to make signal predictions based upon star source characteristics, f/no. of sampled pupil area, tube scanning aperture sizes and tube impulse response characteristics.

Referring to Fig. 21 let D be the sampling aperture size, f the lens focal length and λ the average wavelength of the collimated light. The intensity distribution in the image dissector collecting plane for a unit amplitude disturbance is

$$I(r) = \frac{\pi^2 D^4}{16\lambda^2 f^2} \left[\frac{2J_1(\frac{\pi D r}{\lambda f})}{(\frac{\pi D r}{\lambda f})} \right]^2 .$$

The impulse response of the dissector tube is approximately Gaussian and can be written as

$$G(r) = \frac{1}{2\sigma^2} e^{-\frac{\pi r^2}{2\sigma^2}} .$$

Here σ is the Gaussian width of the response. The collecting aperture can be represented by $H(r) = \text{circ}(r/\ell/2)$, which is a function such that

$$H(r) = 1 \qquad 0 \leq r \leq \frac{\ell}{2}$$

$$H(r) = 0 \qquad r > \frac{\ell}{2}$$

The energy getting through the aperture for a displaced diffraction image is

$$L(r) = I(r)*G(r)*H(r),$$

where * is convolution, and r is the coordinate of the diffraction image.

Taking the Fourier transform (F)

$$FL(r) = FI(r) \cdot FG(r) \cdot FH(r)$$

where

$$\text{(a)} \quad F\big(I(r)\big) = \frac{D^2}{2}\left[\cos^{-1}\frac{S\lambda f}{D} - \frac{S\lambda f}{D}\left(1 - (\frac{S\lambda f}{D})^2\right)^{\frac{1}{2}}\right]$$

when

$$S \leq \frac{D}{\lambda f}$$

$$F\big(I(r)\big) = 0 \quad \text{when } S > \frac{D}{\lambda f}$$

$$\text{(b)} \quad FG(r) = e^{-\pi 2\sigma^2 S^2}$$

$$\text{(c)} \quad FH(r) = (\frac{\ell}{2})^2 \frac{J_1(\pi \ell S)}{\frac{\ell S}{2}} \quad .$$

Multiplying and taking the inverse transform yields

$$L(r) = \frac{\pi D^2 \ell}{2} \int_0^\epsilon J_0(2\pi Sr) J_1(\pi \ell S) e^{-2\pi\sigma^2 S^2} \left[\cos^{-1} \frac{S}{\epsilon} - \frac{S}{\epsilon} \left(1 - \left(\frac{S}{\epsilon}\right)^2 \right)^{\frac{1}{2}} \right] dS$$

where

$$\epsilon = \frac{D}{\lambda f} .$$

We have evaluated this convolution for a series of possible ϵ parameters, in particular for an image dissector with a Gaussian width 2σ of 0.0035" and a collection aperture diameter ℓ of .020". This convolution data was then used to determine the peak-to-peak change in signal per micron of displacement and finally the item of utmost importance: the change in signal per arc second deviation of the sampled ray, and a signal-to-noise figure of merit.*

By plotting the S/N figure of merit versus focal length (Fig. 24) we see that we do have an optimum choice of focal length. However, the function is slowly varying over a large focal length range. The real optimization choice should be made considering the displacement stability of the coils, which can be relaxed at larger focal lengths, and residual mechanical vibration problems which become worse at larger focal lengths. A good compromise for this tube is a focal length of about 50".

---

*Signal current is defined as the peak-to-peak difference in the A.C. error signal generated by a ray displacement. Noise is determined by the total current generated by photons passing through the collection aperture ℓ.

TABLE III

HARTMANN TEST SENSITIVITY VALUES

ελ	D	f	% Signal Change per arc second	S/N
.01	.1"	10"	4.3	3.2
.005	.1"	20"	6.0	4.1
.002	.1"	50"	7.2	5.
.0015	.1"	66"	8.	5.2
.001	.1"	100"	10.	4.1
.0005	.1"	200"	11.	2.9
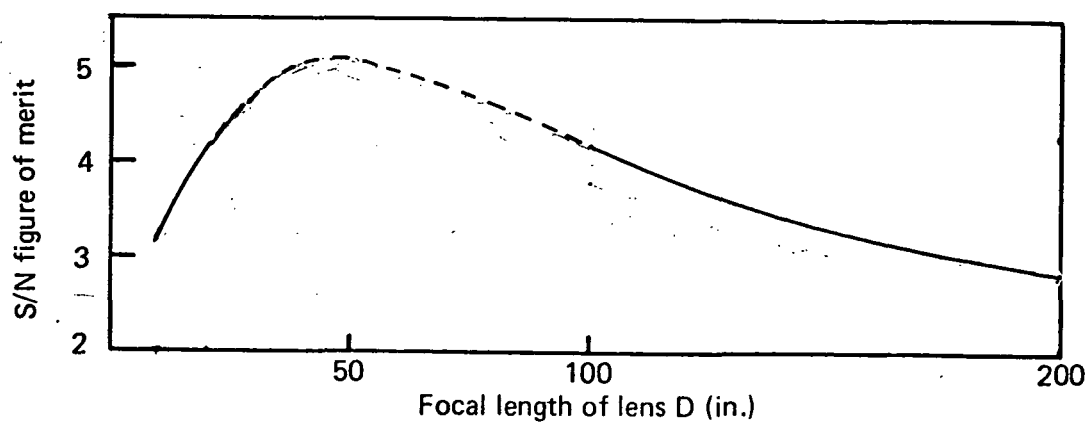
Fig. 24. S/N figure of merit as a function of focal length (image dissector tube).

iii. Signal-to-noise for image dissector readout.

Assuming we have optimized according to the above argument we can now calculate signal-to-noise ratios.

For an extended red photocathode the total signal at the cathode, for a zero magnitude A_o star assuming a 700 cm^2 sampling area collecting aperture, is $I = .50 \times 10^{-10}$ amps on the photocathode, which corresponds to the maximum photocathode current the tube can handle. Now assuming the parameter optimization as described in the last section:

$$\text{(Shot Noise)} \quad I_N \; = \; \sqrt{2e\Delta fI}$$

$$I_N \; = \; \sqrt{.5 \times 10^{-10}(2)(1.6 \times 10^{-19})(1)}$$

$$\approx \; 4 \times 10^{-15} \text{ amps.}$$

From above, for a 1 arc-sec detection, the signal is .06I.

$$I_s \; = \; 30 \times 10^{-13} \text{ amp}$$

$$\text{S/N} \; = \; \frac{30 \times 10^{-13}}{4 \times 10^{-15}} \; \approx \; 7.50 \times 10^2 \; \approx \; 750,$$

where dark current noise $\approx 10^{-16}$ amp for a .020" aperture.

We compute signal-to-noise for other star magnitudes and summarize the results in Table IV.

TABLE IV

BEST SIGNAL-TO-NOISE FOR DETECTING A 1 ARC-SEC SLOPE CHANGE

Magnitude	S/N	Detection Certainty
0	750	100%
2.5	250	100%
5	60	100%
7.5	6	100%

The above analysis has not considered noise problems associated with deflection coils and field effects in image tubes.

CHAPTER IV

FINE RANGE SENSORS

1. The Zernike Test.

    a. General discussion.

The usual interpretation of the Zernike test is based upon the spatial filtering concept. Consider a disturbance $e^{i\phi(x,y)}$ in the pupil of an optical system as in Fig. 25. If the aberrations are very small then we can represent $e^{i\phi(x,y)} = 1 + i\phi$. The important observation is that the aberration information and pupil information are 90° out of phase. If, in addition, the aberrations are of a high spatial frequency type, the Fourier transform of the pupil function consists of a zero order, due to the pupil aperture, and a separated higher order spectrum 90° out of phase and separated from the zero order. (See Fig. 26.) We then argue that a phase delay of 90° introduced by a phase filter on the zero order will bring the higher order information in phase with the zero order. Lens C then re-transforms the filtered spectrum with the aberration information and pupil effects in phase so that the intensity pattern in the pupil contains a modulation proportional to the phase error in the pupil for small aberrations. Furthermore, by attenuating the zero order, the modulation effects can be improved.
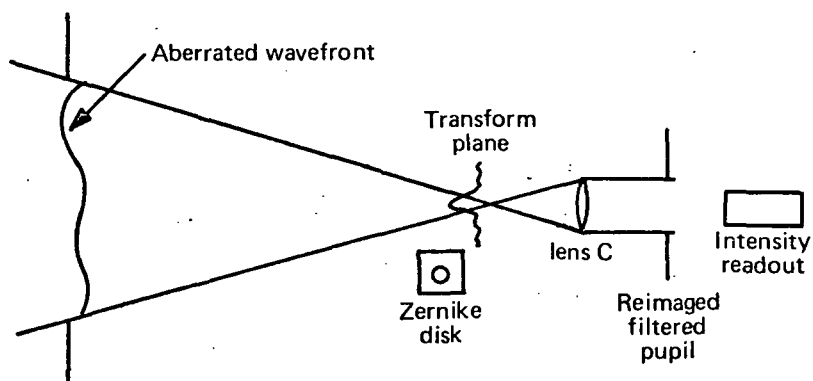
Fig. 25 Zernike phase contrast test arrangement.
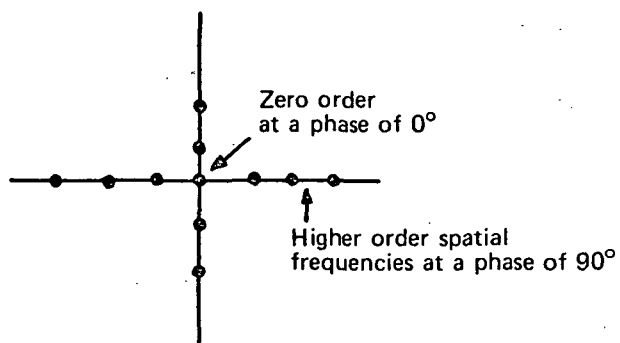
Fig. 26 . Spatial frequency distribution.

In the situation where we are looking for low order aberrations, such as may occur in figuring errors, thermal deformation errors, or misalignments, the problem is somewhat different. In this case the magnitudes of the aberrations are not so small that only a first-order expansion is permissible and, secondly, the aberration information is no longer separated out from the zero order diffraction pattern. These considerations lead to a slightly different interpretation of the problem as well as a more general formulation of the design of the Zernike disc itself, in terms of its size, the optimum phase shift, and the optimum attenuation. Zernike did some work on the low order problem in terms of a Zernike polynomial representation of the aberrations. However, he considered only the first-order term in the expansion and did not generalize the problem considering obscuration effects. He also assumed the $\pi/4$ phase shift and did not consider optimization of the disc parameters. What follows is a general development of the effects of a Zernike disc on the reimaged pupil. We show the relationship between disc size, phase shifts, and attenuations, and how these parameters affect signal-to-noise ratio, fringe visibility and the intensity in the reimaged pupil with and without various types of aberrations. We will also discuss the fabrication of the disc, effects of fabrication errors and tolerancing.

b. General development of intensity equation for reimaged pupil.

In Fig. 27 plane A represents the exit pupil, with fractional obscuration ε of an optical system with radius a and focal length f. The exit pupil contains a general wavefront represented by $e^{i\phi(\rho,\theta)}$. The
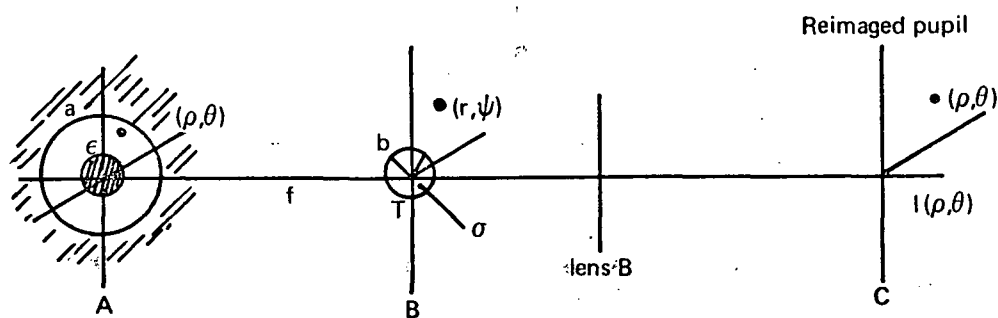
Fig. 27. Pupil geometry for Zernike equation derivations.

normalized coordinate ρ ranges from ε to 1. The pupil amplitude is then represented by:

$$P_o = e^{i\phi}\Pi(\tfrac{\rho}{2})\left[1 - \Pi(\tfrac{\rho}{2\varepsilon})\right],$$

where

$$\Pi(\tfrac{\rho}{2x}) = 1 \qquad \tfrac{\rho}{x} \leq 1$$

$$= 0 \qquad \tfrac{\rho}{x} > 1.$$

At plane B, the Fraunhofer plane, the amplitude of the diffraction pattern $\tilde{P}$ is:

$$\tilde{P} = K_1\tilde{P}_0,$$

where

$$\tilde{P}_0 = K_1 \int_0^1 \int_0^{2\pi} e^{i\phi}\, e^{-i[v\rho\cos(\theta-\psi)]}\rho\,d\rho\,d\theta$$

$$K_1 = -\frac{ia^2}{\lambda f} \qquad v = \frac{2\pi}{\lambda}\frac{a}{f}r$$

and r, ψ are coordinates in plane B.

In plane B we place a circular mask of radius b, which produces a phase shift σ within b and contains an amplitude attenuation (or relative amplification factor) T outside b. Thus, after passing through the mask $\tilde{P}$, the amplitude diffraction pattern becomes:

$$\tilde{P}' = K_1 T \tilde{P}_0 \left[1 - \Pi(\frac{r}{2b}) \right] + e^{i\sigma} K_1 \tilde{P}_0 \Pi(\frac{r}{2b}).$$

By rearranging we obtain:

$$\tilde{P}' = K_1 T \tilde{P}_0 + (e^{i\sigma} - T) K_1 \tilde{P}_0 \Pi(\frac{r}{2b}).$$

This amplitude field then passes through lens B and at plane C (the conjugate plane to A) the amplitude of the disturbance $P_0{}^i$ is:

$$P_0{}^i = K_2 \tilde{\tilde{P}}'$$

where

$$\tilde{\tilde{P}}' = \int_0^\infty \int_0^{2\pi} \tilde{P}' e^{-iwr \cos(\psi - \theta')} r dr d\psi$$

$$w = \frac{2\pi a \cdot \rho}{\lambda f} \qquad K_2 = \frac{i}{\lambda f} \qquad q = \frac{2\pi a}{\lambda f}$$

We are assuming lens B has an aperture sufficiently large to accept all scattered rays. Integrating we obtain:

$$P_0{}^i = \frac{4\pi^2 K_1 K_2}{q^2} T e^{-i\phi} \Pi(\frac{\rho}{2}) \left[1 - \Pi(\frac{\rho}{2\epsilon}) \right] + (e^{i\sigma} - T) K_1 K_2 \left[\widetilde{\tilde{P}_0 \Pi(\frac{r}{2b})} \right]$$

where

$$\left[\widetilde{\tilde{P}_0 \Pi(\frac{r}{2b})} \right] = \int_0^b \int_0^{2\pi} \tilde{P}_0 e^{-iwr \cos(\psi - \theta')} r dr d\psi$$

is in general a complex function $X(\rho,\psi)$

$$= X(\rho,\psi) = Q(\rho)e^{i\psi}$$

$$Q(\rho,\psi) = \sqrt{\text{Re } X^2 + \text{Im } X^2}$$

$$\psi(\rho,\psi) = \text{Arctan } \frac{\text{Im } X(\rho,\psi)}{\text{Re } X(\rho,\psi)} .$$

Thus:

$$P_0^{\ i} = T P_0^{\ *} + \frac{a^2}{\lambda^2 f^2} (e^{i\sigma} - T) \cdot X(\rho).$$

We now let $(e^{i\sigma} - T) = Ae^{i\gamma}$, thus,

$$A^2 = 1 + T^2 - 2T \cos\sigma$$

$$\tan\gamma = \frac{\sin\sigma}{\cos\sigma - T} .$$

Substituting we obtain

$$P_0^{\ i} = T P_0^{\ *} + \frac{a^2}{\lambda^2 f^2} A Q(\rho)e^{i(\psi+\gamma)} .$$

What we have here is an expression for a two-beam interferometer where $TP_0^{\ *}$ is the test beam containing the pupil aberration information and the second term represents a reference wave whose amplitude $\frac{a^2 A Q(\rho)}{\lambda^2 f^2}$ and phase γ is determined by the Zernike disc properties. The factor ψ as will be seen represents the effects of the aberrations on the reference wave. As it turns out, ψ is practically constant so that its effect is essentially one of shifting the intensity-gram by a constant. We will come back to the evaluation of $X(\rho)$ in the next section.

Multiplying $P_0{}^i$ by its complex conjugate yields the intensity of the reimaged pupil for a unit amplitude pupil function.

$$I(\rho,\theta) = P_0{}^i \times P_0{}^{i*} = T^2 + \frac{1Q^2A^2}{16\lambda^4F\#^4} - \frac{2TQA}{4\lambda^2F\#^2} \sin(\xi+\psi-\phi)$$

(holds for $\epsilon \leq \rho \leq 1$)

where

$$\xi = \gamma - \pi/2$$

$$I(\rho,\theta) = \frac{A^2Q^2(\rho,\theta)}{16\lambda^4F\#^4} \qquad \epsilon > \rho > 1$$

Our development here gives us an added bonus in the intensity prediction outside the pupil. We will see later how we can possibly use this information in order to determine the zero aberration profile for an imperfectly manufactured Zernike disc. The question now is: how to choose the values of T and σ to optimize the Zernike test performance?

If we desire to operate on the midpoint of a fringe so we have maximum range ($\sim\pm$ quarter-wave) we want to choose $\xi = 0$. If this is the case we then have $\gamma = \xi + \pi/2 = \pi/2$. Then from $\tan\gamma = \frac{\sin\sigma}{\cos\sigma-T}$, we have the constraining condition that $T = \cos\sigma$, and thus $A = 1-T^2 = \sin^2\sigma$. Now we have to consider fringe visibility. The visibility

$$V = \left(\frac{2QAT}{4\lambda^2F\#^2}\right) \div \left(T^2 + \frac{Q^2A^2}{16\lambda^4F\#^4}\right) = \left(\frac{2Q\sin2\sigma}{4\lambda^2F\#^2}\right)$$

$$\div \left(1 + \frac{Q^2}{16\lambda^4F\#^4} + \left(1 - \frac{Q^2}{16\lambda^4F\#^4}\right)\cos2\sigma\right).$$

By differentiating and setting equal to zero, we obtain the condition for maximum visibility:

$$\cos 2\sigma = -\frac{1 - \frac{Q^2}{16\lambda^4 F^4}}{1 + \frac{Q^2}{16\lambda^4 F^4}} .$$

Thus, by picking σ to satisfy this equation and the transmission to satisfy the equation $T^2 = \cos^2\sigma$, we guarantee a fringe visibility of unity and an operating point that gives us maximum range. We see that the choice of σ depends upon $\frac{Q(\rho)}{16\lambda^4 F^4}$, which depends upon wavelength, system F number, and the size of the Zernike disc. As we will demonstrate later, the effect of a large Zernike disc is to yield a reimaged pupil that has large intensity graduations for a zero-aberration condition. A large Zernike disc also tends to mix aberration information into the reference wave. Smaller discs tend to yield a uniform zero-aberration pupil profile with little aberration mixing in the reference wave. However the transmission factor is small and more energy is wasted. In Table V we have calculated the optimum phase shift and transmission required for several Zernike disc radii, corresponding to about 1/10 to 1/2 the size of the diffraction pattern of an f/12 system operating at a wavelength of 0.6 μm, making use of expressions for Q derived in the following sections. Considering signal-to-noise requirements, pupil profile, and aberration mixing, the disc corresponding to about 1/3 the size of the central diffraction lobe appears to be a good compromise.

TABLE V

ZERNIKE DISC DESIGN PARAMETERS AT 0.6 μm

Disc Size	Phase Delay σ	T^2
2μ	.228λ	2%
3μ	.206λ	7%
4μ	.189λ	13.8%
5μ	.178λ	18.8%

c. Derivation of the effects of the Zernike disc on the reimaged pupil.

The effect of the Zernike disc on the reimaged pupil manifests itself through the term $X(\rho,\theta) = Q(\rho,\theta)e^{i\psi(\rho,\theta)}$. One can evaluate the integral

$$X(\rho,\theta) = \int_0^b \int_0^{2\pi} U(r,\psi)e^{-iwr\,\cos(\psi-\theta)}rdrd\psi,$$

where $U(r,\psi)$ is the amplitude diffraction pattern, numerically using a good deal of computer time. We have however, taken the approach of developing analytical expressions for both $U(r,\psi)$ and $X(\rho,\theta)$. The work has provided accurate analytical expressions for $U(r,\psi)$ for aberrations of up to .22λ and accurate analytical expressions for $X(\rho,\theta)$ for Zernike disc sizes up to 2/5 of an Airy disc size. The range of accuracy could

be improved by expanding the expressions developed to include higher orders. The derivations have included the effects introduced by a system obscuration.

First we develop analytical expressions for the diffraction pattern amplitude $U(r,\psi)$, which includes aberration effects and the effect of a circular obscuration. The derivations that follow are done in terms of special functions $\Lambda_N(v)$ called Lambda functions. The Lambda function is defined such that:

$$\Lambda_N(v) = 2^N N! \frac{J_N(v)}{v^N}$$

where $J_N(v)$ is an Nth order Bessel function. Using the recursion formula for Bessel's function one can show that:

$$\Lambda_N(v) = \Lambda_{N-1}(v) + \frac{v^2}{4N(N+1)} \Lambda_{N+1}(v)$$

$$\Lambda(\tfrac{\rho}{2})(1-\rho^2)^N \rho^M \cos^M \theta \leftrightarrow (-i)^M \frac{\Pi}{N+1} \left[\frac{1}{(2\Pi)^M} \frac{\partial^M}{\partial Y^M} \Lambda_{N+1}(v) \right] \qquad (A)$$

where $\leftrightarrow$ represents a two-dimensional Fourier transform, and

$$v = 2\pi r_1$$

$$r_1 = \sqrt{X^2 + Y^2}$$

$$X = \frac{X_o a}{\lambda f}$$

$$Y = \frac{Y_o a}{\lambda f}$$

We can also show that:

$$\frac{d\Lambda_N(v)}{dv} = -\frac{1}{2} v \frac{\Lambda_{N+1}(v)}{N+1}$$

$$\frac{d^2\Lambda_N(v)}{dv^2} = \frac{2N+1}{2N+2} \Lambda_{N+1}(v) - \Lambda_N(v)$$

$$\frac{d^2\Lambda_N(v)}{dv^2} = -\frac{1}{2} v \frac{1}{4}\left[\Lambda_{N+2}(v) - \frac{\Lambda_{N+1}(v)}{N+1}\right]$$

$$\frac{\partial}{\partial Y} \Lambda_{N+1}(v) = 2\pi\cos\psi\left[-\frac{1}{2} v \frac{\Lambda_{N+2}(v)}{N+2}\right]$$

$$\frac{\partial^2}{\partial Y^2} \Lambda_{N+1}(v) = -\frac{(2\pi)^2}{4} (1-\cos2\psi) \frac{\Lambda_{N+2}(v)}{N+2}$$

$$+ \frac{(2\pi)^2}{2} (1+\cos2\psi)\left[\frac{2N+3}{2N+4} \Lambda_{N+2}(v) - \Lambda_{N+1}(v)\right].$$

(B)

The approach is now as follows. The pupil function $e^{i\phi}$ is expanded to the second term $= 1 + i\phi - \frac{1}{2} \phi^2$, where

$$\phi = W_{11}\rho\cos\phi + W_{02}\rho^2 + W_{04}\rho^4 + W_{06}\rho^6 + W_{13}\rho^3\cos\phi$$

$$+ W_{22}\rho^2\cos^2\phi.$$

This is a power series representation of the phase in the pupil where W_{11} is a tilt effect, W_{02} is a defocus effect, W_{04} and W_{06} are spherical aberration effects, W_{13} is a coma effect, and W_{22} is an astigmatism effect. This expansion is substituted into:

$$U(r,\psi) = K_1 \int_{\epsilon}^{1} \int_{0}^{2\pi} e^{i\phi} e^{-i[v\rho\cos(\theta-\psi)]} \rho \, d\rho \, d\theta$$

where

$$e^{i\phi} = 1 + i\phi - \phi^2/2.$$

After substitution we arrive at a series of transforms of terms of the form $\rho^{2N+M}\cos^M\theta$, where N and M take on various positive values. We can show that

$$\rho^{2N+M}\cos^M\theta = \left[1 - N(1-\rho^2) + \frac{N(N-1)}{2!}(1-\rho^2)^2 \right.$$

$$\left. - \frac{N(N-1)(N-2)(1-\rho^2)^3}{3!} + \ldots\right] \cdot \cos^M\theta\,\rho^M.$$

By taking each term in the power expansion and putting it in to the above form, applying the Fourier transform relationship (A) and finally making use of the derivative relationships (B) we arrive at the following expression for diffraction amplitude in plane B.

$$U = U_0 + U_{11} + U_{02} + U_{04} + U_{13} + U_{22} + U_{\text{Interactions}}$$

where $U_{\text{Interactions}}$ represent cross terms resulting from the ϕ^2 term in the pupil function where:

$$U_0 = \Pi[\Lambda_1(v) - \epsilon^2\Lambda_1(\epsilon v)] \qquad \begin{array}{l}\text{--diffraction pattern of the}\\\text{obstructed aperture.}\end{array}$$

$$K = \frac{2\pi}{\lambda}$$

Defocus:

$$U_{02} = \Pi(iKW_{02})\left[\Lambda_1(v) - \frac{1}{2}\Lambda_2(v) - \epsilon^4\left(\Lambda_1(\epsilon v) - \frac{1}{2}\Lambda_2(\epsilon v)\right)\right]$$

$$- \frac{\Pi K^2 W_{02}^2}{2}\left[\Lambda_1(v) - \Lambda_2(v) + \frac{1}{3}\Lambda_3(v)\right.$$

$$\left. - \epsilon^4\left(\Lambda_1(\epsilon v) - \Lambda_2(\epsilon v) + \frac{1}{3}\Lambda_3(\epsilon v)\right)\right]$$

Third-order spherical:

$$U_{04} = \Pi(iKW_{04})\left[\Lambda_1(v) - \Lambda_2(v) + \frac{1}{3}\Lambda_3(v)\right.$$

$$\left. - \epsilon^6\left(\Lambda_1(\epsilon v) - \Lambda_2(\epsilon v) + \frac{1}{3}\Lambda_3(\epsilon v)\right)\right]$$

$$- \frac{\Pi}{2}K^2 W_{04}^2\left[\Lambda_1(v) - 2\Lambda_2(v) + \frac{5}{3}\Lambda_3(v) - \Lambda_4(v)\right.$$

$$+ \frac{1}{5}\Lambda_5(v) - \epsilon^{10}\left(\Lambda_1(\epsilon v) - 2\Lambda_2(\epsilon v)\right.$$

$$+ \frac{5}{3}\Lambda_3(\epsilon v) - \Lambda_4(\epsilon v)$$

$$\left.\left. + \frac{1}{5}\Lambda_5(\epsilon v)\right)\right]$$

Tilt:

$$U_{11} = \Pi(iKW_{11})(iv\cos\psi)\left[\frac{1}{4}\Lambda_2(v) - \frac{1}{4}\epsilon^4\Lambda_2(\epsilon v)\right]$$

$$-\frac{\Pi}{2}K^2W_{11}^2\left[\frac{1}{2}\left(\Lambda_1(v) - \frac{1}{2}\Lambda_2(v)\right)\right.$$

$$+\frac{1}{2}\left(\Lambda_1(v) - \Lambda_2(v)\right)\cos2\psi$$

$$\left.-\epsilon^4\left[\frac{1}{2}\left(\Lambda_1(\epsilon v) - \frac{1}{2}\Lambda_2(\epsilon v)\right) + \frac{1}{2}\left(\Lambda_1(\epsilon v) - \Lambda_2(\epsilon v)\right)\cos2\psi\right]\right]$$

Astigmatism:

$$U_{22} = \Pi(iKW_{22})\left[\frac{1}{2}\left[\Lambda_1(v) - \frac{1}{2}\Lambda_2(v)\right] + \frac{1}{2}\left[\Lambda_1(v) - \Lambda_2(v)\right]\cos2\psi\right.$$

$$\left.-\epsilon^4\left(\frac{1}{2}\left[\Lambda_1(\epsilon v) - \frac{1}{2}\Lambda_2(\epsilon v)\right] + \frac{1}{2}\left[\Lambda_1(\epsilon v) - \Lambda_2(\epsilon v)\right]\cos2\psi\right)\right]$$

$$-\frac{\Pi}{16}K^2W_{22}^2\left[\Lambda_3(v) - 3\Lambda_2(v) + 3\Lambda_1(v) + \cos2\psi\cdot\right.$$

$$\left[2\Lambda_3(v) - 6\Lambda_2(v) + 4\Lambda_1(v)\right]$$

$$+\cos4\psi\left[2\Lambda_3(v) - 3\Lambda_2(v) + \Lambda_1(v)\right]$$

$$-\epsilon^6\left\{\Lambda_3(\epsilon v) - 3\Lambda_2(\epsilon v) + 3\Lambda_1(\epsilon v) + \cos2\psi\cdot\right.$$

$$\left[2\Lambda_3(\varepsilon v) - 6\Lambda_2(\varepsilon v) + 4\Lambda_1(\varepsilon v)\right]$$

$$+ \cos4\psi\left[2\Lambda_3(\varepsilon v) - 3\Lambda_2(\varepsilon v) + \Lambda_1(\varepsilon v)\right]\Bigg\}\Bigg]$$

Coma:

$$U_{13} = \Pi(iKW_{31})(iv\,\cos\psi)\left[\frac{1}{4}\Lambda_2(v) - \frac{1}{12}\Lambda_3(v)\right.$$

$$- \varepsilon^6\left(\frac{1}{4}\Lambda_2(\varepsilon v) - \frac{1}{12}\Lambda_3(\varepsilon v)\right)$$

$$- \frac{K^2\Pi}{4}W_{13}^2\left[\Lambda_1(v) - \frac{3}{2}\Lambda_2(v) + \Lambda_3(v) - \frac{\Lambda_4(v)}{4}\right.$$

$$+ \cos2\psi\left[\Lambda_1(v) - 2\Lambda_2(v) + \frac{4}{3}\Lambda_3(v)\right]$$

$$- \varepsilon^8\left(\left(\Lambda_1(\varepsilon v) - \frac{3}{2}\Lambda_2(\varepsilon v) + \Lambda_3(\varepsilon v) - \frac{\Lambda_4(\varepsilon v)}{4}\right)\right.$$

$$\left.\left.\left.+ \cos2\psi\left(\Lambda_1(\varepsilon v) - 2\Lambda_2(\varepsilon v) + \frac{4}{3}\Lambda_3(\varepsilon v)\right)\right)\right)\right]$$

$$U_{\text{INTERACTION}} = -\Pi K^2 W_{02} W_{04}\left[\Lambda_1(v) - \frac{3}{2}\Lambda_2(v) + \Lambda_3(v) - \frac{1}{4}\Lambda_4(v)\right.$$

$$\left. - \epsilon^8\left(\Lambda_1(\epsilon v) - \frac{3}{2}\Lambda_2(\epsilon v) + \Lambda_3(\epsilon v) - \frac{1}{4}\Lambda_4(\epsilon v)\right)\right]$$

$$- \Pi K^2 W_{11} W_{02}(iv\cos\psi)\left[\frac{1}{4}\Lambda_2(v) - \frac{1}{12}\Lambda_3(v)\right.$$

$$\left. - \epsilon^6\left(\frac{1}{4}\Lambda_2(\epsilon v) - \frac{1}{12}\Lambda_3(\epsilon v)\right)\right]$$

$$- \frac{\Pi k^2}{2}(W_{13}W_{11} + W_{02}W_{22})\left[\Lambda_1(v) - \Lambda_2(v) + \frac{\Lambda_3(v)}{3}\right.$$

$$+ \cos2\psi\left[\Lambda_1(v) - \frac{3}{2}\Lambda_2(v) + \frac{\Lambda_3(v)}{2}\right]$$

$$- \epsilon^6\left(\Lambda_1(\epsilon v) - \Lambda_2(\epsilon v) + \frac{\Lambda_3(\epsilon v)}{3}\right)$$

$$\left. + \cos2\psi\left(\Lambda_1(\epsilon v) - \frac{3}{2}\Lambda_2(\epsilon v) + \frac{\Lambda_3(\epsilon v)}{2}\right)\right]$$

$$- iK^2\Pi v\cos\psi(W_{11}W_{04} + W_{02}W_{13})\left[\frac{\Lambda_2(v)}{4} - \frac{\Lambda_3(v)}{6} + \frac{\Lambda_4(v)}{24}\right.$$

$$\left. - \epsilon^8\left(\frac{\Lambda_2(\epsilon v)}{4} - \frac{\Lambda_3(\epsilon v)}{6} + \frac{\Lambda_4(\epsilon v)}{24}\right)\right]$$

$$- iK^2 W_{04} W_{13} \Pi v \, \cos\psi \left[\frac{\Lambda_2(v)}{4} - \frac{\Lambda_3(v)}{4} + \frac{\Lambda_4(v)}{8} - \frac{\Lambda_5(v)}{40} \right.$$

$$\left. - \epsilon^{10} \left(\frac{\Lambda_2(\epsilon v)}{4} - \frac{\Lambda_3(\epsilon v)}{4} + \frac{\Lambda_4(\epsilon v)}{8} - \frac{\Lambda_5(\epsilon v)}{40} \right) \right]$$

$$- \frac{iK^2 \Pi W_{11} W_{22}}{16} \left[\left(\left(-v\Lambda_3(v) + 3v\Lambda_2(v) \right) \cos\psi + \left(v\Lambda_2(v) - v\Lambda_3(v) \right) \cos 3\psi \right. \right.$$

$$\left. \left. - \epsilon^6 \left((-v\Lambda_3(\epsilon v) + 3v\Lambda_2(\epsilon v)) \cos\psi + \left(v\Lambda_2(\epsilon v) - v\Lambda_3(\epsilon v) \right) \cos 3\psi \right) \right) \right]$$

$$- \frac{iK^2 \Pi W_{13} W_{22}}{16} \left[\left(3\Lambda_2(v) - 2\Lambda_3(v) \right) + \frac{1}{2} \Lambda_4(v) \, v \, \cos\psi + \left(\Lambda_2(v) - \frac{4}{3} \Lambda_3(v) \right. \right.$$

$$\left. + \frac{1}{3} \Lambda_4(v) \right) v \, \cos 3\psi$$

$$- \epsilon^8 \left[\left(3\Lambda_2(\epsilon v) - 2\Lambda_3(\epsilon v) + \frac{1}{2} \Lambda_4(\epsilon v) \right) v \, \cos\psi \right.$$

$$\left. \left. + \left(\Lambda_2(\epsilon v) - \frac{4}{3} \Lambda_3(\epsilon v) + \frac{1}{3} \Lambda_4(\epsilon v) \right) v \, \cos 3\psi \right] \right]$$

The above expression enables us to determine the diffraction pattern amplitude in the presence of third-order aberrations less than quarter-wave in magnitude, where the effect of a circular obscuration has been included.

We now want to determine the analytical expression that describes the effect of the Zernike disc on the reimaged pupil. We do this by substituting the previous derived expression for $U(r,\psi)$ into the integral expression for $X(\rho,\theta)$. We then make use of the fact that the Λ functions can be expanded in a power series where

$$\Lambda_{N-1}(\varepsilon v) = 1 - \frac{\varepsilon^2 v^2}{4N} + \frac{\varepsilon^4 v^4}{16N^2(\frac{2}{N} + 2)} + \ldots$$

We apply the three terms of the expansion to the unaberrated pupil U_o, and the quadratic approximation to the aberration terms. We also make use of the recursion relationship for Bessel functions:

$$J_{N-1}(v) + J_{N+1}(v) = \frac{2N\,J_N(v)}{v},$$

and the integral relationships:

$$\int_0^{2\pi} \cos M\theta\, e^{-iv\rho\cos(\theta-\psi)}\,d\theta = (-i)^M 2\pi\,J_M(v\rho)\cos M\psi,$$

and

$$\int_0^1 \rho^{v+1}\,J_v(v\rho)\,d\rho = \frac{1}{v}\,J_{v+1}(v).$$

After a good deal of tedious manipulation and evaluation we obtain:

$$X(\rho,\theta) = X_o(\rho,\theta) + X_{Ab}(\rho,\theta),$$

where $X_0(\rho,\theta)$ is the effect of Zernike disc on the unaberrated pupil and $X_{Ab}(\rho,\theta)$ is the effect rendered on the aberrated wavefront.

$$X_0(\rho,\theta) = 2\pi^2 b^2 \left[\frac{J_1(wb)}{wb} - \frac{b^2 q^2}{8}\left(\frac{2}{w^2 b^2} J_2(wb) - \frac{J_3(wb)}{wb} \right) \right]$$

$$- 2\pi^2 \varepsilon^2 b^2 \left[\frac{J_1(wb)}{wb} - \frac{b^2 \varepsilon^2 q^2}{8}\left(\frac{2}{w^2 b^2} J_2(wb) - \frac{J_3(wb)}{wb} \right) \right]$$

$$+ \frac{2\pi^2 b^6 q^4}{192}\left[1-\varepsilon^6\right]\left[\frac{J_1(wb)}{wb} - \frac{4J_2(wb)}{w^2 b^2} + \frac{8J_3(wb)}{w^3 b^3} \right]$$

$$X_{Aberration}(\rho,\theta) = iKW_{02}\left[\frac{J_1(wb)}{2wb} - \frac{b^2 q^2}{12}\left(\frac{2}{w^2 b^2} J_2(wb) - \frac{J_3(wb)}{wb} \right) \right]$$

$$- i2\pi^2 b^2 KW_{02}\varepsilon^4 \left[\frac{J_1(wb)}{2wb} - \frac{b^2 \varepsilon^2 q^2}{12}\left(\frac{2J_2(wb)}{w^2 b^2} - \frac{J_3(wb)}{wb} \right) \right]$$

$$- b^2 \pi^2 K^2 W_{02}{}^2 \left[\frac{J_1(wb)}{3wb} - \frac{b^2 q^2}{16}\left(\frac{2}{w^2 b^2} J_2(wb) - \frac{J_3(wb)}{wb} \right) \right]$$

$$+ b^2 \pi^2 K^2 \varepsilon^6 W_{02}{}^2 \left[\frac{J_1(wb)}{3wb} - \frac{b^2 q^2 \varepsilon^2}{16}\left(\frac{2}{w^2 b^2} J_2(wb) - \frac{J_3(wb)}{wb} \right) \right]$$

$$+ iKW_{04}\left[\frac{J_1(wb)}{3wb} - \frac{b^2 q^2}{16}\left(\frac{2}{w^2 b^2} J_2(wb) - \frac{J_3(wb)}{wb} \right) \right]$$

$$- i2\pi^2 b^2 K W_{04} \epsilon^6 \left[\frac{J_1(wb)}{3wb} - \frac{b^2\epsilon^2 q^2}{12} \left(\frac{2J_2(wb)}{w^2 b^2} - \frac{J_3(wb)}{wb} \right) \right]$$

$$- b^2 \pi^2 K^2 W_{04}{}^2 \left[\frac{J_1(wb)}{5wb} - \frac{b^2 q^2}{24} \left(\frac{2}{w^2 b^2} J_2(wb) - \frac{J_3(wb)}{wb} \right) \right]$$

$$+ b^2 \pi^2 K^2 W_{04}{}^2 \epsilon^{10} \left[\frac{J_1(wb)}{5wb} - \frac{b^2 q^2 \epsilon^2}{24} \left(\frac{2J_2(wb)}{w^2 b^2} - \frac{J_3(wb)}{wb} \right) \right]$$

$$+ iq2\pi^2 K W_{11} \cos\theta \left[\frac{J_2(wb)}{4wb} b^3 + \frac{q^2 b^5}{48} \left(\frac{2}{w^2 b^2} J_3(wb) - \frac{J_2(wb)}{wb} \right) \right]$$

$$- iq2\pi^2 K \cos\theta W_{11} \epsilon^4 \left[\frac{J_2(wb)}{4wb} b^3 + \frac{q^2 \epsilon^2 b^5}{48} \left(\frac{2}{w^2 b^2} J_3(wb) - \frac{J_2(wb)}{wb} \right) \right]$$

$$- b^2 \frac{\pi^2}{2} K^2 W_{11}{}^2 \left[\frac{J_1(wb)}{2wb} - \frac{b^2 q^2}{12} \left(\frac{2}{w^2 b^2} J_2(wb) - \frac{J_3(wb)}{wb} \right) + \cos 2\theta \frac{b^2 q^2}{24wb} J_3(wb) \right.$$

$$\left. - \epsilon^4 \left(\frac{J_1(wb)}{2wb} - \frac{b^2 \epsilon^2 q^2}{12} \left(\frac{2}{w^2 b^2} J_2(wb) - \frac{J_3(wb)}{wb} \right) \right. \right.$$

$$\left. \left. + \cos 2\theta \frac{b^2 \epsilon^2 q^2}{24wb} J_3(wb) \right) \right]$$

$$+ iq2\pi^2 KW_{13}\cos\theta\left[\frac{J_2(wb)}{6wb}b^3 + \frac{q^2b^5}{64}\left(\frac{2}{w^2b^2}J_3(wb) - \frac{J_2(wb)}{wb}\right)\right]$$

$$- iq2\pi^2 KW_{13}\cos\theta\varepsilon^6\left[\frac{J_2(wb)}{6wb}b^3 + \frac{q^2\varepsilon^2b^5}{64}\left(\frac{2}{w^2b^2}J_3(wb) - \frac{J_2(wb)}{wb}\right)\right]$$

$$- \frac{K^2\pi^2W_{13}^2b^2}{2}\left[\frac{J_1(wb)}{4wb} - \frac{b^2q^2}{20}\left[\frac{2}{w^2b^2}J_2(wb) - \frac{J_3(wb)}{wb}\right] + \cos2\theta\frac{b^2q^2J_3(wb)}{40wb}\right.$$

$$\left. - \varepsilon^8\left(\frac{J_1(wb)}{4wb} - \frac{b^2q^2\varepsilon^2}{20}\left(\frac{2}{w^2b^2}J_2(wb) - \frac{J_3(wb)}{wb}\right) + \cos2\theta\left(\frac{b^2\varepsilon^2q^2}{40wb}J_3(wb)\right)\right)\right]$$

$$+ i\pi^2 KW_{22}\left[\left(\frac{b^2J_1(wb)}{2wb} - \frac{b^4q^2}{12}\left(\frac{2}{w^2b^2}J_2(wb) - \frac{J_3(wb)}{wb}\right) + \cos2\theta\frac{b^4q^2}{24wb}J_3(wb)\right)\right.$$

$$\left. - \varepsilon^4\left(\frac{b^2J_1(wb)}{2wb} - \frac{b^4q^2\varepsilon^2}{12}\left(\frac{2}{w^2b^2}J_2(wb) - \frac{J_3(wb)}{wb}\right) + \cos2\theta\frac{b^4q^2\varepsilon^2J_3(wb)}{24wb}\right)\right]$$

$$
-\frac{3}{8} K^2 \pi^2 W_{22}^2 \left[\left(\frac{b^2 J_1(wb)}{3wb} - \frac{b^4 q^2}{16} \left(\frac{2}{w^2 b^2} J_2(wb) - \frac{J_3(wb)}{wb} \right) \right) + \cos 2\theta \frac{b^4 q^2}{24wb} J_3(wb) \right.
$$

$$
- \cos 4\theta \frac{q^2 b^4}{2} \left(\frac{J_2(wb)}{w^2 b^2} + \frac{J_3(wb)}{6wb} - \frac{8}{w^4 b^4} \left(1 - J_0(wb) \right) + \frac{4}{w^3 b^3} J_1(wb) \right) \right]
$$

$$
- \epsilon^6 \left[\frac{b^2 J_1(wb)}{3wb} - \frac{b^4 q^2 \epsilon^2}{16} \left[\frac{2}{w^2 b^2} J_2(wb) - \frac{J_2(wb)}{wb} \right] + \cos 2\theta \frac{b^4 q^2 \epsilon^2}{24wb} J_3(wb) \right.
$$

$$
- \cos 4\theta \frac{q^2 b^4 \epsilon^2}{2} \left(\frac{J_2(wb)}{w^2 b^2} + \frac{J_3(wb)}{6wb} - \frac{8}{w^4 b^4} \left(1 - J_0(wb) \right) + \frac{4}{w^3 b^3} J_1(wb) \right) \right]
$$

plus cross terms.

This equation has been programmed and the data run to obtain $X(\rho, \theta)$ for cases that show the effect of the Zernike disc radius on $X(\rho)$. As stated before, this information was used to calculate σ and T and is tabulated in Table V. These data were then used to obtain the no-aberration profiles for the reimaged pupil which appear in Fig. 28. These vividly demonstrate the tradeoff between disc size and pupil uniformity. For an f#12 system operating at an effective wavelength of 0.6 μm, a 3 to 4 μm Zernike radius appears to be a reasonable compromise.
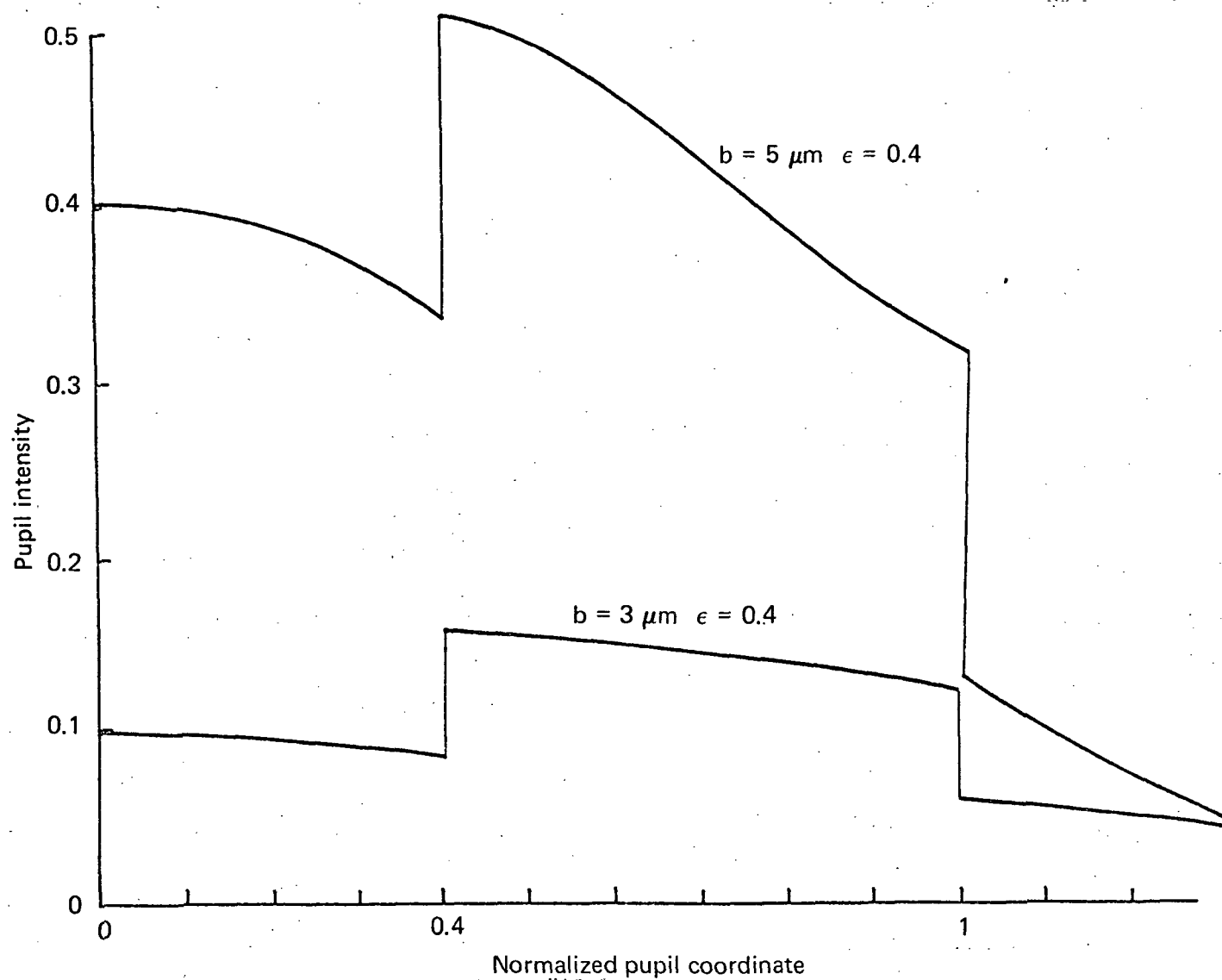
Fig. 28. Reimaged pupil through Zernike disk (no aberration).

Fig. 29. Reimaged pupil under the following conditions: $\lambda = 0.60\ \mu m$, F/no. = 12.000, b = 3.000, $\epsilon = 0.4000$, $W_{02} = 0 1$, $\sigma = 1.3025$ rad., T = 0.2605

Fig. 30. Reimaged pupil under the following conditions: $\lambda = 0.60\ \mu m$,
F/no. = 12.000, b = 3.000, ϵ = 0.4000, W_{02} = 0.050, σ = 1.3025
rad., T = 0.2605

Fig. 31. Reimaged pupil under the following conditions: $\lambda = 0.60\,\mu m$, F/no. = 12.000, b = 3.000, ϵ = 0.4000, W_1 = 0.0, W_{02} = 0.100, σ = 1.3025 rad., T = 0.2605

Fig. 32. Reimaged pupil under the following conditions: $\lambda = 0.60 \ \mu m$, F/no. = 12.000, b = 3.000, ϵ = 0.4000, W_{02} = 0.200, σ = 1.3025 rad., T = 0.2605
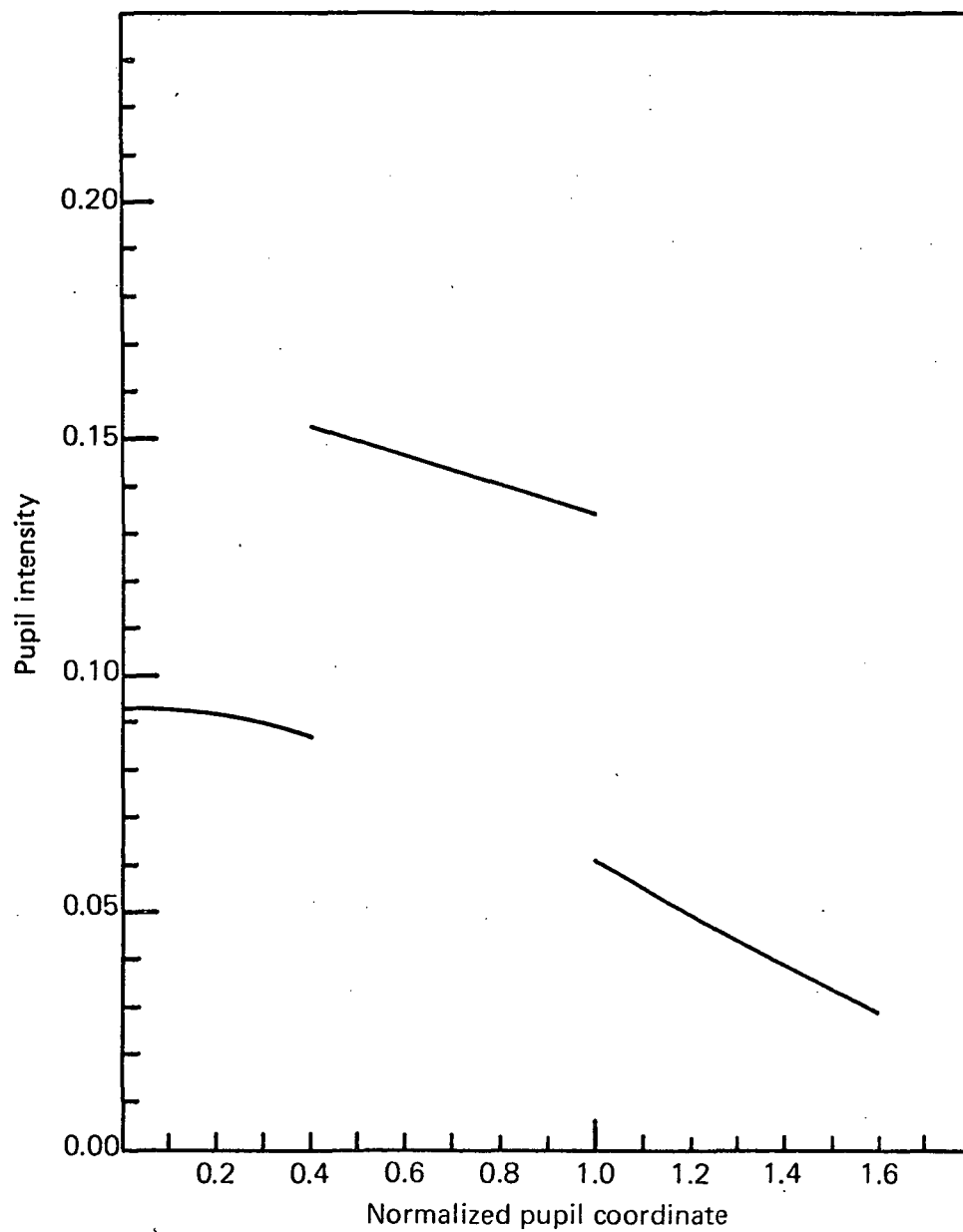
Fig. 33. Reimaged pupil under the following conditions: λ = 0.60 μm,
F/no. = 12.000, b = 3.000, ϵ = 0.4000, ω_{04} = 0.010, σ = 1.3025
rad., T = 0.2605

Fig. 34. Reimaged pupil under the following conditions: $\lambda = 0.60 \ \mu m$,
F/no. = 12.000, b = 3.000, ϵ = 0.4000, W_{04} = 0.050, σ = 1.3025
rad., T = 0.2605

Fig. 35. Reimaged pupil under the following conditions: λ = 0.60 μm, F/no. = 12.000, b = 3.000, ϵ = 0.4000, W_{04} = 0.100, σ = 1.3025 rad., T = 0.2605
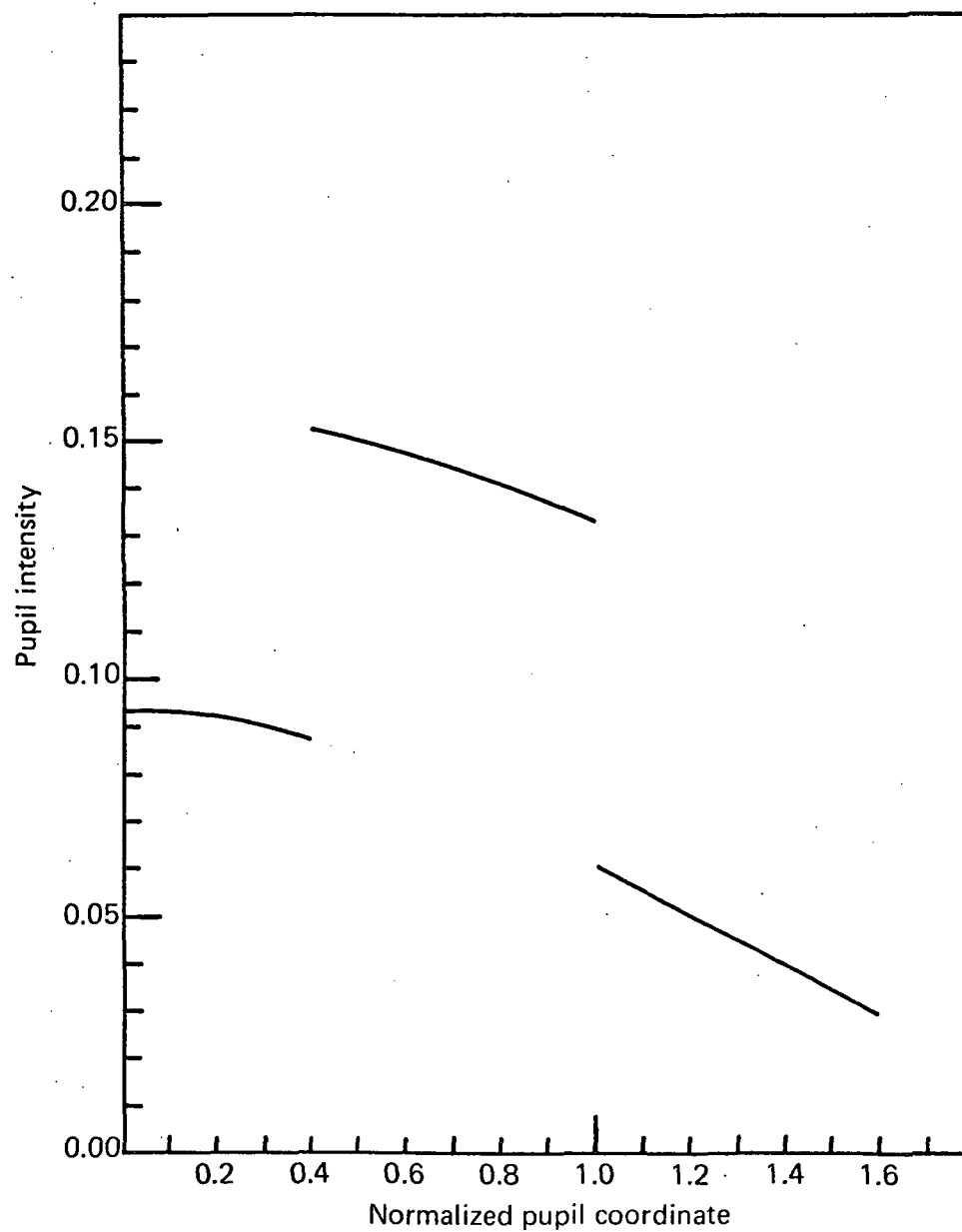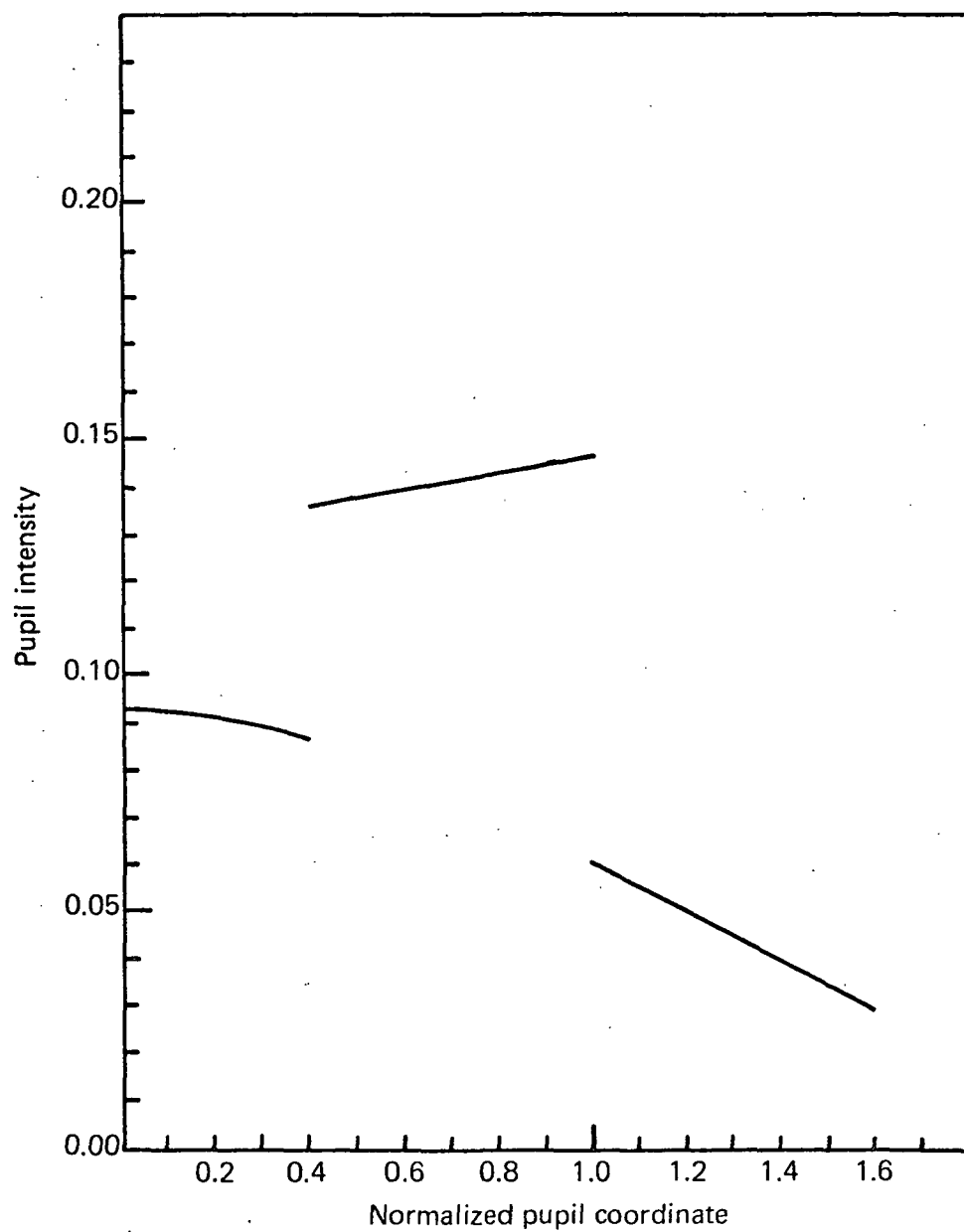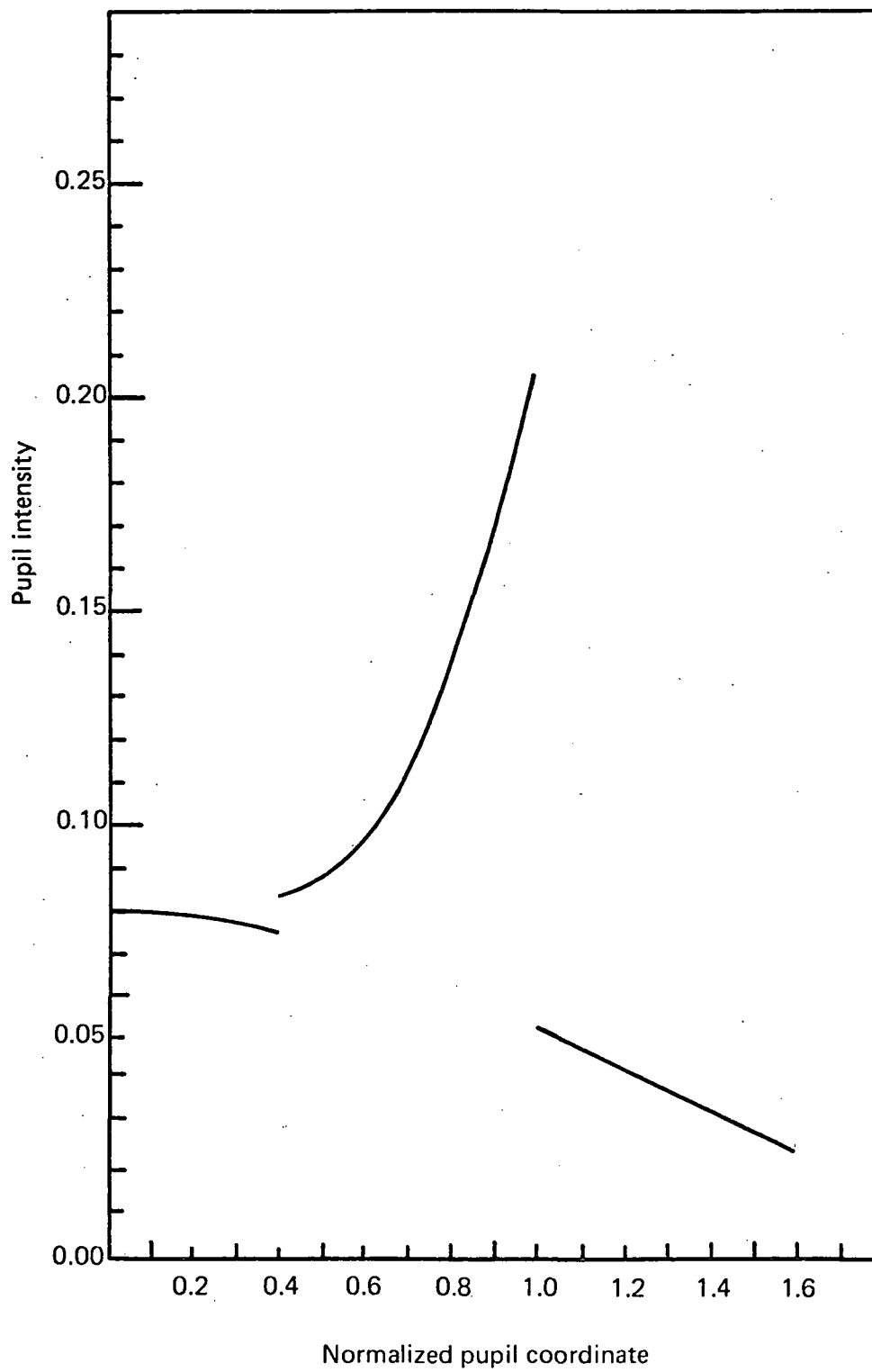
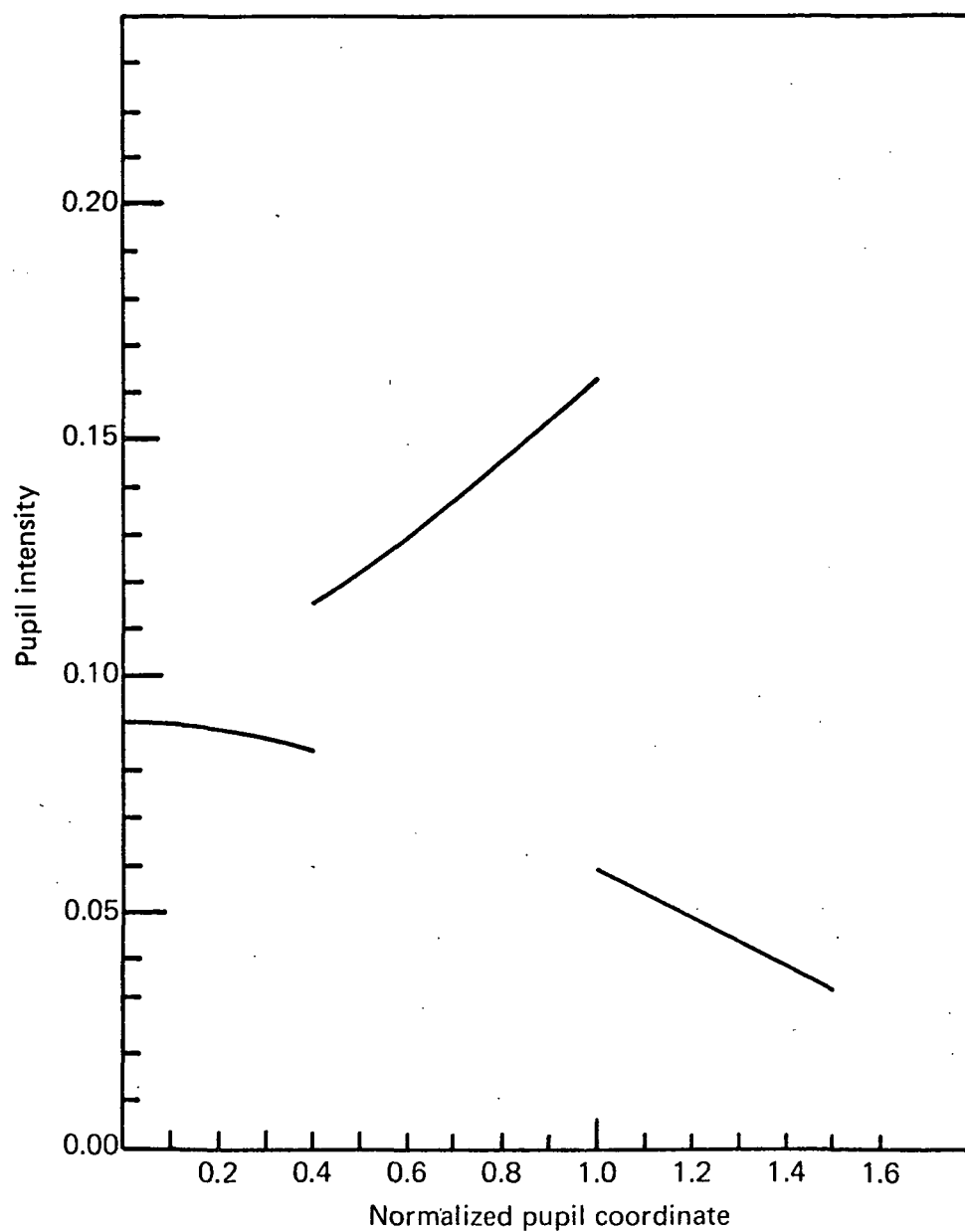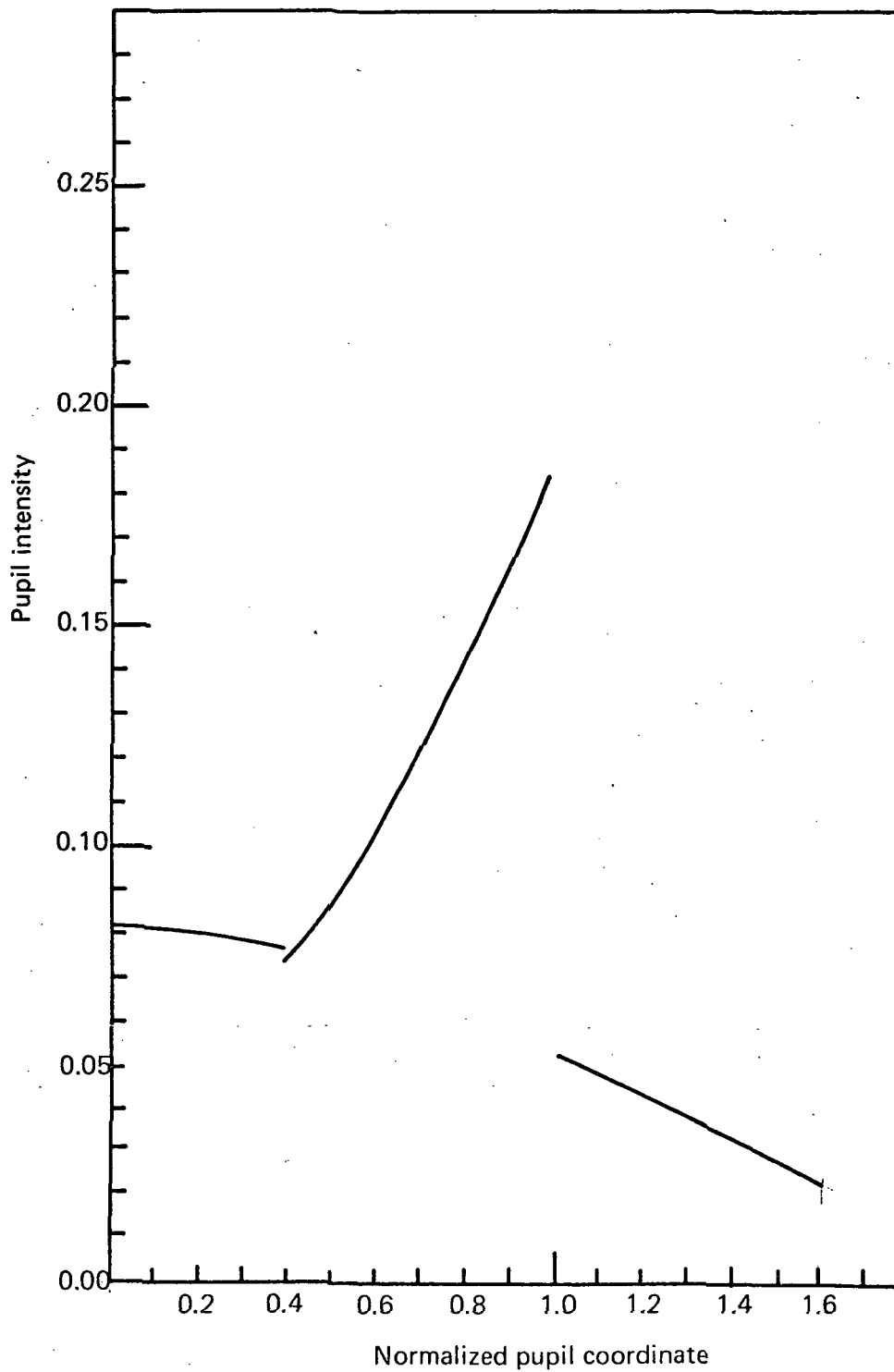Fig. 36. Reimaged pupil under the following conditions: $\lambda = 0.60\,\mu\text{m}$, F/no. = 12.000, b = 3.000, $\epsilon = 0.4000$, $W_{04} = 0.200$, $\sigma = 1.3025$ rad., T = 0.2605
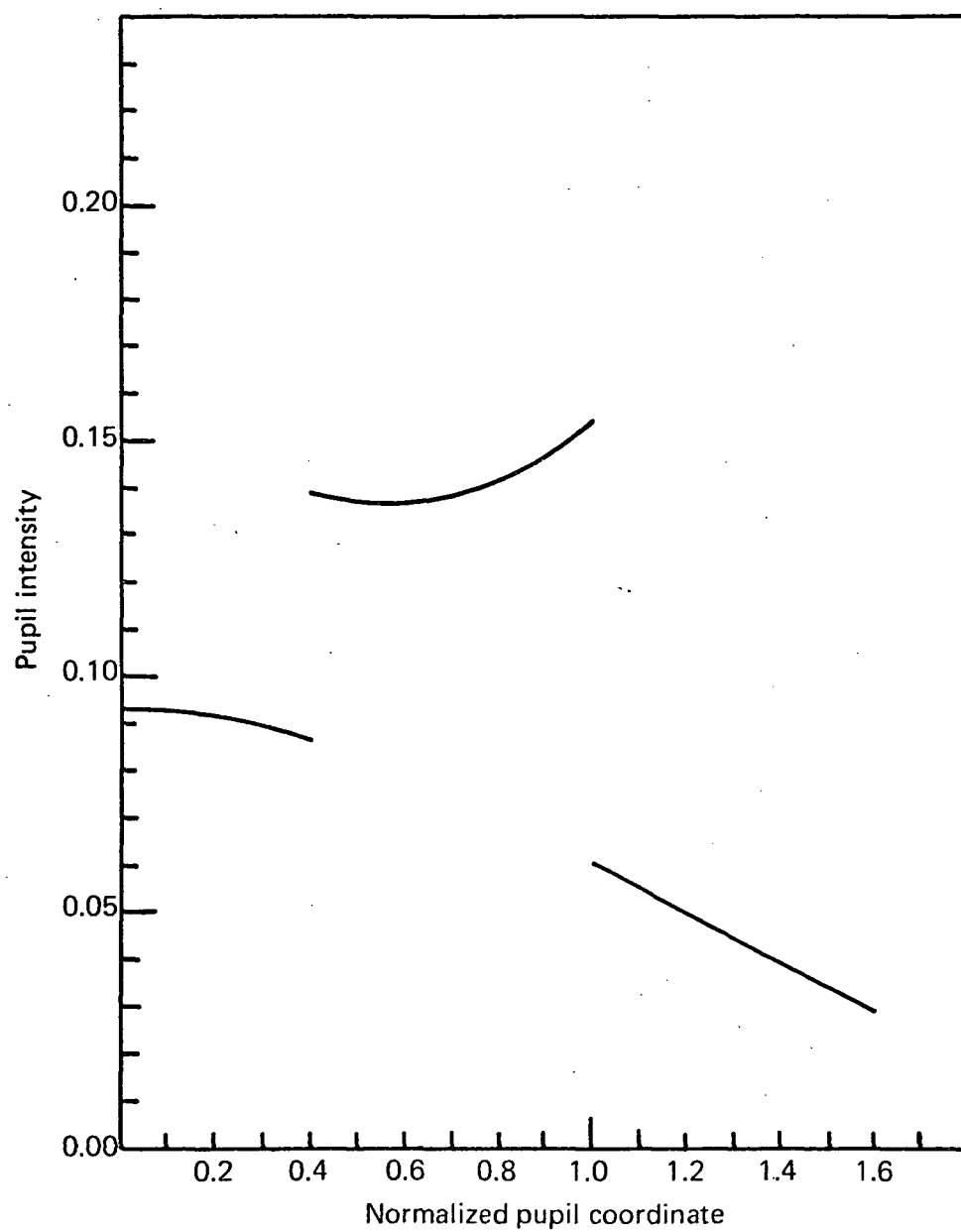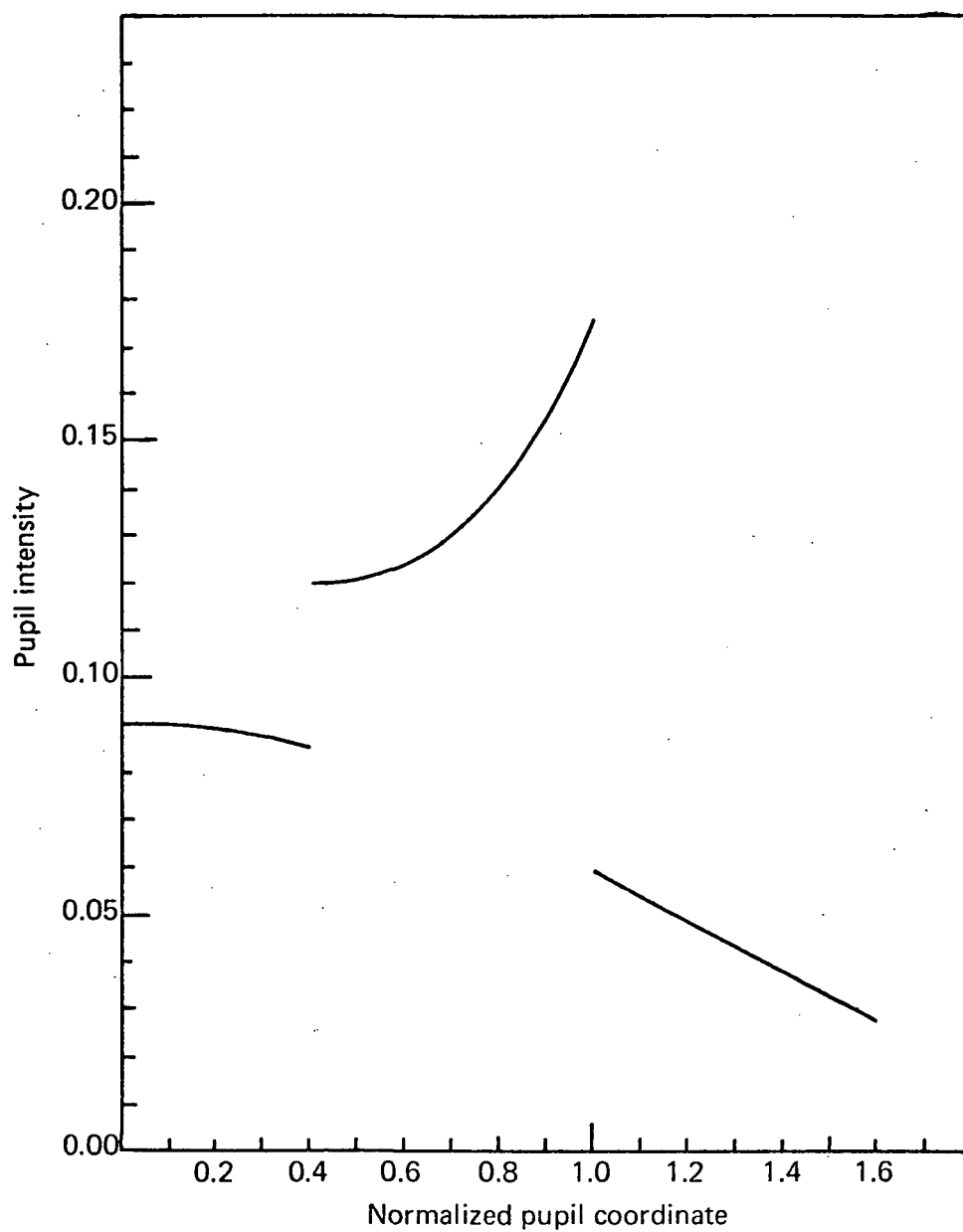
The effects of aberrations upon the $X(\rho,\theta)$ function were next analyzed. Using $X(\rho,\theta) = Q(\rho,\theta)e^{i\psi(\rho,\theta)}$ we find a very interesting and important result. Using W_{02} (defocus) as an example, the contribution to the $Q(\rho,\theta)$ term, which governs the reimaged pupil shading, is insignificant for W_{02} and even less significant for higher order aberrations. The effect of the aberration is only on the $\psi(\rho,\theta)$ term and this effect is for all practical purposes constant across the pupil. This tells us that the intensity changes we observe in the pupil will be solely a function of ϕ, the pupil aberration, except for a constant average over the reference wave passing through the Zernike disc, which affects each point in the pupil by the same constant phase shift. Indeed if we look at higher order terms we find the effects to be even less. We have included Figs. 29-36 (graphs) of reimaged pupil intensity as influenced by varying amounts of defocus and spherical aberration from $.01\lambda$ to $.2\lambda$. A comparison of these graphs with the zero-aberration case (Fig. 28) points out the sensitivity of the test.

d. Calibration of real discs.

Let us examine the graphs of the reimaged pupil, Figs. 29-36, concentrating our attention on the intensity profile outside the pupil. $(r < \epsilon; r > 1)$ This area contains, practically speaking, little of the effects of the pupil aberrations for small aberrations and is in fact the functional representation of $\frac{A^2 Q^2(\rho,\theta)}{16\lambda^4 F\#^4}$. In the case of Zernike disc manufacture we will not have perfect square-well formation of the phase delay or exact dimensions. By measuring the diffracted intensity within

ε and outside the pupil we will be able to fit a curve to determine AQ(ρ,θ), for our real Zernike disc. This information will then be used in the pupil intensity equation to calculate the zero aberration profile of the real disc. Changes in intensity due to phase errors can then be related to this baseline.

e. Tolerancing of discs.

As mentioned before, the ideal transmission and phase delay can be calculated from the equations developed for the Zernike disc. Departures from the design values in the manufacturing process will result in two main effects. The first effect is a departure from maximum visibility, and the second effect will cause a shift in the zero-aberration operating point away from the zero condition. Figure 37 shows the effect on the visibility function V as a function of phase delay with three different transmission values. It can be seen that the visibility is indeed a slowly varying function and that for gross errors of phase delay and transmission its change is not significant.

The significant effect of fabrication errors is illustrated by Fig. 38. Here we can see the shift in the operating point (the point midway between the maximum and minimum of a fringe) due to departures in phase and transmission from the design values. For example, if the phase delay upon manufacture was found to be 0.16 waves (instead of about 0.21 waves which corresponds to the 0.00 operating point) the operating point has moved 0.05 waves from the symmetrical position. The range in one direction has thus been reduced from 0.25λ to 0.20λ. The prime purpose
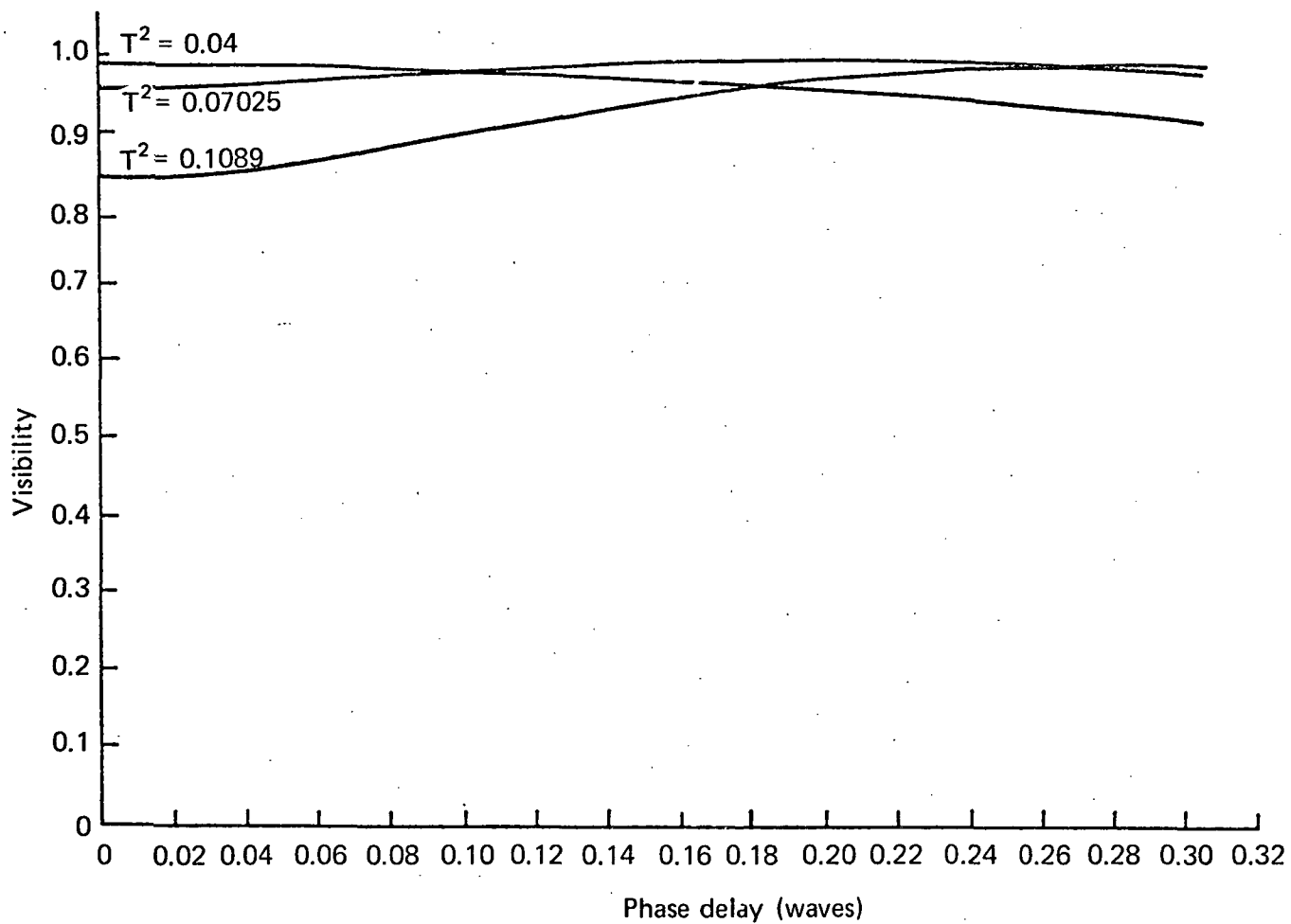
Fig. 37. Tolerance study for Zernike manufacture
$\lambda = 0.6$, $\epsilon = 0.4$, b = 3 μm
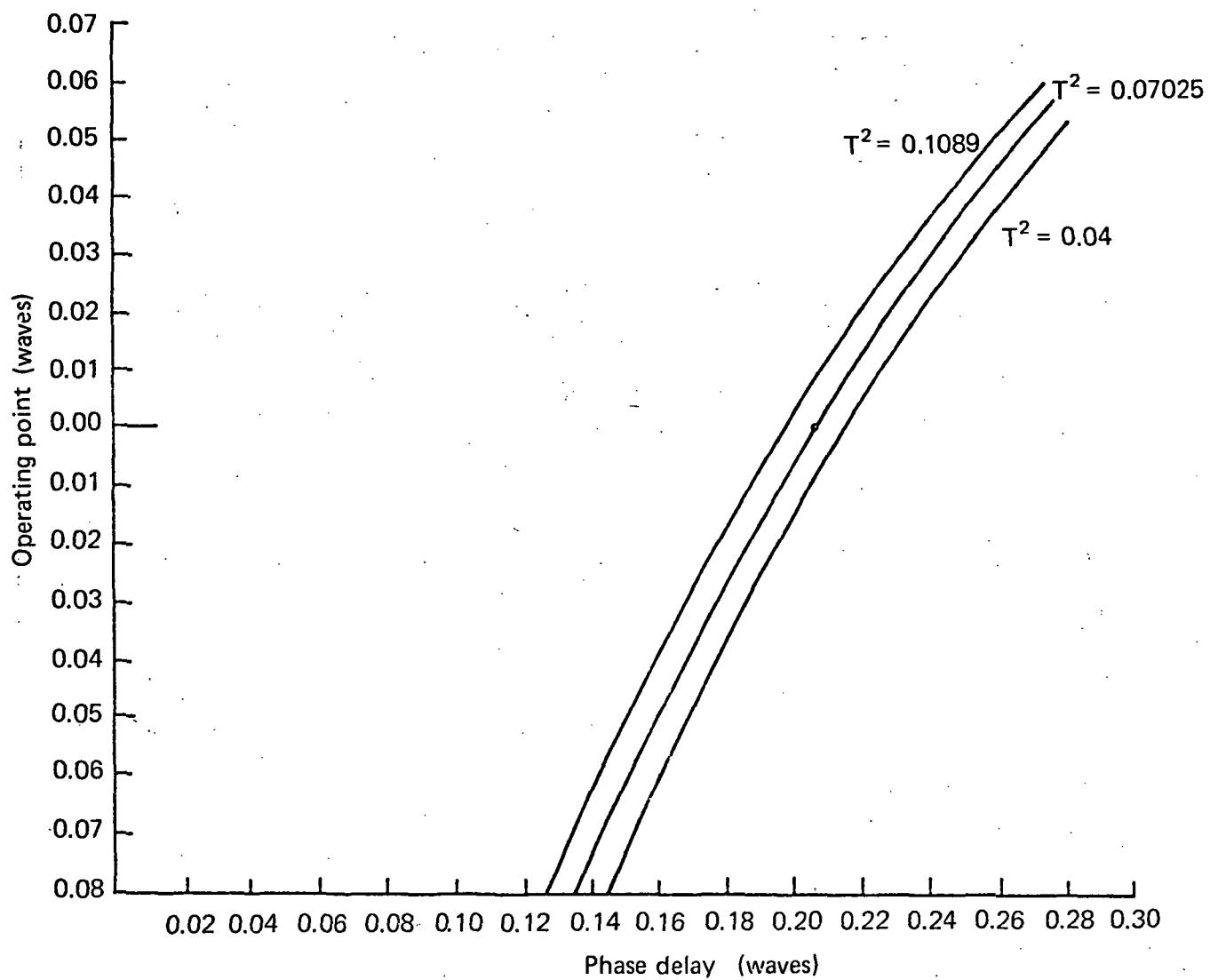
Fig. 38. Tolerance study for Zernike manufacture
$\lambda = 0.6$, $\epsilon = 0.4$, $b = 3 \ \mu m$

then of tight tolerancing will be to maintain a maximum range of operation (see Fig. 39). The other factor that influences our phase and transmission tolerancing is bandwidth. The shift in the operating point due to a finite bandwidth is $\pm \Delta\lambda/2\lambda_o$ at the edge of the bandwidth where λ_o is the nominal design wavelength. In Table VI we have tabulated the effects of error in the manufacturing process on the range of operation for the Zernike disc. For the erosion process, with careful control, and a 20 nm bandwidth the range of operation will be $\pm 1/8\lambda$ in the worst case. For testing a well-corrected system the operating range can be reduced from $\pm 0.25\lambda$ to a smaller range and the bandwidth can then be increased.

For a deposition process, assuming $\pm 1/10\lambda$ deposition control we expect $\pm 1/5\lambda$ in the worst case.

f. Signal-to-noise calculations.

One can show that in making a measurement the statistical signal-to-noise ratio due to photon noise will be:

$$S/N = \frac{\sqrt{V}}{\sqrt{2}} \frac{\sqrt{AQTNatB}}{2\lambda F\#}$$

V, A, Q, T, λ, F# are properties of the Zernike disc and the incident wavefront as defined before.

N is the number of photons per sec per cm^2 per A^o incident on telescope entrance pupil.

a is the pupil area sampled.

t is the sampling time.

B is the bandwidth.

Fig. 39. Illustration of optimum operating point.

Table VI. Error budget for Zernike disc manufacture.

Erosion range ± 1/8 λ
$\Bigg\{$
Assign ± 1/120 λ transmission = ± 2%

± 1/10 λ phase delay = ± 1/5 λ erosion depth

± 1/60 λ bandwidth = 20 nm

Deposition range ± 1/5 λ
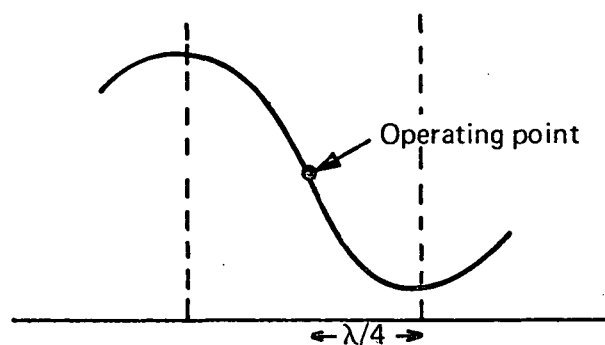$\Bigg\{$
± 1/120 λ transmission = ± 2%

± 1/20 λ phase plate = ± 1/10 λ

± 1/60 λ bandwidth = 20 nm

For a Zernike disc designed for $\xi = 0$,

$$A^2 = 1 - T^2$$

$\therefore$

$$S/N = \frac{\sqrt{V}}{\sqrt{2}} \quad \frac{\sqrt{T(1-T^2)^{\frac{1}{2}}QNatB}}{2\lambda F\#}$$

If we make two measurements, of different phases, the percent change in signal will be equal to $V\Delta\phi$ for small phase changes $\Delta\phi$. The signal-to-noise (S/N) must be greater than $1/V\Delta\phi$. From this we can obtain an expression for the number of photons required to detect a phase change $\Delta\phi$.

$$N = (NatB) = \frac{8\lambda^2 F\#^2}{\Delta\phi^4 V^3 QT(1-T^2)^{\frac{1}{2}}}$$

Figure 40 shows the minimum number of photons required to obtain $\Delta\phi = .01\lambda$, $\Delta\phi = .02\lambda$ for various size Zernike radii.

Assuming a collecting area a = 100 cm^2, a bandwidth of 20 nm and an A$_0$ type star, we have determined the integration times required for various star magnitudes. Figure 41 shows the star magnitude vs. integration time per pupil point for $\Delta\phi = .01\lambda$ for 3 μm and 4 μm radii Zernike discs, and Fig. 42 shows the same for $\Delta\phi = .02\lambda$. These calculations have assumed a *perfect* detector. For a real detector with a quantum efficiency of about 0.1, the photon requirement would have to be increased by a factor of 10 and the integration times would also have to be increased
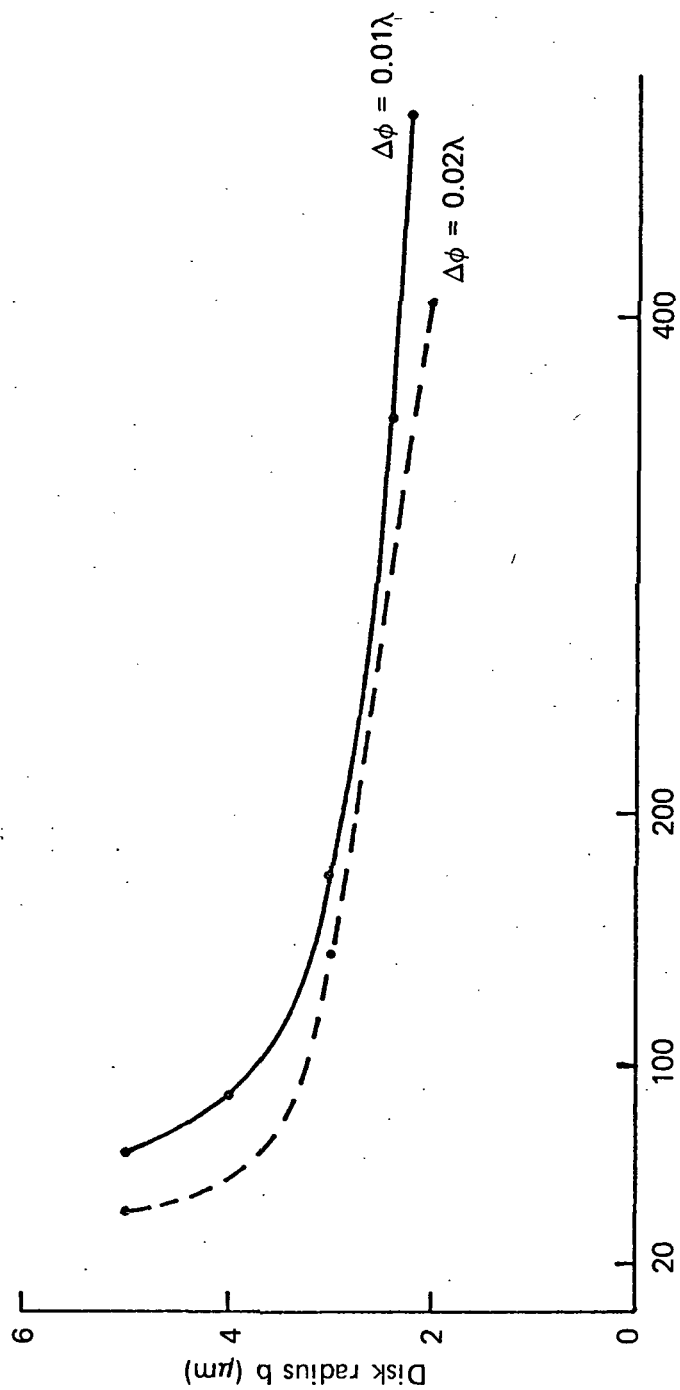
Fig. 40. Number of photons required to obtain S/N sufficient to measure $\Delta\phi$ [0.01λ, 0.02λ].

Number of photons $= $, (NatB) $= \dfrac{8\lambda^2 F^2}{\Delta\phi^4 V^3 QT(1 - T^2)^{1/2}}$
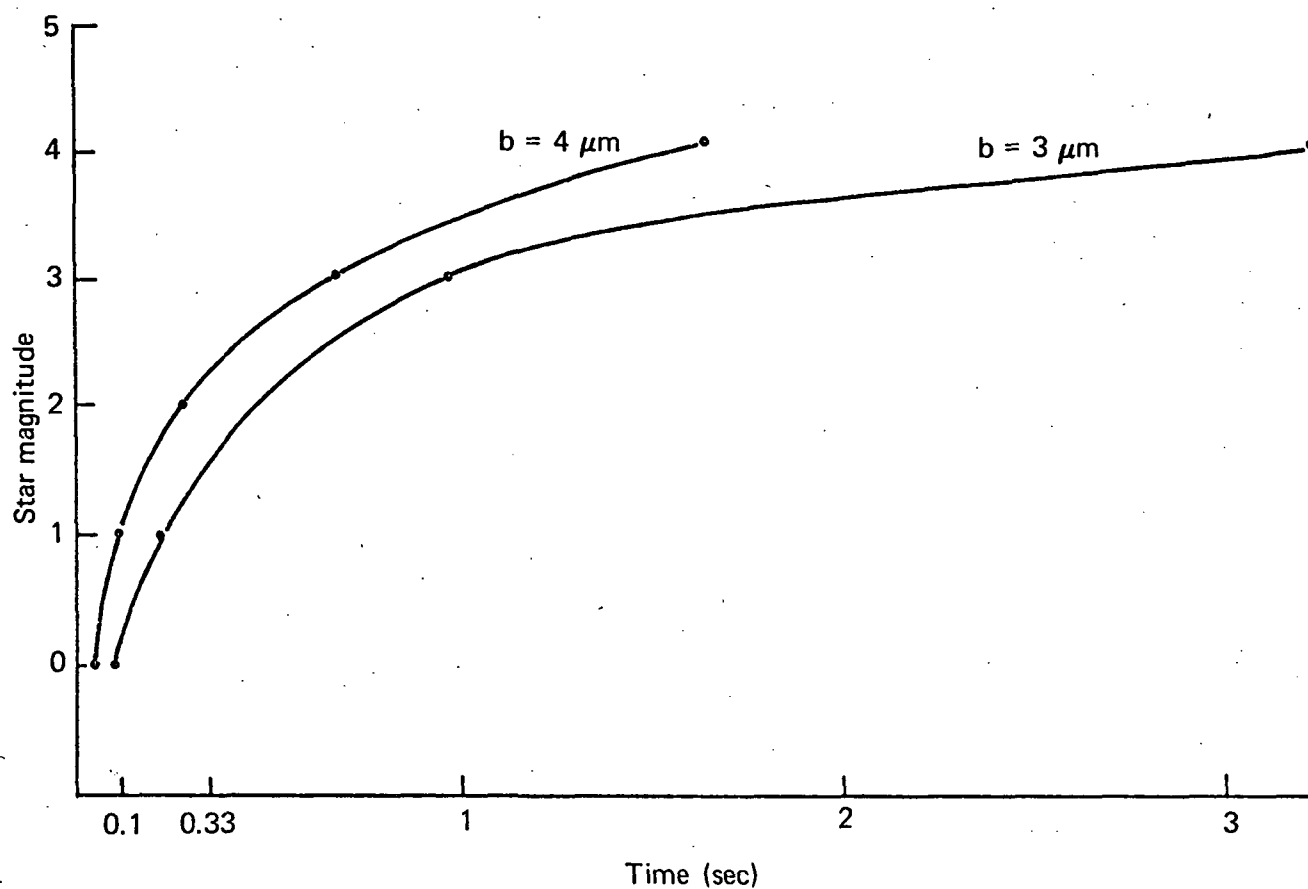
Fig. 41. Required star magnitude for λ/100 detection
A = 100 cm², Δλ = 200 Å
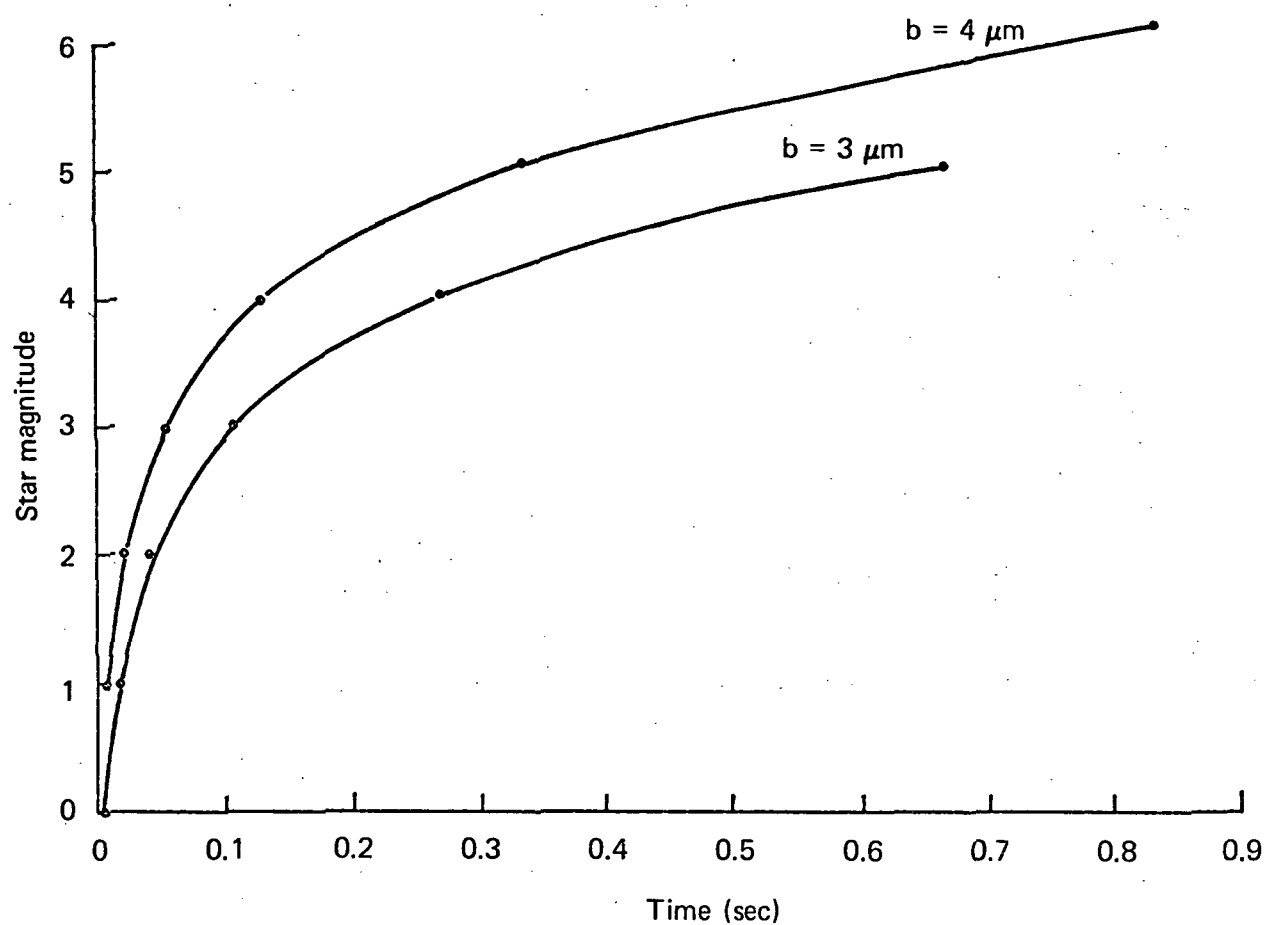
Fig. 42. Required star magnitude for λ/50 detection
A = 100 cm², Δλ = 200 Å

by a factor of 10. Thus for reasonable collection times in a real system we are talking about star magnitudes of 0 or less for the Zernike test to resolve $\Delta\phi = .01\lambda$ over the full $\pm 0.25\lambda$ range.

g. Fabrication process for Zernike discs.

Below is a step-by-step procedure for manufacturing a Zernike disc, a procedure that we developed in our clean area solid state circuitry facility. A good deal of the process is extremely sensitive to small dust particles, chemical contamination and environmental controls. These factors all influence the success or failure of the process. In summary dust must be minimized, care must be taken to avoid chemical contamination, and the temperature and humidity must be regulated in order to achieve repeatable results.

i. Zernike Manufacture (Erosion Method)

1. Clean substrate.

2. Coat with aluminum to specified transmission.

3. Clean substrate.

4. Spin on photoresist.

> Shipley: AZ-1350
> Spinner: ~ 5,000 rpm for 20 sec.

5. Bake at 75°C for 10 min.

6. Expose with mask in UV.

7. Develop in AZ-Developer--45 sec.

> A. (1:1 dilution).
> B. Rinse in deionized water.

8. Bake 20 min. at 120°C.

9. Etch.

    A. Aluminum Etch.

        4 mℓ HNO_3

        18 mℓ deionized H_2O May heat to increase etch rate.

        80 mℓ H_3PO_4

    B. Glass Etch. Rate (23°C): 1.4 μ/min.

        5:5:1

        $H_2O:NH_4F_2:HF$

10. Photoresist removal.

    J-100 at ~80°C

    Rinse in deionized H_2O

    Dry - N_2

11. Inspect.

ii. Zernike Manufacture - Metal Phase Shift Effect.

We have developed the equations which describe the optimum transmission and phase delays. Ideally we would like the phase delay to be introduced by the erosion process and the attenuation introduced by the aluminum coating. However, because of the complex index of refraction and finite thickness of the metal we must make corrections to account for the phase delay introduced by the metal. We have calculated the *phase advance* θ, introduced by the metal for various values of thickness d and also the transmissions for various values of d. This information appears in Fig. 43. By referring to this graph and table V for T^2 and σ we can calculate the required depth of erosion in our substrate using the equation:

$$t = (\theta + \frac{d}{\lambda} + \sigma) \div (n - 1)$$

where θ = phase advance produced by Al in waves

d = thickness of the Al film

λ = wave length

σ = required retardation in waves

n = index of refraction of substrate.

As an example for a 3 μ radius Zernike disc at 600 nm, we require that T^2 = 7 %, and σ = .206 λ. From Fig. 43, we obtain θ = .121 λ and d = 11. nm. Taking n = 1.516 we obtain:

$$t = (.121 + \frac{11}{600} + .206) \div (.516)$$

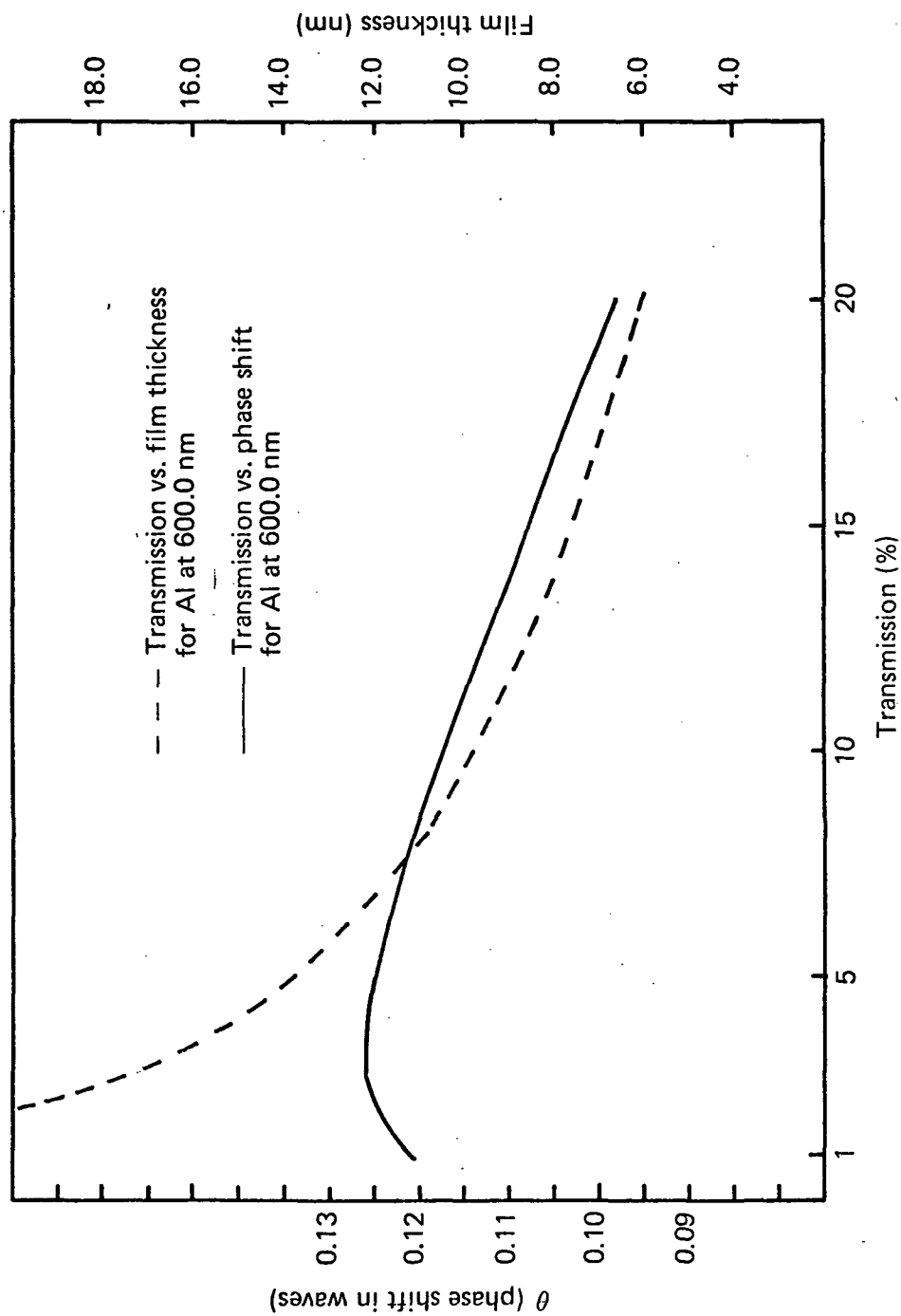$$t \simeq .67 \text{ waves (at 600.00 nm)}$$

Fig. 43. Transmission thickness and phase shift for aluminum films used in Zernike manufacture.

2. Polarization Interferometers.

a. General discussion.

Polarization interferometers have generally been used up to now as devices for creating fringes. We can gain maximum sensitivity by taking phase information and converting it into states of linear polarization using a sensor which can read out the polarization state and thus obtain a phase reading. An instrument with a polarization readout in a Twyman-Green configuration has been built at the Optical Sciences Center and has demonstrated sensitivities of $1/500\lambda$. This is to be compared with a $1/50\lambda$ sensitivity of the traditional two-beam fringe reading Twyman-Green interferometer. The Twyman-Green instruments, of course, operate with an artificial source which generates a nearly perfect reference wave. Since we are using a real star source we have to generate our own reference. Two possibilities are: 1) the use of some sort of polarization pupil shearing technique, such as the lateral shear, which we have chosen for laboratory purposes or, 2) the use of a method similar to the Zernike phase test, except operating in a polarizing sense, which can generate its own nearly perfect reference wave. The first concept we call the shearing polarization interferometer and the second the Zernike polarization disc interferometer.

b. The Shearing Polarization Test.

There are many types of shear (lateral, radial, inverting, etc.), which can be used to produce interference effects between two points in the pupil of an optical system. For laboratory simplicity we have chosen to illustrate, analyze and construct a polarizing lateral shearing device.
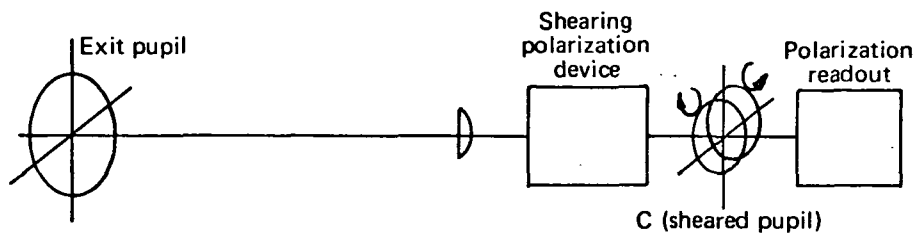
Fig. 44

$$\psi = (\Delta_A - \Delta_B)/2$$
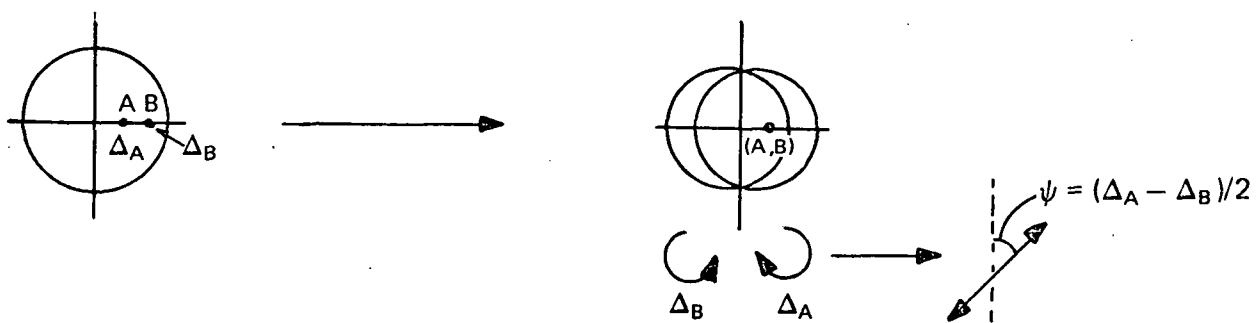
Fig. 45

Polarization shearing concepts.

The basic idea is as follows: In Fig. 44 we have the exit pupil of

the system which in gneral will be in some partially polarized state.

We then reimaged this pupil at C through the polarizing interferometer

as follows. By means of a polarizer we put the wavefront into a linear

polarized state. This linear polarized pupil is then operated on by

a series of optical elements to produce at C two images of the system

exit pupil slightly displaced from one another such that one image is

right-circularly polarized and the other image is left-circularly

polarized. If we now look at a point in the sheared pupil image we

have light right-circularly polarized from point A interfering with light

left-circularly polarized from point B. If point A has phase Δ_A and

point B has phase Δ_B , the two oppositely-circularly polarized coherent

beams combine to produce a linearly polarized beam such that

$$\psi = \frac{\Delta_A - \Delta_B}{2} ,$$

where ψ is the direction of linearly polarized light. This is illus-

trated in Fig. 45. We now use some sort of device to detect this linear

polarization state and thus can obtain a direct measurement of the

sheared phase $(\Delta_A - \Delta_B)$ across the pupil.

i. Ways of Producing the Sheared Polarization States.

There are many possible ways of obtaining the desired orthogonal

circularly polarized sheared pupil condition at point C, and several of

these illustrated below, with some brief comments.

Figure 46 shows a neat, compact unit where the shear in the pupil is produced by displacement of the two halves of the modified pentaprism along the polarizing beamsplitter plane A-B. Plane polarized light at 45° is then passed through the prism and sheared into two orthogonal states of polarization. These two orthogonal states then emerge at D where they pass through an achromatic quarter wave plate at 45° which in turn yields two oppositely-circularly polarized pupils at plane C. We have a compact unit where the shear is easily varied from zero to any value by movement along A-B. We require manufacture using very low birefringence glass so as to maintain linear polarization states. For greater stability one could replace the second right angle prism with another prism. The above arrangement is achromatic in collimated light.

Figure 47 shows a compact way of obtaining circularly-polarized light by using two Wollaston prisms. The amount of shear is controlled by the separation of the two matched prisms with the scaling factor set by the prism angle θ, the unit being naturally achromatic with the main advantage in the compactness. Two disadvantages are in not being able to go to zero shear, and the large separation D required for large shears, which may result in uncompensated path differences and coherence length problems. This device appears most suitable for a small fixed shear mode where the two prisms are made into a single unit. In this case we have a single compact shearing mechanism.

In Fig. 48 we have a polarizing beamsplitter A-B. The shear is introduced by tilting a right angle prism about axis O. The shear is given by

$$S = 2t \sin u \left[1 - \left(\frac{1-\sin^2 u}{n^2-\sin^2 u}\right)^{\frac{1}{2}}\right]$$

where t is the total thickness of the upper prism and u is the tilt angle. And

$$S = 2tu \left[\frac{n-1}{n}\right]$$

for small values of u.

In this case we can vary our shear from zero upwards. However, at large shears the variation is very nonlinear and wavelength dependent shear effects can be large. Low birefringence glass is required.

In the simple arrangement shown in Fig. 49. A Wollaston prism is placed at the system focus. We have a fixed shear determined by the prism angle θ. Lens B will affect the polarization orthogonality of the shear and the arrangement is very sensitive to positioning of the prism. The shear itself is no longer achromatic.

Summary

There are other ways of introducing orthogonally-polarized sheared pupils either with birefringent materials or by using polarizing beam-splitters with tiltable glass plates or mirrors. Of the concepts presented, based on maximum versatility and simplicity, the first would be preferred.
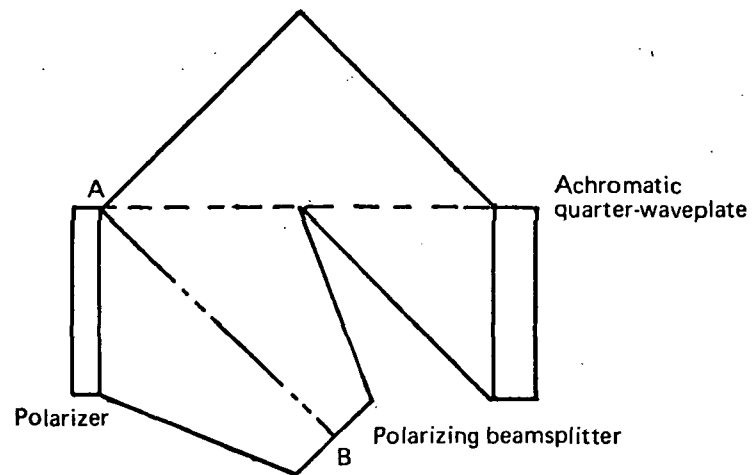
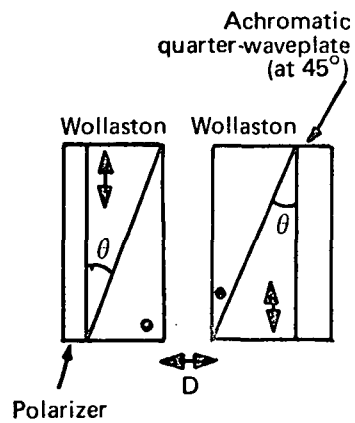Fig. 46. Pentaprism polarization shearing device.

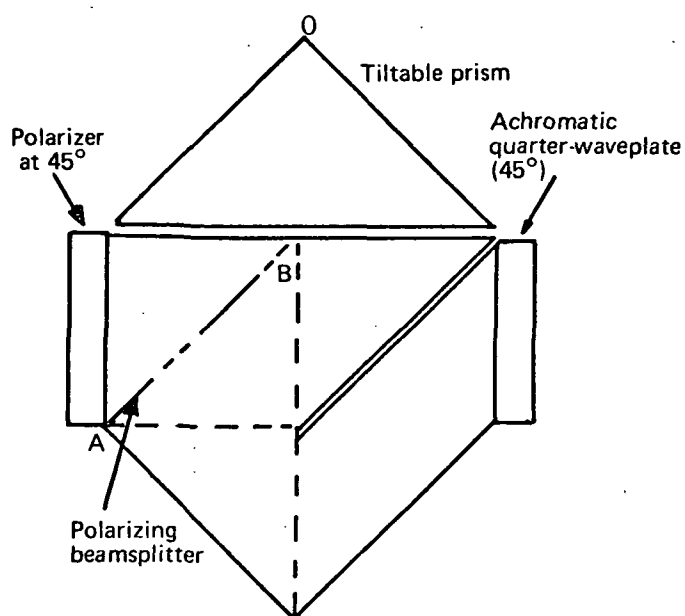Fig. 47. Double Wollaston prism polarization
shearing device.

Fig. 48. Polarizing beamsplitter tiltable prism polarization shearing device.
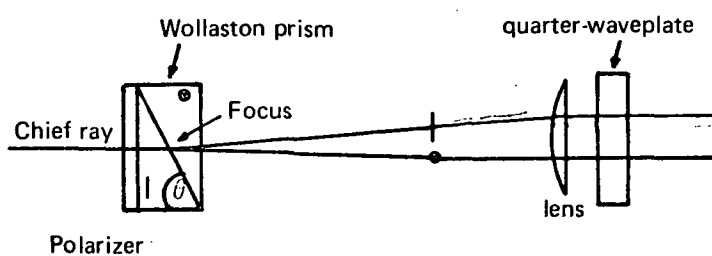
Fig. 49. Single Wollaston prism polarization shearing device.

Based on simplicity with limited versatility the second would be pre-
ferred. For laboratory purposes and since we could use off-the-shelf
components we have designed our shearing unit about this second concept.

c. Ways of Reading Out Polarization States.

We discuss here two possible ways of reading out polarization
states.

i. Using a single rotatable Wollaston prism.

Assuming we have produced two oppositely-circularly polarized
sheared pupil images at C in Fig. 44, we know that these two coherent
beams combine to produce a state of linear polarization where the angle
is

$$\psi = \frac{\Delta_A - \Delta_B}{2} .$$

Behind this we position a Wollaston prism and a decollimating lens D, as
in Fig. 50. If the original zero aberration position of the Wollaston
prism was at 45°, we rotate this prism until the two oppositely-polarized
intensities are equal. We can measure these intensities by use of an
image dissector tube with deflection coils, in a synchronous amplifica-
tion scheme (Fig. 50). We would thus rotate the Wollaston toward a null
signal and encode the rotation, where a rotation of 1/60 radian ($\sim$1°)
corresponds to a phase measurement $\Delta_1 - \Delta_2$ of $\sim \lambda/190$.

We have chosen to simulate this scheme in the laboratory because
of its simplicity. However, instead of using an image dissector we
simulate the dissector with two counter-rotating prisms as illustrated in

Fig. 50. Single channel polarization readout with image dissector.
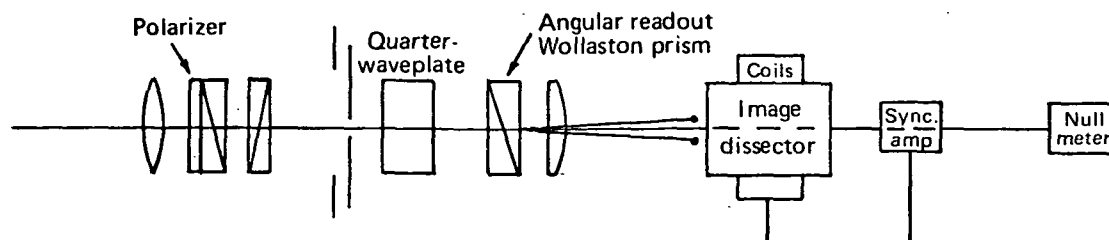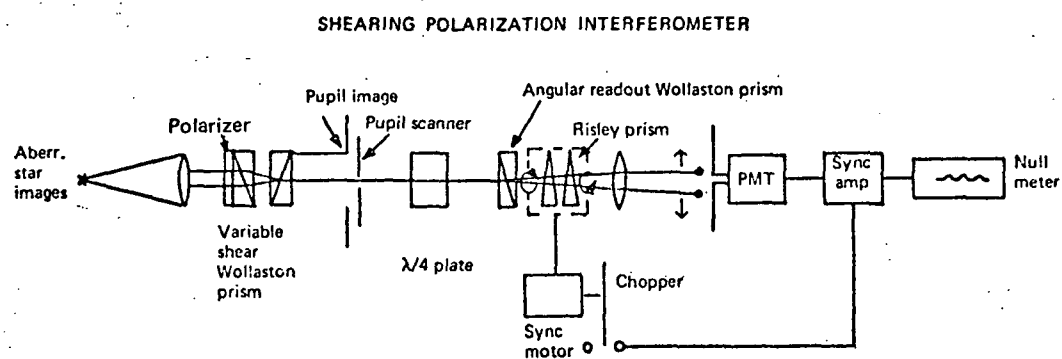

Fig. 51. Laboratory simulation of shearing polarization interferometer.

Fig. 51. We thus sequentially sample one of two beams at 28 cps and synchronously amplify the difference signal. The Wollaston prism is rotated until this signal is minimized and this rotation is recorded.

ii. The two-channel device.

If we use the optical arrangement illustrated in Fig. 52 we get difference signals in each channel. In channel one, with the quarter-wave plate fast axis located at +45°, we obtain a sinusoidally modulated signal where $\Delta I_1 = I_1 - I_2 = K \sin(\Delta_1 - \Delta_2)$ and in channel two with the quarter-wave plate fast axis oriented at -45° we obtain $\Delta I_2 = K \cos(\Delta_1 - \Delta_2)$. The circuits are balanced for equal gain. Then the signals are divided so that

$$\frac{\Delta I_1}{\Delta I_2} = \tan(\Delta_1 - \Delta_2),$$

and then the $\arctan(\Delta I_1 / \Delta I_2)$ is taken. All of this is done electronically without the need for movement of any components. As with the other scheme it is insensitive to source fluctuations. This type of readout has been utilized in a Twyman-Green configuration instrument constructed at OSC and phase errors of $1/500\lambda$ have been measured.

d. Discussion of the Polarization Intensity Equations Including Alignment and Fabrication Errors.

Below we drive expressions for the intensities of the sheared pupil signals as a function of (1) unbalanced signal amplitudes between two polarization states, (2) angular positioning of components and

Synchronous differential amp

Image
dissector

Channel two
$\Delta I = K \cos(\Delta_1 - \Delta_2)$

Polarizer

Wollaston
Quarter-waveplate

Synchronous
differential
amp

arc
tan

$(\Delta_1 - \Delta_2)$

Image
dissector

Aberrated
star source

Wollaston
prisms

Beamsplitter

Wollaston
Quarter-waveplate

Channel one
$\Delta I = K \sin(\Delta_1 - \Delta_2)$

Sheared
pupils
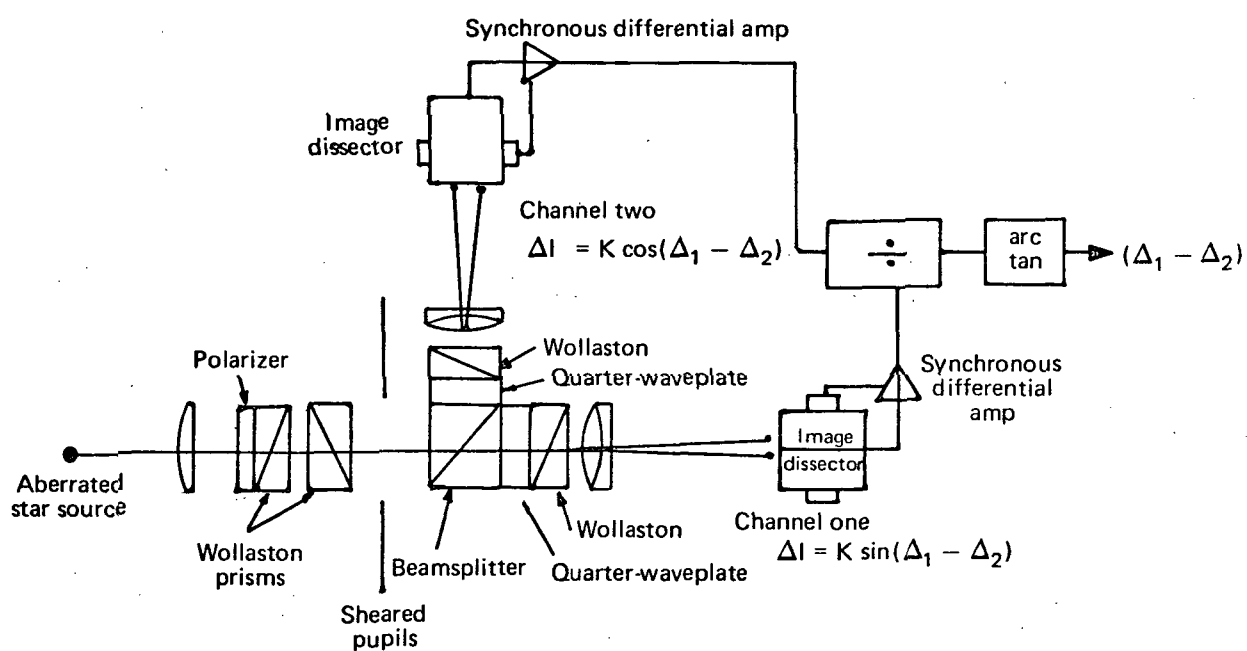
Fig. 52. Two-channel shearing polarization interferometer.

(3) departure from perfect quarter-wave plate delay.

Let us assume that the polarizer-shearing combination produces a shear in the y direction, as illustrated, Fig. 53, where the amplitude of one polarization is

$$E_\perp e^{i\Delta(x,y-\frac{S}{2})}$$

and the other is

$$E_\parallel e^{i\Delta(x,y+\frac{S}{2})},$$

and where S is the total shear.
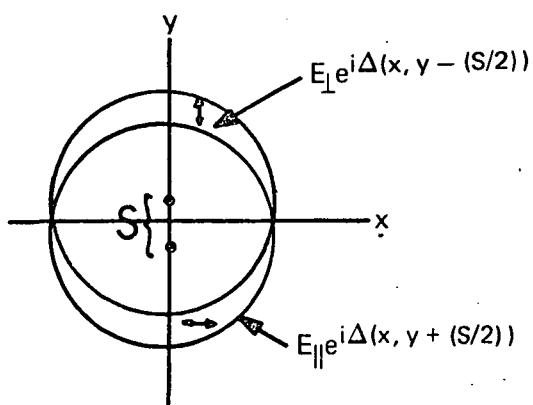
Fig. 53. Sheared pupil geometry.

These signals then pass through the quarter-wave plate oriented at some angle θ, with respect to the x axis. (Ideally $\theta = \pm 45°$, depending on whether we desire sin or cos modulation, as discussed in the previous section.) The plate advances the phase by $\frac{\pi}{2} + \delta$ for the fast axis over the slow axis.

The field passing through the fast axis is:

$$E_\theta = e^{i(\frac{\pi}{2} + \delta)} [E_\perp e^{i\Delta(x,y - \frac{S}{2})} \sin\theta + E_{//} e^{i\Delta(x,y + \frac{S}{2})} \cos\theta].$$

The field passing through the slow axis direction is:

$$E_{\theta+90°} = E_{//} e^{i\Delta(x,y + \frac{S}{2})} \sin\theta - E_\perp e^{i\Delta(x,y - \frac{S}{2})} \cos\theta.$$
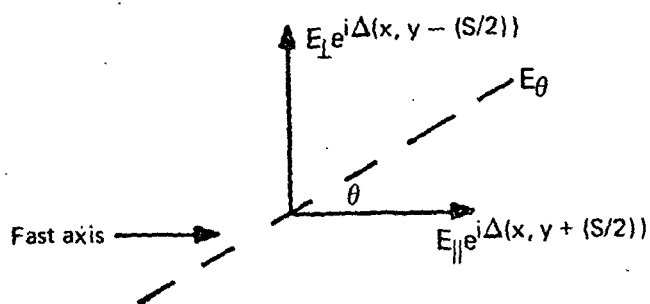
We now orient a Wollaston prism at an angle ψ with respect to the x axis. Light through this prism then produces one signal polarized in the ψ direction and another polarized at ψ + 90°.
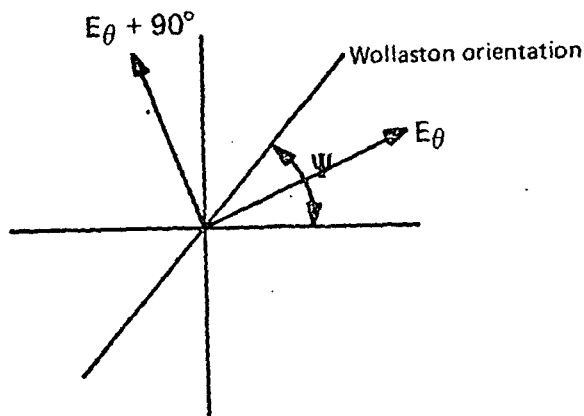
The output through the Wollaston is thus

$$I_\psi = E_\psi E_\psi^* = |E_\theta|^2\cos^2(\theta-\psi) + |E_{\theta+90}|^2\sin^2(\theta-\psi)$$

$$+ 2\text{Re } E_\theta E_{\theta+90} \cos(\theta-\psi)\sin(\theta-\psi)$$

$$I_{\psi+90°} = E_{\psi+90}E_{\psi+90}^* = |E_{\theta+90}|^2\cos^2(\theta-\psi)$$

$$+ |E_\theta|^2\sin^2(\theta-\psi)$$

$$- 2\text{Re } E_\theta E_{\theta+90} \cos(\theta-\psi)\sin(\theta-\psi).$$

We now substitute for E_θ, and $E_{\theta+90}$ and assume δ is small so that

$$e^{i(\frac{\pi}{2} + \delta)} \approx i - \delta.$$

This yields

$$I_\psi = \left[[E_\perp^2\sin^2\theta + E_{//}^2\cos^2\theta + E_\perp E_{//}\sin2\theta]\cos^2(\theta-\psi) \right.$$

$$\left. + [E_\perp^2\cos^2\theta + E_{//}^2\sin^2\theta - E_\perp E_{//}\sin2\theta]\sin^2(\theta-\psi)\right]\cos\Delta$$

$$- E_\perp E_{//}\sin(2\theta-2\psi)\sin\Delta$$

$$+ \delta \left[[E_\perp E_{//}]\cos\Delta - (E_{//}^2-E_\perp^2) \frac{\sin2\theta}{2}\right]\sin(2\theta-2\psi)$$

$$I_{\psi+90°} = [E_{||}^2\sin^2\theta + E_{\perp}^2\cos^2\theta - E_{\perp}E_{||}\sin 2\theta]\cos^2(\theta-\psi)$$

$$+ [E_{||}^2\cos^2\theta + E_{\perp}^2\sin^2\theta + E_{\perp}E_{||}\sin 2\theta]\sin^2(\theta-\psi)\ \cos\Delta$$

$$+ E_{\perp}E_{||}\sin(2\theta-2\psi)\sin\Delta$$

$$- \delta[E_{\perp}E_{||}\cos\Delta - (E_{||}^2-E_{\perp}^2)\frac{\sin 2\theta}{2}]\sin(2\theta-2\psi)$$

We now substract the two signals:

$$I_{\psi+90°} - I_{\psi} = 2E_{\perp}E_{||}\sin\Delta\sin(2\theta-2\psi)$$

$$- 2E_{\perp}E_{||}\sin 2\theta\cos\Delta\cos[2\theta-2\psi)$$

$$- \delta S[E_{\perp}E_{||}\cos\Delta - (E_{||}^2-E_{\perp}^2)\frac{\sin 2\theta}{2}]\sin(2\theta-2\psi)$$

i. Possible Operating Conditions for Two Channel Device

Neglecting δ for the present:

If $\theta = 45°$, $\psi = 0$ $\theta = 0$, $\psi = 45°$

$\Delta I = 2E_{\perp}E_{||}\sin\Delta$ $\Delta I = 2E_{\perp}E_{||}\sin\Delta$

If $\theta = -45°$, $\psi = -45°$ $\theta = -45°$, $\psi = -45°$

$\Delta I = 2E_{\perp}E_{||}\cos\Delta$ $\Delta I = 2E_{\perp}E_{||}\cos\Delta$

We see we have two possible operating conditions for the two-channel device.

ii. Departure from perfect quarter wave plate.

In the one-channel device ψ is rotated until $\Delta I = 0$, or

$$\tan\Delta = \frac{1}{\sin 2\theta} \tan(90 - 2\theta + 2\psi) + \delta - \frac{(E_{\parallel}^2 - E_{\perp}^2)\delta}{2E_{\perp}E_{\parallel}\cos\Delta}$$

With the orientation of the quarter wave plate fast axis at $\theta = 45°$, as far as tolerancing on δ goes, we see that for small phase errors the second error term will be a small fraction of the first. We can manufacture a quarter wave plate with $\delta \approx \pm 1/100$ or less over 1000 A° bandwidth.

$$\therefore \quad \bar{\delta}_{ave} << \frac{1}{100} \quad \text{and} \quad \tan\Delta = \tan 2\psi + \delta.$$

The effect on small phase errors $\Delta \approx \lambda/200$ will be to introduce a constant offset error $\bar{\delta}$, the constant offset being less than $\pm \lambda/500$. This constant correction would hold beyond Δ becoming somewhat greater $1/20\lambda$. Beyond this, the correction would get smaller for larger aberrations. If it were desired one could measure δ over the passband of the instrument and determine the average δ, $\bar{\delta}$, and compensate for measured values.

iii. Alignment of quarter wave plate.

Now let us examine small errors in θ, $\Delta\theta$. $\theta = 45° \pm \Delta\theta$.

$$\tan\Delta = \frac{1}{\cos(90 - 2\Delta\theta)} \tan(90 - 2\theta + 2\psi)$$

$$\tan\Delta = \frac{1}{\cos(2\Delta\theta)} \tan(2\psi - 2\Delta\theta).$$

The cos(2Δθ) effect is negligible for small Δθ of a few degrees,

$$. \cdot \cdot \quad \tan\Delta = \tan(2\psi - 2\Delta\theta)$$

$$\Delta = 2\psi - 2\Delta\theta.$$

We see that the effect of the quarter-wave plate misalignment is to introduce a constant bias of 2Δθ in the measurements, if Δθ is kept to ±2°.

e. Bandwidth Considerations.

i. General discussion.

If $\theta = 45°$ we arrive at an error signal $\Delta I = I(\lambda)\sin(\Delta-2\psi)$,

$$\Delta = \frac{2\pi}{\lambda} x \qquad \text{x is physical path difference between the sheared points.}$$

$$\Delta = Kx \qquad K = 2\pi/\lambda$$

$$\Delta I = I(K)\sin(Kx-2\psi)\Delta K \text{ for monochromatic radiation of bandwidth } \Delta K.$$

If we have a bandwidth of ± ΔK/2 and if we take into consideration the weighted spectral response of the detector, the shape of the bandpass filter and the distribution of the radiation we obtain an integrated effect. If the weighted function is symmetric about a K_{ave} we will show below that

$$\Delta I = \sin(K_W x - 2\psi)F(x, B(K), S, R)\Delta K$$

K_W is the weighted average wave number.

$F(x, \Delta K, S, R)$ is a function depending on the spectral
distribution S, responsivity R, bandpass
filter function B(K), and x.

It is desirable to have $F \approx 1$ and a much slower varying function of x than the sine function. If we consider the case of narrow bandwidths S, R can be assumed constant. If we take ΔK to be a square bandpass we find that:

$$\Delta I = \sin(K_{ave}x - 2\psi)\text{sinc } x\Delta K \Delta K.$$

If $\Delta\lambda = \pm 250^{\circ}A$, and for the range of x, $\Delta Kx \approx 0$, thus:

$$\text{sinc } x\Delta K \approx \text{const.} \approx 1.$$
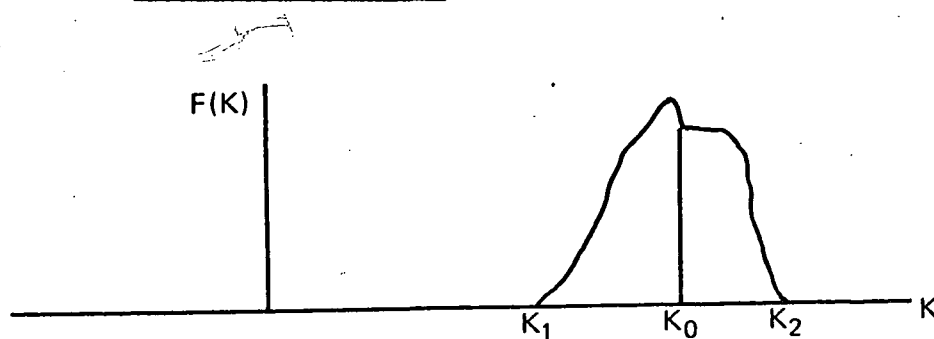
And

$$\Delta I \approx \sin (K_{ave}x - 2\psi)\Delta K,$$

for a narrow band where

$$K_{ave} = \frac{K_{max} + K_{min}}{2}.$$

ii. General Theory

In the above sketch F(K) represents the spectral energy distribution multiplied by the filter response multiplied by the detector response. The error signal for a setting ψ of our readout prism is

$$\Delta I = \int_{K_1}^{K_2} F(K)\sin(Kx - 2\psi)dK.$$

In the monochromatic case we have seen that $\Delta I = 0$, if $2\psi - Kx$. We would like to see the effect of this general radiation function $F(K)$ on our error signal ΔI.

$$\sin(Kx - 2x) = \frac{1}{2i}(e^{iKx}e^{-i2\psi} - e^{-iKx}e^{i2\psi})$$

$$\therefore \quad \Delta I = \frac{1}{2i}e^{-i2\psi}\int_{K_1}^{K_2}F(K)e^{iKx}dK - e^{i2\psi}\int_{K_1}^{K_2}F(K)e^{-iKx}dK$$

$$\Delta I = \text{Imaginary part of } e^{-i2\psi}\int_{K_1}^{K_2}F(K)e^{iKx}dK$$

$$\Delta I = \text{Im } e^{i(K_0x-2\psi)}\int_{-(K_1-K_0)}^{K_2-K_0}F(K)e^{iKx}dK$$

Here we have used the fact that $F(K)$ is real, and the shift theorem of Fourier transforms, where K_0 is the weighted average

Now $F(K)$ can be written as the sum of an even and odd function.

$$F(K) = EF(K) + OF(K)$$

$$\therefore \quad \Delta I = \text{Im}e^{i(K_0x-2\psi)}\int(EF(K)e^{iKx}dK + \int OF(K)e^{iKx}dK$$

The Fourier transform of an even function is real and even, and the Fourier transform of an odd function is imaginary and odd. Thus we obtain:

$$\Delta I = \sin(K_0x-2\psi)F(EF) + i\cos(K_0x-2\psi)F(OF),$$

where F denotes Fourier transform.

We note that for any even distribution function our error signal is of the same functional form as in the monochromatic case, where K_o is the weighted average wave number. In the case of a nonsymmetric distribution, the odd part of the distribution will cause in general an inability to obtain the null condition at $K_o x - 2\psi = 0$. Then condition for nulling now becomes:

$$\tan(K_o x - 2\psi) = -\frac{iF(OF)}{F(EF)}, \qquad \text{(relationship A)}$$

In general we can thus make the bandwidth quite large if we take the spectral distribution function $F(K)$ and correct for the null condition.

In particular we have our highest sensitivity requirement in the vicinity of $x \simeq 0$. In this region $F(OF) \simeq 0$, and we have $2\psi = K_o x$, the monochromatic condition, as a solution above, and $F(EF)$ only lowers the S/N.

iii. Summary.

In summary our polarization interferometer can be used as a "white light" interferometer under the following conditions:

(1) In the near zero aberration area with no corrections on the monochromatic case provided we use $K = K_o$.

(2) In the larger aberration area, with no corrections, if the asymmetry of the distribution is small. For example, if

$$\left| \frac{iF(OF)}{F(EF)} \right| \leq \frac{1}{60},$$

we would have $1/200\lambda$ error. We also assume $F(FE) \simeq 1$.

(3) In the larger aberration area if the spectral characteristics are known and we make corrections as provided by relationship

A, or if we are willing to accept lower accuracy for the larger aberration measurements, where the above relationship determines the measurement degradation if we know our distribution and sensitivity functions.

f. Signal-to-Noise Ratio

In order to resolve a small change in signal we want the S/N ratio to be greater than the ratio of signal to change in signal, produced by a phase difference, $I/\Delta I$. For a very high degree of confidence 99%, three sigma, we require that $S/N > 3I/\Delta I$.

For Δ small, $\psi \approx 0$, $\theta = 45^{\circ}$

$$\Delta I \approx I\Delta$$

$$\therefore \frac{I}{\Delta I} = \frac{1}{\Delta} \quad \text{and} \quad \frac{S}{N} > \frac{3}{\Delta}.$$

The signal-to-noise results from taking *two* measurements on an approximate equal number of photons.

$$\frac{S}{N} = \frac{\sqrt{\#\text{Photons}}}{\sqrt{2}} \times \text{DQE}$$

$\#\text{Photons} = N a t B \cdot E$

N = number incident per unit time per A° per sec. ≈ 1000

a = collecting area ≈ 100 cm^2

B = bandwidth ≈ 500 A°

E = polarizer effect = .5 (linear polarizer efficiency) $\times$ .5 (Wollaston prism) = .25.

DQE = Detective Quantum Efficiency of Detector $\approx .33$

Thus

$$\#\text{Photons Required} \;=\; \frac{1}{E}\left(\frac{3\sqrt{2}}{\Delta}\right)^2 \frac{1}{DQE^2} \qquad 99\% \text{ confidence}$$

$$=\; \frac{720}{\Delta^2}$$

This relationship is graphed in Fig. 54.
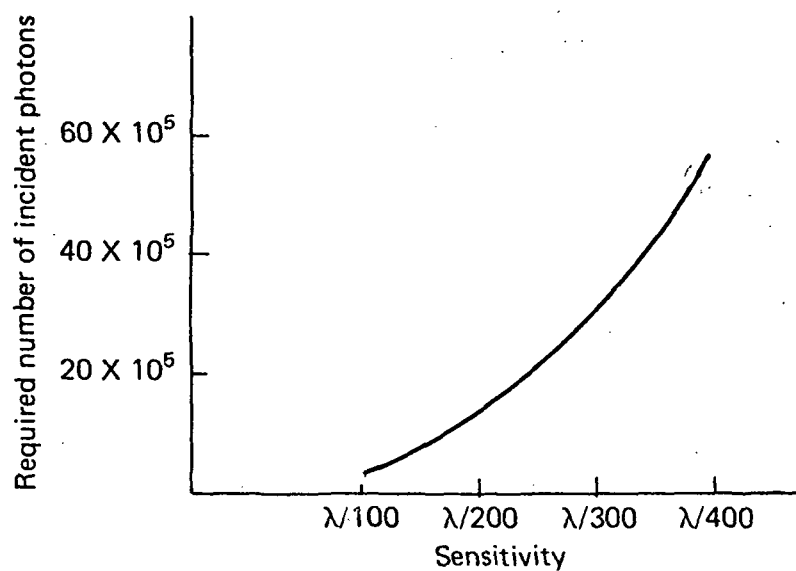
Fig. 54. Relationship between the required number
of incident photons versus sensitivity.

Using:

$$a = 100 \text{ cm}^2$$

$$B = 500 \text{ A}^\circ$$

$$N = 1060 \text{ photons/cm}^2\text{sec A}^\circ \text{ for } A_0 \text{ zero magnitude star.}$$

We obtain a graph of sampling time versus star magnitude for various sensitivity requirements in Fig. 55.
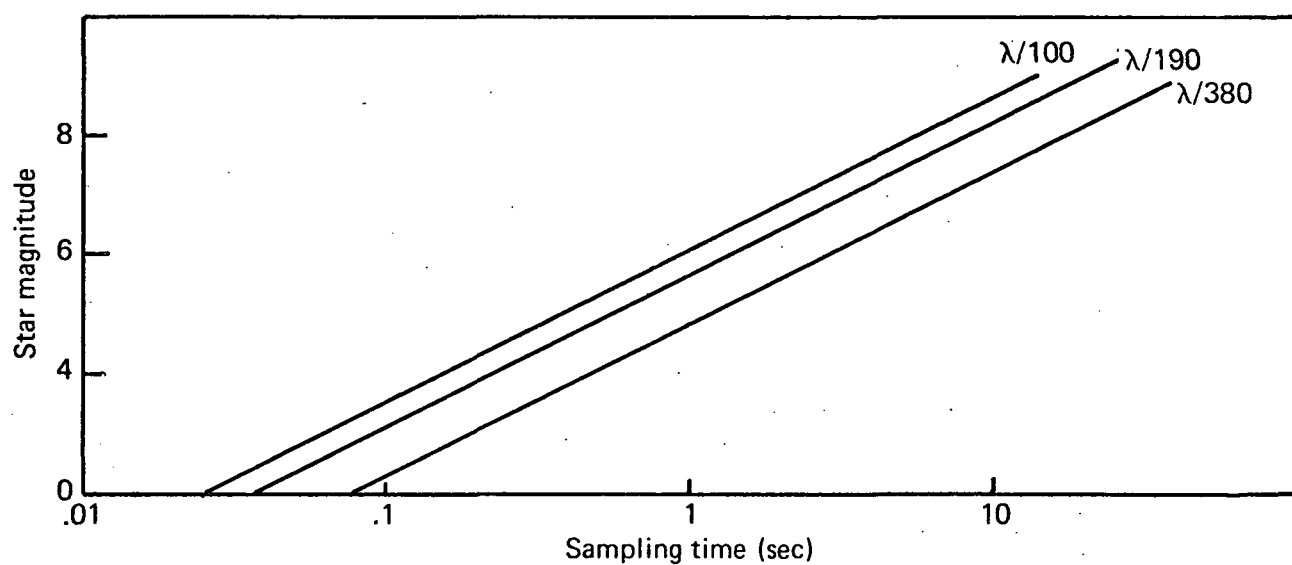
Fig. 55. Sampling times and stellar magnitudes required for three sensitivities.

g. The Effect of Shearing on the Low Order Aberrations.

In the shearing interferometer we measure the difference in optical path between two points in the pupil. Below we derive expressions in terms of the shear S and the aberration coefficients. From these expressions we will be able to predict the minimum amounts of low order aberrations we are sensitive to as a function of shear S, and instrument sensitivity.

$$x^2 + y^2 \leq 1^2 + \frac{S^2}{4} - 2 \cdot \frac{S}{4}\cos\gamma$$

$$\sin\gamma = \frac{y}{1}$$
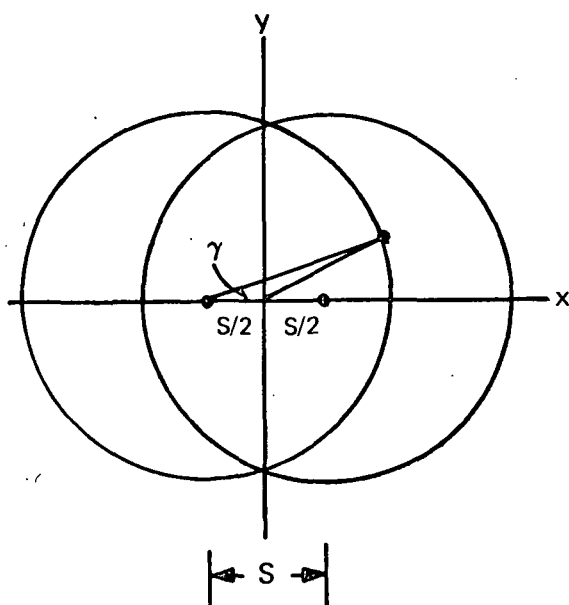
$$y_{max} = + \sqrt{1 - (\tfrac{S}{2})^2} \qquad |x_{max}| = \left|1 - \frac{S}{2}\right|$$

In the nonsheared pupil, if coma is oriented at angle θ, astigmatism at angle ψ and tilt at angle α, all measured from the y axis, the general wavefront expression is:

$$W(x,y) = W_{20}(x^2+y^2) + W_{040}(x^4 + 2x^2y^2 + y^4)$$

$$+ W_{11}x \sin\alpha + W_{11}y \cos\alpha + W_{31}(x^2+y^2)(x \sin\theta + y \cos\theta)$$

$$+ W_{22}[\tfrac{1}{2}(x^2+y^2) + \tfrac{1}{2}(y^2-x^2)\cos2\psi + xy \sin2\psi].$$

This is a normalized expression where $x^2+y^2 \leq 1$. We now shear the pupils by an amount S, where S is a number from 0 to 2 (where S = 2 is a shear of a pupil diameter). This is illustrated above. At some point A, we now have two waves, W(+) and W(−) interfering.

$$W(\pm) = W(x \pm \frac{S}{2}, y)$$

By substituting in the previous expression for W we obtain:

$$W(\pm) = W_{20}\{(x^2+y^2) \pm Sx + \frac{1}{4}S^2\}$$

$$+ W_{40}\{(x^2 + 2x^2y^2 + y^4) \pm 2x(x^2+y^2)S + \frac{1}{2}(3x^2+y^2)S^2$$

$$\pm \frac{1}{2}xS^3 + \frac{1}{16}S^4\}$$

$$+ W_{11}\{x \sin\theta \pm \frac{1}{2}S \sin\alpha + y \cos\alpha\}$$

$$+ W_{31}\{(x^2+y^2)(x\sin\theta + y\cos\theta) \pm \frac{1}{2}[(3x^2+y^2)(\sin\theta)$$

$$+ 2xy\cos\theta]S$$

$$+ \frac{1}{4}[3x\sin\theta + y\cos\theta]S^2 \pm \frac{1}{8}S^3\sin\theta\}$$

$$+ W_{22}\{[\frac{1}{2}(x^2+y^2) + \frac{1}{2}(y^2-x^2)(\cos2\psi) + (xy\sin2\psi)]$$

$$\pm \frac{1}{2}[(1-\cos2\psi)x + (\sin2\psi)y]S$$

$$+ \frac{1}{8}[(1-\cos2\psi)]S^2\}.$$

At point A, we measure the difference between W(+) and W(-).

$$W(+) - W(-) = 2W_{020}xS + 4W_{040}x(x^2+y^2)S + W_{040}xS^3$$

$$W_{11}S\sin\alpha + W_{31}[(3x^2+y^2)\sin\theta + 2xy\cos\theta]S$$

$$+ \frac{1}{4}W_{31}\sin\theta S^3 + W_{22}[(1-\cos2\psi)x + \sin2\psi y]S.$$

i. Sensitivity Dilution.

We can make use of the expression above to determine our ability to measure various amounts of the different aberration types as a function of 1) our ability to measure W(+) - W(-) and 2) the amount of shear S. This information is summarized in Table 7 and Table 8. We see that in general the result of shearing is to reduce the sensitivity in measuring small amounts of aberration. This dilution, of course, is dependent upon the functional form of the aberration, and the amount of shear. For the LST a shear of .2 → .4 (the value of S) would be appropriate since it would give information over most all of the pupil. The important thing to recognize here is that the very fact of shearing dilutes the

sensitivity of any readout one chooses and that in order to make up for this dilution one must look for more sensitive forms of readout, as in the case of the polarization type readout, which we are investigating.

ii. Small Shear Limit.

As we make S small we can take the division

$$\frac{W(+) - W(-)}{S} = W_{11}\sin\alpha + 2W_{20}x + 4W_{40}x(x^2+y^2)$$

$$+ W_{31}[(3x^2+y^2)\sin\theta + 2xy\cos\theta]$$

$$+ W_{22}[(1-\cos2\psi)x + \sin2\psi y].$$

This is merely the expression for $\delta W/\delta x$, the slope of the wavefront (x component) at x,y. A corresponding shear in the y direction would then give the y component slope $\delta W/\delta y$.

SHEAR	.2	1	1.6
ABERRATION			
DEFOCUS	1/10λ	1/25λ	1/16λ
TILT	1/5λ	1/25λ	1/40λ
SPHERICAL	1/20λ	1/50λ	1/6λ
COMA	1/20λ	1/50λ	1/6λ
ASTIGMATISM	1/5λ	1/12λ	1/8λ

TABLE VII

Lateral shear, 1/50λ detection capability, static, fringe position reading.

SHEAR	.2	1	1.6
ERROR			
DEFOCUS	1/60λ	1/150λ	1/90λ
TILT	1/30λ	1/150λ	1/300λ
SPHERICAL	1/120λ	1/300λ	1/35λ
COMA	1/120λ	1/300λ	1/35λ
ASTIGMATISM	1/30λ	1/75λ	1/50λ

TABLE VIII

Shearing polarization interferometer, assuming 1/300λ capability with lateral shear (polarization or other phase reading scheme).

3. Zernike Polarization Sensor (ZPS)

a. General Discussion

The ZPS represents a conceptual attempt to marry the Zernike test to a polarization readout. The result can be a sensor with at least the sensitivity of the Zernike test and a readout which provides for a direct phase measurement, in terms of linear polarization state.

The experimental arrangement is indicated in Fig. 56. The wavefront from the system exit pupil first passes through a linear polarizer. At the system focus we place a birefringent crystal polished with its optic axis in the plane of the surface and adjusted to a multiple order thickness of a quarter wave. A small circular square well (~1/3 the Airy disc diameter) is eroded to a depth corresponding to a half-wave retardation between the ordinary and extraordinary waves. The area surrounding the square well is partially aluminized so that, with the Airy pattern centered across the well, the energy transmitted through the well is equal to the energy transmitted through the surround. As a result of this arrangment, we generate a reference wave of one circular polarization sense from the inner part of the central core of the diffraction pattern, and a test wave of the opposite circular polarization sense from the outer part of the diffraction pattern. The lens following re-images the system pupil at plane C. In this plane, the two oppositely circular polarized waves interfere. According to the equations developed for the Zernike test, which are again applicable here, the test wave contains the wavefront deformation from each point on the pupil, and the reference wave is of essentially constant phase across the pupil, the constant dependent on the amount and type of aberration, and the
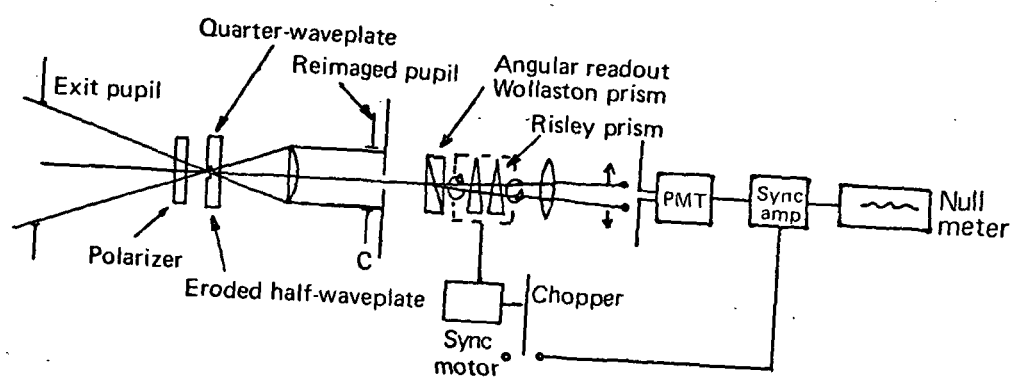
Fig. 56. Zernike polarization sensor laboratory simulation.

size of the eroded well. These two waves combine to produce a linearly polarized state (the polarization direction depending on the phase difference at the point), at each point in the pupil. We measure this polarization using a device of the type discussed in Chapter IV and illustrated again in Fig. 56. We thus have a test with the simplicity of the Zernike test where we read out phase directly.

b. Design Parameters for ZPS

The optimum design parameters for the ZPS are obtained from the same equations derived for use with the Zernike disc. The effects of the diameter of the half-wave plate will be manifested in the phase variations in the generated reference wave. For relatively small constant effects, we want to keep this diameter about 1/3 the Airy core diameter. The transmission attenuation is introduced only because of its effect on the visibility function, since we are not concerned with the operating point using the ZPS. The optimum T^2 is obtained from Table V.

c. Manufacture

The success of the ZPS depends upon being able to manufacture a small half-wave plate. In order to eliminate tunneling effects we decided to look at materials with a high birefringent index. Two we have chosen to work with are calcite and rutile.

We have prepared several samples of both materials cut with their optical axis lying in the planes of the polished surfaces. We are now trying to discover a procedure which will yield a smooth controllable surface erosion for these materials. We have tried many different acids on

calcite and have discovered one combination which is giving promising results. We have tried many combinations of acids under different conditions for rutile, but have not had positive results.

We are now in the process of obtaining etch rate data on the calcite. After we have determined this we will continue on with the procedure in much the same way as in Zernike disc manufacture if we can find a substitute for the Shipley photo-resist (Shipley does not hold up under the acid combination used for calcite erosion).

Chapter V

SUMMARY

1. Wavefront Error Simulator

We have designed a F/12 wavefront error simulator that will enable us to test several types of figure sensors under varying conditions of stellar magnitude, wavelength range, and aberration type and magnitude. The most critical part of this work was the design of an aberration generator. The design had to meet the specifications for an instrument that could simulate the aberrational effects of misalignment as well as of various asymmetries and orientations of small figure errors. We thus designed an instrument that could simulate errors up to several waves and at the same time have an incremental capability of around $1/100\lambda$. This instrument has been optically and mechanically designed, manufactured, assembled, and aligned.

2. The Hartmann Test

We have considered several methods of reading out the position of the ray being sampled and have decided that the best approach to position determination is the circular scan of a given ray around a small collecting aperture. We have worked on a program that takes the diffraction image size, sampling aperture size and the impulse response of the detector, if applicable (i.e., star tracker), so that the readout parameters may be optimized. A S/N study has been pursued so that sensitivity vs. stellar magnitude can be predicted. Sensitivity predictions, optimum readout predictions and

136

other data reduction corrections and methods have to be verified in the laboratory. We are now proceeding with the experimental evaluation of the Hartmann test.

3. The Shearing Polarization Interferometer

We have examined the general capability of the lateral shearing interferometer and have reached the conclusion that a conventional lateral shearing device will not have adequate sensitivity because of the dilution of sensitivity inherent in a lateral shear. However, by incorporating a polarization type readout into the interferometer we can increase the sensitivity of the instrument significantly. Thus, in the laboratory, the primary objective in the construction of a lateral shearing interferometer is the experimental analysis of the polarization type readout using a star source. We have thus designed and manufactured a white light lateral shearing polarization interferometer in order to evaluate the polarization readout scheme. We have done some S/N studies and subsequent predictions on sensitivities and required stellar magnitudes. A preliminary error analysis on the system alignment and component fabrication has also yielded results. We plan to align the interferometer and evaluate it using the wavefront error simulator.

4. Zernike Test

We have worked on the general theory of the Zernike test and have developed expressions that can be used in the design of an optimum Zernike disc. We have also developed the theory that shows the effect of the finite size of the Zernike disc on the reimaged pupil due to the mixing of aberra-

tion information in the reference wave. This theory has been programmed and error analysis, S/N analysis, and some simulated experiments have been run. We have also worked on the technique for manufacturing the Zernike disc using an erosion process. Further work has to be done in the data reduction procedure for the Zernike test both for the $\pm$ 1/4λ range and for larger aberrations. Work will be done on handling the effects of nonperfect square well phase shift and other disc irregularities. Work will also continue on the fabrication process.

5. Zernike Polarization Test

This test marries the Zernike test to a polarization readout, the possibilities being an extension of the sensitivity and range of the Zernike test. Much of the theory derived for the Zernike test is applicable here. The task that lies ahead now is an experimental effort on the manufacture of the device. One method we are investigating now involves erosion in calcite. If the manufacturing technique can be developed it should be followed by an extensive experimental evaluation of aberrations.